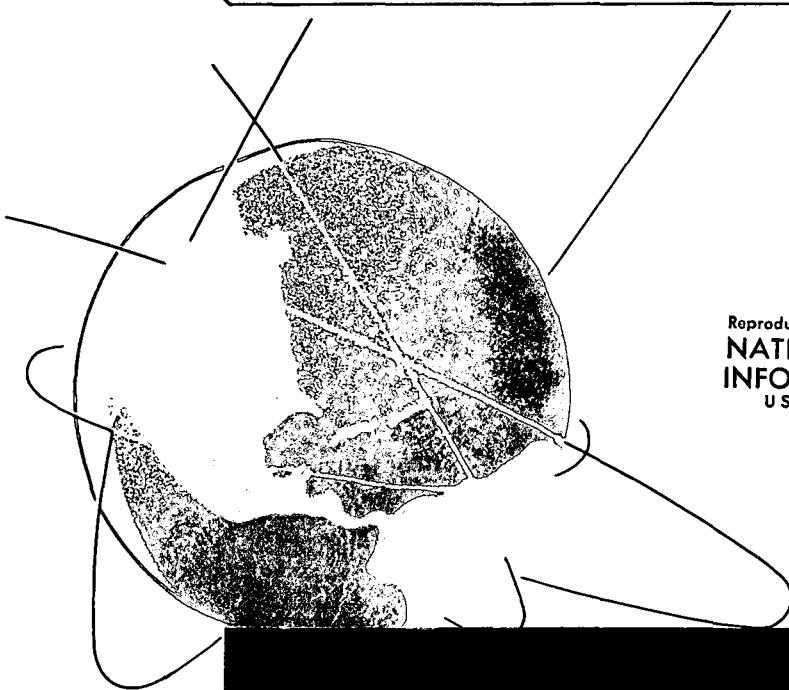
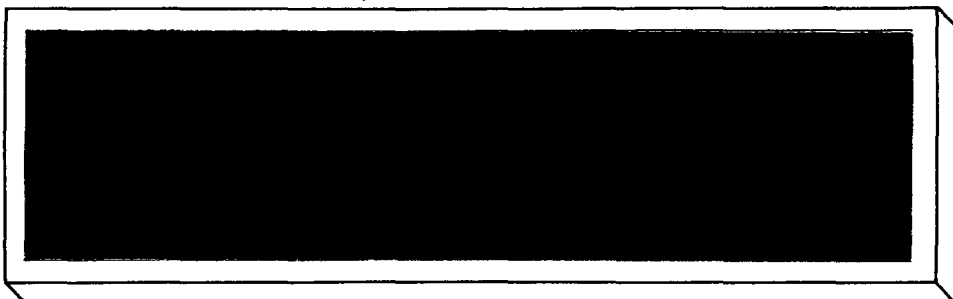
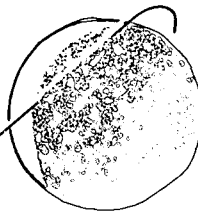


2-17-72



Reproduced by  
NATIONAL TECHNICAL  
INFORMATION SERVICE  
U S Department of Commerce  
Springfield VA 22151



(NASA-CR-128586) HYPERSONIC  
SHOCK-INTERACTION PHENOMENA APPLICABLE TO  
SPACE SHUTTLE CONFIGURATIONS J.J. Bertin,  
et al (Texas Univ.) Aug. 1972 97 p CSCL

N73-10318

20D G3/12

Unclas  
45740

118P.

CR-128586

HYPERSONIC SHOCK-INTERACTION PHENOMENA APPLICABLE  
TO SPACE SHUTTLE CONFIGURATIONS\*

by John J. Bertin and Bruce W. Graumann

Aerospace Engineering Report 72003

\*The authors gratefully acknowledge the financial  
support provided by the Manned Spacecraft  
Center through NASA  
Contract NAS 9-11082

Details of illustrations in  
this document may be better  
studied on microfiche

Department of Aerospace Engineering and  
Engineering Mechanics

The University of Texas at Austin

August 1972

i



# TABLE OF CONTENTS

INTRODUCTION . . . . .	1
Models Consisting of Basic Elemental Combinations . . . . .	1
Models of Specific Flight Vehicles . . . . .	5
Straight-wing orbiters . . . . .	6
Delta-wing orbiters . . . . .	9
NOMENCLATURE . . . . .	12
EXPERIMENTAL PROGRAM . . . . .	14
Models . . . . .	14
VAC HVWT program . . . . .	14
AEDC Tunnel B program . . . . .	15
Test Facilities . . . . .	16
Test Program . . . . .	17
DISCUSSION OF RESULTS . . . . .	19
Fuselage Flow Field . . . . .	19
VAC models . . . . .	19
AEDC NAR 161B DWO . . . . .	22
Wing Flow Field . . . . .	25
Alpha of 0° . . . . .	25
Alpha of 30° . . . . .	29
(a) Delta-wing configurations . . . . .	32
(b) Straight-wing configurations . . . . .	36
Alpha of 50° . . . . .	39
(a) Delta-wing configurations . . . . .	40
(b) Straight-wing configurations . . . . .	45
Additional Measurements for the Delta-Wing Configurations . .	49

SUMMARY . . . . .	51
CONCLUSIONS . . . . .	54
REFERENCES . . . . .	55
TABLES . . . . .	59
FIGURES . . . . .	67

## INTRODUCTION

To determine the convective heat-transfer distribution for space-shuttle configurations, one must consider the viscous:inviscid interactions associated with the complex three-dimensional flow fields. Locally severe heat-transfer rates may occur when an externally generated shock wave impinges directly on the boundary layer, when the shear layer generated by the intersection of two shock waves impinges on the surface, and when boundary-layer separation in a compression corner induces a shock wave with the attendant shock-wave: boundary-layer interaction. Because the most severe convective-heating problems of atmospheric flight at high speeds are due to viscous:inviscid interactions, these phenomena have been the subject of numerous investigations. Two excellent surveys of the related literature have been published recently (refs. 1 and 2). Because the current research effort involved a hypersonic shock-interaction and impingement phenomena applicable to space-shuttle configurations, it is germane to review some of these results, if only briefly. For the present discussion, the literature review of the "Introduction" will be divided into two sections: (1) models consisting of basic elemental combinations and (2) models of specific flight vehicles.

### Models Consisting of Basic Elemental Combinations

Because of the complexity of the viscous:inviscid interaction phenomena, many investigators have studied the locally perturbed flow fields using models simulating a limited portion of a complete flight vehicle. By considering only a limited portion of the vehicle, a relatively large scale model can be built with a corresponding increase in the instrumentation density. Further, the investigators can concentrate on the governing physical mechanisms using models

combining simple elemental configurations. One can, therefore, study those parameters which govern the mechanisms for shock-interference patterns.

It has been observed that hypersonic vehicles can experience severe damage due to locally high heating rates generated when the bow shock-wave of the vehicle impinges on the leading edge of a wing or a fin. The problems of shock-wave:boundary-layer interference have been widely studied in recent years. Many of the investigations employed a shock generator (either a wedge or a conical surface) to generate the incident, or "bow", shock wave and a fin with a hemicylindrical leading edge to represent the wing. Thus, the models were designed to simulate the essential features of the flight configurations, yet provide a flow field which could be readily analyzed.

As the angle between the shock-generating surface and the cylinder decreases, a distinct change occurs in the structure of the intersecting shock waves. Gulbran et al (ref. 3) identify two distinct structures, depending upon whether the angle is large or sufficiently small. Gulbran notes further, however, "because flow separation on the shock generator may occur in either model, there are actually four flow fields to consider". Edney (ref. 4) states flatly that three interference patterns are possible for these flows. For fins at zero or small angles of sweep, a Type IV interaction occurs; for angles of sweep around  $30^\circ$ , Type V; and for large sweep angles, Type VI. Sketches of these interference patterns are presented in Fig. 1.

An experimental investigation of the shock-wave impingement problem has been conducted by Hiers and Loubisky (ref. 5) in the Ames 1-foot shock tunnel at Mach 14 at a low Reynolds number. Boundary-layer separation was observed upstream of the unswept cylinders at these low Reynolds numbers, producing a second heating peak due to the impingement of the separation shock wave. For these flow conditions, order-of-magnitude increases in the stagnation-line heat-transfer to the unswept leading edge were observed in localized regions

as a result of the shock-wave impingement. The deflection angle of the shock generator for these test was  $15^\circ$ , or less. In another hypersonic, low-Reynolds-number investigation, Knox (ref. 6) noted that whenever the leading edge was unswept, the flow on the shock-generator surface was separated for shock-generator flow-deflection angles of  $20^\circ$ , or less. The stagnation-line heat-transfer was found to increase locally by a factor of six for the tests in which boundary-layer separation occurred. Data were also obtained for a shock-generator flow-deflection angle of  $40^\circ$ . The boundary layer did not separate for this case and the perturbation in the heating to the unswept leading edge was only a factor of two. The laminar interaction with boundary-layer separation ahead of the cylinder at low sweep-angles leads to significantly higher heat-transfer rates. Gulbran et al (ref. 3) attribute the locally high heating to the additional compression of the flow caused by separation.

Hains and Keyes (ref. 7) identified locally high heating rates on a fin with  $20^\circ$  sweepback as the result of the shock:boundary-layer interaction associated with a Type V interference pattern. The Type V pattern has a detached supersonic jet and shear layer. Hiers and Loubsky (ref. 5) observed a similar heating increase on the stagnation line of a cylinder which was swept back  $22.5^\circ$ . Because of the type of data obtained (and the then limited understanding of the flow mechanisms involved), Hiers and Loubsky could not describe with certainty the resultant flow field. "The absence of a heat-transfer peak associated with the intersection of the generated shock wave and the bow shock wave with the leading edge swept  $22.5^\circ$ " was noted. Instead, "the disturbance induced effects appear to be associated with the separation phenomena on the shock-generator plate". Using flow visualization photographs

from the Martin-Marietta Hotshot Wind Tunnel and from the Vought Aeronautics Corporation Hypervelocity Wind Tunnel, it was concluded (ref. 8) that a Type V pattern was produced by the interaction of the fuselage-generated shock wave with the shock wave generated by the  $15^\circ$  swept wing of the space-shuttle orbiter model at  $40^\circ$  angle-of-attack.

Bushnell (ref. 9) correctly identified the flow-field phenomena associated with the intersection of the "bow-generated" shock wave with the cylinder-generated shock wave for very large sweep angles. Edney classifies this interaction as a Type VI pattern. No localized increases in heating were observed for either laminar or turbulent stagnation-line boundary-layer flow. Instead, the heating increased "uniformly" along that portion of the cylinder subjected to the wedge flow. The maximum increase in this region can be predicted using the local flow conditions to evaluate the necessary fluid properties for the infinite, swept-cylinder theories of ref. 10. By comparing the data obtained for the cylinder and wedge attached with the data obtained for the cylinder and wedge separated, Bushnell found that the extent of flow separation in the cylinder-wedge juncture was small for the flow conditions considered. Hiers and Loubsky (ref. 5) observed the same general features in data obtained at a very much lower Reynolds number. Thus, there was no region of locally intense heating on the stagnation line of a cylinder for a large sweep angle and there was no separation of the boundary layer from the shock generator.

Thus, from these tests involving "partial" models, one finds that the important parameters in describing the interaction between the bow shock-wave and the wing shock-wave include initial flow deflection (i.e., incidence angle of the shock-generator), the sweep angle of the leading edge, the Mach number, and the Reynolds number. Most of the previous investigators have

considered the Reynolds number as it relates to separation of the boundary-layer upstream of the wedge:cylinder juncture. Bushnell (ref. 9) also noted that, at high angles of sweep, the wedge flow caused transition for the wedge:cylinder configurations at a smaller value of the free-stream Reynolds number than for the undisturbed cylinder. However, it was noted further that, if the local wedge Reynolds number is used as a criteria for the wedge:cylinder tests, a single value can be used as a transition criteria.

### Models of Specific Flight Vehicles

It has been often observed that the viscous:inviscid interactions produce locally severe heating rates even for "clean" configurations, i.e., those configurations which represent only the basic vehicle geometry without the various surface irregularities which would be present on the actual flight vehicle, such as windows or antenna pods. When the complexity of the configuration generates a flow field in which multiple shock waves are present, interactions between two, or more, shock waves may create regions of locally severe heating. Using models spray painted with Detecto-Temp paint, Lorenz et al (ref. 11) noted that, in the vicinity of the wings, the wing-generated shock wave crossed the body, causing a thickening of the boundary layer upstream of the shock (with reduced heating) and then an increase in heating due to the increase in pressure behind the shock. Studies of the flow field, surface-pressure distributions, and heat-transfer distributions for several tension shell configurations indicated that the extent of separation on the concave surface and the multiple-shock flow pattern were a function of the wall-to-total temperature ratio, the Reynolds number, the nose bluntness, and

the base corner radius (ref. 12). A comparison of the shock patterns for the high-drag configuration indicated that the location of the nearly normal flare shock is strongly dependent on the normal shock density ratio (which was varied using different test gases).

The intensity of the interaction phenomena between the fuselage-generated shock wave and the wing-generated shock wave is strongly configuration dependent. The flow-field perturbations are much more pronounced for the straight-winged, or low cross-range, orbiters than for the delta-winged, or high cross-range, orbiters. Further, although one would expect that the wing planform surface would alter the shock-interaction pattern as the angle-of-attack increases, the investigations using cylinders mounted on wedge shock-generators suggest a fundamental division between straight wings of low sweep and delta wings having large sweep angles.

Straight-wing orbiters. The interaction between the wing-generated shock wave and the fuselage-generated shock wave produces localized increases in the heating both on the fuselage and on the wing. Marvin, et al, (ref. 13) noted localized increases in surface-pressure and in the heat-transfer rates measured in the pitch plane of fuselage between the wings at an angle-of-attack of  $60^\circ$ . The pressure increases were essentially independent of the Reynolds number. The perturbations in the pitch-plane heating measurements, however, increased with Reynolds number. Since the heat-transfer data downstream of the wing are in satisfactory agreement with laminar theory, the Reynolds number influence is attributed to the "complex nature of the flow in this region" rather than to transition. At an angle-of-attack of  $30^\circ$  only slight increases occurred in the surface-pressures and in the heat-transfer rates measured in the pitch plane of the fuselage between the wings. On the wings, however, the more significant increases in the heating were noted at an angle-of-attack of



30°. At both angles-of-attack, the wing heating-rate increased with increasing Reynolds number.

Making extensive use of shadowgraphs and excellent quality oil flow patterns on the model surface, Seegmiller (ref. 14) concluded that, for a straight-winged orbiter at 40° angle-of-attack, the windward shock interference region is composed of two similar impinging shock waves, which are oblique to the wing flow streamlines, and a shear region impingement. The proposed flow model was described in a plane perpendicular to the wing surface. Heat-transfer data were presented which supported the flow-field model derived from the oil flow patterns. At 60° angle-of-attack, the interaction between the fuselage shock and the wing shock no longer had an observable influence on the oil flow pattern, although a distortion of the wing stagnation line was noted near the 40% span position. Although the magnitude of the shock-interference heating perturbation decreased rapidly with angle-of attack, shock interference heating effects were still observed at  $\alpha = 70^\circ$ . The significant perturbations in the heat-transfer rate to the wing were observed between 20% to 55% of the exposed span and forward of the 30% chord location. The spanwise heat-transfer distributions measured on a straight-winged orbiter model in the CAL HST (ref. 15) also indicated local increases in the heat transfer to the wing at an angle-of-attack of 70°. Double-peaked spanwise heating distributions which were observed for many of the test conditions were attributed to the bifurcated shock resulting from the interaction of the bow shock and the wing shock.

Kessler et al (ref. 16) investigated a cross-flow model as a degenerate case of the complex three-dimensional shock structure. The shock-wave interaction flow-structure based on these cross-flow calculations differed from that proposed by Seegmiller (ref. 14). Using post-run burn patterns on the

model wing and schlieren photographs taken in the Martin-Marietta Hotshot Wind Tunnel, Kessler et al concluded that Edney's Type V shock-interaction pattern best fit the data (as well as matching Seegmiller's oil flow data). Photographs of the shock-wave structure taken in the VAC Hypervelocity Wind Tunnel (ref. 17) support the conclusion that the Type V pattern describes the shock-wave interaction for a straight-winged orbiter at angles-of-attack of  $40^\circ$  and  $50^\circ$ . As noted previously, the essence of these latter two investigations have been reported in ref. 8.

The data discussed above were obtained in facilities where real gas effects would not be expected to significantly affect the shock-interaction phenomena for the straight-winged orbiter. By comparing data from facilities using helium, air, nitrogen, and tetrafluoromethane as the test gases, Hunt and Creel (ref. 18) studied the effect of shock-density ratio on the body-shock:wing-shock interaction phenomena. The intersection moved inboard along the wing span with increasing angle-of-attack until, at some critical angle-of-attack range, the flow field changed and the shock impingement effects did not appear to significantly affect the wing heating patterns. The critical angle-of-attack range was associated with a large change in the inviscid flow in which stand-off-distance greatly increased and the local stagnation region moved from the wing leading edge toward the central portion of the wing. The angle-of-attack at which this phenomena occurred was found to be relatively independent of the free-stream Mach number, but showed a strong dependence on shock density, or specific-heat ratio.

The relation between the location of the flow impingement on the wing leading edge and the angle of attack was discussed in ref. 17. The functional relation was determined using flow-field photographs, post-test photographs of

the model surface, and heat-transfer distributions from a variety of facilities where the test stream was air or nitrogen ( $\gamma \approx 1.4$ ). The impingement location moved inboard as the angle-of-attack increased to  $50^\circ$ . At higher angles-of-attack, the fuselage-generated shock wave and the wing-generated shock wave merge as the flow encounters the very blunt cruciform shape.

Delta-wing orbiters. Hunt and Creel (ref. 18) concluded that, because the delta-wing configuration "reenters at lower angles of attack and is essentially free of imbedded shocks, real-gas shock-density-ratio effects will be less significant" than those for the straight-winged orbiter.

The shock-interaction and impingement phenomena and the resultant interference heating is a function of configuration geometry. Since the delta-wing configurations are "second-generation" orbiters, the data available in the literature were obtained for a variety of geometries. These geometric differences may explain, at least in part, the differences between the interference phenomena reported in the literature.

Shock-impingement patterns were not evident (ref. 19) in the oil flow patterns obtained in the LRC Variable Density Tunnel using the Grumman Aerospace Corporation's H-33 delta-wing orbiter at an angle-of-attack of  $27^\circ$ . However, the leeward oil flow patterns indicated impingement at approximately 70% span, as measured from the center-line. The phase-change heating patterns obtained on the windward wing surface at the higher Reynolds number indicate heating increased at 70% span due to the impingement of the bow shock on the wing. At the lower Reynolds number, little effect was observed due to the interaction between the wing and fuselage flows. An increase in the heating-rate measured along the pitch-plane of the fuselage was observed downstream of  $x = 0.35L$ . This increase in heating which was invariant with Reynolds number was centered about  $x = 0.55L$ .

Impingement of the booster bow-shock-wave on the delta wing was evident (ref. 20) for angles-of-attack from  $0^\circ$  to  $50^\circ$ . At an alpha of  $20^\circ$ , the peak in windward heating occurred at the point of impingement, which was about the 45% span location, as measured from the center-line. At this relatively low angle-of-attack, the effects of the bow:wing shock-interaction are pronounced only near the leading edge. At intermediate alphas, i.e.,  $40^\circ$  and  $50^\circ$ , the effect of bow-shock impingement influenced a much larger portion of the wing. At the higher Reynolds number conditions of the test, i.e., a unit Reynolds number of  $6 \times 10^6$  per foot, generally higher heating rates occurred outboard of the shock intersection. It was concluded that the boundary layer tended toward a laminar condition within the bow-shock field and a turbulent condition outboard of the shock. The same pattern was not observed at the lower Reynolds number, i.e., one million per foot. At the high booster angles-of-attack, i.e.,  $60^\circ$  and greater, bow shock impingement was not observed on the wing. Schlieren photos indicated an almost normal shock enveloped the entire lower surface of the booster.

The present report discusses the surface-pressure and heat-transfer-rate data for a variety of space-shuttle orbiter configurations over an angle-of-attack range from  $0^\circ$  to  $60^\circ$ . The results from the first year of study in this program have been presented in ref. 17. Measurements for the second year's contracted effort were made in VAC's Hypervelocity Wind Tunnel (HVWT). The experimental program included a free-stream Mach number of 10 with free-stream Reynolds number from  $2 \times 10^6$  to  $13 \times 10^6$ . In addition, the present report also analyzes the heat-transfer-rates measured on the NAR DWO 161B in Tunnel B of AEDC, as tabulated in ref. 21. These data are compared with theoretical correlations, with the previously reported data (ref. 17), and with data from other facilities. Flow models have been constructed to describe the flow field

phenomena associated with the interaction between the fuselage-generated shock wave and the wing-generated shock wave. The shock:shock interactions in the vicinity of the wing leading-edge are categorized in terms of the shock-interference patterns described by Edney (ref. 4).

## NOMENCLATURE

$b$	- exposed span of one wing, see Fig. 4b
$c_l$	- local chord length, which is a function of the spanwise location
$c_r$	- root chord length
$F$	- a factor which accounts for the non-circular shape of the fuselage cross-section when calculating the stagnation point velocity gradient defined in eqn. (2)
$L$	- total model length, measured along the fuselage axis
$M$	- Mach number
$p$	- pressure
$\dot{q}$	- local heat-transfer rate
$\dot{q}_{t,loc}$	- calculated value of heat-transfer to the stagnation point of a sphere whose diameter is equal to the local body width
$\dot{q}_{t,R=1 \text{ ft}}$	- calculated value of heat-transfer to the stagnation point of a one-foot sphere scaled to model size
$\dot{q}_{t,ref}$	- calculated value of heat-transfer to the stagnation point of a sphere whose diameter is $W_b$
$R_{eff}$	- effective radius of curvature for a fuselage whose cross-section is non-circular
$R_{ref}$	- one-half the fuselage width, $0.5 W_b$
$R_{scale}$	- radius of a one-foot sphere scaled model size (approximately 0.0045 ft for the VAC models)

$Re_{\infty}/ft$	- free-stream unit Reynolds number
$Re_{\infty,L}$	- free-stream Reynolds number based on model length
$r_{le}$	- leading-edge radius of local wing section
$s$ or $x$	- distance from apex measured along the fuselage axis, see Fig. 4b
$s_w$	- distance from leading edge of wing measured along the chord, see Fig. 4b
$T_t$	- stagnation temperature
$W_b$	- characteristic fuselage width, or body-width
$z_a$	- lateral distance measured from the plane of symmetry, see Fig. 4b
$z_r$	- lateral distance measured from the root chord of the wing, see Fig. 4b
$z_s$	- lateral distance from the plane of symmetry to wing tip, see Fig. 4b
$\alpha$	- angle of attack
$\Lambda$	- leading-edge sweep angle
$\Lambda_{eff}$	- effective leading-edge sweep angle taking into account the angle of attack, defined in eqn. (4)

#### Subscripts

$t_2$	- Value of flow property at stagnation point downstream of normal shock
$\infty$	- value of flow property in free-stream

## EXPERIMENTAL PROGRAM

The experimental program was conducted to provide fundamental information about boundary-layer transition and about shock-intersection and impingement phenomena associated with space-shuttle-type configurations. The parameters considered in the program included: configuration geometry, angle of attack, Mach number, and Reynolds number. The experimental program of the contracted effort included tests in the Martin-Marietta Hotshot Wind Tunnel (MM HWT) and in the Vought Aeronautics Corporation Hypervelocity Wind Tunnel (VAC HVWT). Part of the program planned for the VAC HVWT was delayed considerably by unexpected delays in completing a tunnel modification. Therefore, the results of the first year's study have been reported previously in ref. 17. The shadowgraphs, heat-transfer rates, and surface pressures obtained in the VAC facilities during the second year of the contractual effort are discussed at length in the present report. Further, since the data for the NAR 161B DWO are germane to the University program, they will also be discussed at length in the present report. Therefore, the pertinent information about that program will be reviewed.

### Models

VAC HVWT program. - The planned variables of configuration geometry were the fuselage cross-section and the wing planform. Two fuselage cross-sections were studied, the F3 and F4, which are illustrated in Fig. 2a. The cross-sections of these fuselages match those of "simulated" infinite cylinders which were studied in a companion program (the data of which are discussed in refs. 22 and 23). The three wing planforms which were utilized in the experimental programs are illustrated in Fig. 2b. No dihedral angle was used for any wing. An NACA 0012-64 airfoil section (ref. 24) was used as the



cross-section for the straight wings. Except for the leading-edge radius, the windward surface of the delta wing, i.e., the W4 wing, was flat. Since the delta wing was used only in conjunction with the flat-faced fuselage, the F3, the windward surface of the F3:W4 delta-wing orbiter was flat over the wing area, avoiding a complex corner flow at the wing root.

The models used in the program conducted in the VAC HVWT were instrumented with thermocouples and with pressure orifices, as indicated in Fig. 3. Because it was felt that heat-transfer measurements would be more sensitive to the character of the local flow-field, the number of thermocouples on a model was roughly twice the number of pressure orifices. The local pressures were measured using Sensotech transducers. The semiconductor strain gages of the transducers had a nominal output of one millivolt per psi. The local heating rates were determined from computer fits of the surface-temperature histories. These temperature histories were obtained using thermocouples of 40 gage chromel/constantan wire which were spot welded to the inner surface of the 0.004 inch nickel skin of the models.

The body width,  $W_b$ , was chosen as the characteristic length by which parameters relating to model dimensions were divided to obtain dimensionless correlation parameters. With the exception of the blunt nose, the width of the body, or fuselage, was constant for the VAC HVWT models and was, therefore, a convenient correlation dimension. The exposed span of one wing,  $b$ , was used as a characteristic dimension to identify the location of sensors on the wing.

AEDC Tunnel B program. - The configuration of interest which was tested in Tunnel B of AEDC was a 0.009 scale version of the North American Rockwell (NAR) 161B Delta Wing Orbiter (DWO). The model was machined from 17-4 PH steel to a

nominal skin thickness of 0.04 inch. The orbiter model was instrumented with 204 iron-constantan thermocouples, the outputs of which were recorded on magnetic tape by a Beckman digital data system at the rate of 20 times per second from the start of the model injection cycle. The data reduction technique used to calculate the local convective heating rate once the surface temperature history is known is described in ref. 21.

A sketch of the model is presented in Figure 4. The characteristic parameters for length are defined, as indicated in Fig. 4. The locations of selected thermocouples (as taken from ref. 25) are illustrated in Fig. 5.

#### Test Facilities

The VAC Hypervelocity Wind Tunnel is a hot-shot tunnel with a variable volume arc-chamber to provide relatively constant test conditions. A contoured nozzle is used to accelerate the nitrogen test gas to Mach 8 in an 8.0 inch diameter test section. For free-stream Mach numbers of 10, or greater, the wind-tunnel nozzles are conical with a total included angle of  $7.5^\circ$  and a test-section 12.5 inches in diameter. The high energy capacity of the tunnel provides either a high unit Reynolds number capability, e.g., nominally a unit Reynolds number of  $70 \times 10^6$  per foot at Mach 8, or relatively long run times, e.g., 0.50 second at Mach 17. The facility is complemented by an onsite IBM digital computer which is employed for data acquisition and reduction.

Tunnel B is a continuous, closed-circuit, variable density wind tunnel with an axisymmetric, contoured nozzle and a 50-inch diameter test section. The tunnel can be operated at a nominal Mach number of 6 or 8 at stagnation pressures from 20 to 300 and 50 to 900 psia, respectively, with stagnation temperatures up to 1350°R. The model may be injected into the tunnel for a test run and then retracted for model cooling or for model changes which can be made without interrupting the tunnel flow.

## Test Program

The run schedule for the nominal test conditions of the contracted effort is presented in Table 1. The numbers which appear in this table are used to identify a particular "shot". From the outset of the contract, the test schedule incorporated a break to allow for a scheduled modification of the VAC HVWT and, thereby, to make use of an increased Reynolds number capability. However, the modification took much longer than scheduled and the data from the first year's study were analyzed separately. Those shots which were discussed in ref. 17 are designated by an asterisk.

The current tests served as the first program to be conducted in the modified tunnel. Thus, no operational experience was available to predict the model/tunnel performance at nominal flow conditions 2 and 3. Unfortunately, two serious problems were encountered during the test,

- (1) Considerable wrinkling of the model skin for the fuselage (which was only 0.004-inch thick nickel) occurred during these runs, because of particle impingement and high surface pressures. Post-test examination of the model indicated extreme peak-to-valley differences of 0.01 inch along the fuselage length. Because of the relatively thin boundary layer on these small models, the skin wrinkling contributed to numerous shock waves, which were evident in the flow-field photographs. Further, the skin wrinkling and the associated flow-field perturbations significantly influence the measured heat-transfer, which is very sensitive to the surface roughness of the scale experienced. It should be noted that the delta-wing surfaces did not suffer any noticeable damage, because they were constructed of 0.005-inch thick 302 stainless steel, which is a much tougher material.

(2) The nondimensionalized surface-pressure and heat-transfer rate data obtained at the higher Reynolds number (i.e., nominal condition 3) differed significantly from the values obtained at the lower Reynolds number. Furthermore, the flow-field photographs of the higher Reynolds number flow exhibit marked distortions as can be seen in the photographs presented in Fig. 6 (which are admittedly extreme, although not unique, examples of the problems encountered).

Not all the measurements were affected. However, the uncertainty introduced by these perturbations significantly limited the ability to discuss the effect of flow parameters.

Table 2 contains the exact test conditions for the VAC HVWT data and for the AEDC Tunnel B data discussed in the present report.

## DISCUSSION OF RESULTS

### Fuselage Flow Field

VAC MODELS - As noted when discussing the test program in the section "Experimental Program", the fuselage skin degraded markedly during the present tests. The progressive wrinkling of the fuselage skin means that only the heat-transfer data from the first shots using a particular fuselage are comparable to the previously reported measurements (ref. 17).

The surface-pressure and the heat-transfer-rate distributions measured in the plane of symmetry are presented in Fig. 7 for the F4:W2 at an angle-of-attack of 50°. To nondimensionalize the data, the local heat-transfer-rate measurements have been divided by  $\dot{q}_{t,\text{ref}}$ , which is the theoretical heating rate (ref. 26) to the stagnation point of a sphere whose diameter is equal to the body width of the fuselage (exposed to the flow conditions of the data). Since the model scale is approximately 0.0045, the reference heating rate commonly used by NASA (i.e.,  $\dot{q}_{t,R=1 \text{ ft}}$ ) may be related to the present reference by:

$$\frac{\dot{q}_{t,\text{ref}}}{\dot{q}_{t,R=1 \text{ ft}}} = \sqrt{\frac{R_{\text{scale}}}{R_{\text{ref}}}} = 0.3286$$

The measurements from the current effort (which are from the third shot using the F4 fuselage) compare reasonably with the previous data.

The experimental surface pressures decrease with distance from the stagnation point, such that the data just upstream of the wing are in reasonable agreement with the value for modified Newtonian flow. Except for that region which is upstream of  $s = 0.5 W_b$ , the fuselage is of constant cross-section. Thus, the modified Newtonian pressure is constant along the fuselage for a

given angle-of-attack (and equal to the value which is indicated in the figure). The wing-generated shock wave perturbs the fuselage flow field, as indicated by the increase in surface pressure. The experimental pressure distribution is essentially independent of the free-stream flow conditions, even in the perturbed region. The interaction of the wing-generated shock wave with the fuselage-generated shock wave perturbed the heat transfer also. The perturbations in the heat-transfer rates appears to depend on the Reynolds number. However, the experimental variations in the heat-transfer data mask the exact form of the dependence.

The surface-pressure and the heat-transfer-rate distributions measured in the pitch plane of straight-winged orbiters having an F3 fuselage are presented in Fig. 8 for an  $\alpha$  of  $50^\circ$ . The repeatability of the data for the two shots made before the tunnel modification (Fig. 8a) is considered very good. The differences in the data for the downstream thermocouples are attributed to run-to-run variations in heat-transfer measurements in a region where the boundary layer is transitional or turbulent rather than to actual flow-field differences caused by variations in the wing geometry. Considering all the data for the F3-fuselage at an angle-of-attack of  $50^\circ$ , one finds considerable scatter in the heat-transfer measurements obtained after the tunnel modification was completed, i.e., the open symbols of Fig. 8b. Because this scatter is attributed to the two problems discussed previously, no further analysis of these data is planned at this time.

As noted in ref. 17, the fuselage flow was essentially independent of the wing geometry for the straight-winged configurations tested. Thus, one can examine geometry effects by comparing the data for the F4-fuselage (presented in Fig. 7) with the data for the F3-fuselage (presented in Fig. 8a).

Based on these measurements alone, there is no discernable difference in the laminar heat-transfer rates in the undisturbed region upstream of the wing for the two fuselages. Using the swept cylinder relation to calculate the heat-transfer rate to the fuselage:

$$\frac{\dot{q}}{\dot{q}_{t, \text{ref}}} = 0.707 F (\sin \alpha)^{1.2}, \quad (1)$$

where the factor  $F$  accounts for the noncircular shape of the cross-sections and is, therefore,

$$F = \sqrt{\frac{0.5W_b}{R_{\text{eff}}}}. \quad (2)$$

Based on an experimental study employing axisymmetric models (ref. 27), the factor accounting for the effective radius of curvature of the F4-fuselage is 0,685. Using the relation of ref. 28 to calculate the effective radius of curvature for the flat-faced cross-section of the F3-fuselage, the factor of  $F$  is 0,639. Thus, for a given flow condition, the heating rates as computed using eqn (1) for the two fuselages would differ by less than eight percent, which is within the expected experimental variation.

The pressure increase due to the influence of the wing shock appears to extend further upstream for the F4-fuselage. The dimensionless pressure measurements for the third orifice are approximately 15% higher for the F4-configurations, while the values for the two fuselages are very close at each of the other orifices. The difference in shock-interaction pattern which causes this pressure difference results since the wings are located at the maximum width point of the F4-configurations and are, therefore, not tangent to the windward pitch plane as are the wings of the F3-configurations. The difference between the wing location can be seen in the sketches of Figs. 7 and 8. Furthermore, the windward surface of the F4-fuselage is curved, while

it is flat (and flush with the wings) for the F3-fuselage.

AEDC NAR 161B DWO - The heat-transfer-rate distributions for the windward pitch plane of the NAR 161B delta-wing orbiter are presented in Fig. 9 for angles-of-attack of  $0^\circ$ ,  $30^\circ$ , and  $50^\circ$ . To nondimensionalize the data, the experimental value of the local heat-transfer rate has been divided by the theoretical value for the stagnation point (ref. 26) of an 0.009-scale one-foot sphere, i.e., a one-foot sphere which has been reduced to the scale of the model. Included for comparison with the data from the test program conducted in Tunnel B of AEDC are data obtained in the Ames 3.5-foot Hypersonic Wind Tunnel (ref. 25). For an alpha of  $0^\circ$ , the heat-transfer rate decreases rapidly with distance from the stagnation point over the first ten percent of the model. The heating rate increases in the vicinity of the wing juncture (the percentage increase and, apparently, the extent of the region which is affected by the perturbations in heating is greater for the higher Reynolds number flow). For an alpha of  $30^\circ$ , the heating data from the Ames facility "increase with increasing Reynolds number, thus indicating a transition to turbulent flow. The results seem to indicate transition sticking at the wing-body juncture". The transition sticking is further complicated because "a joint in the model surface at  $x/L = 0.57$  resulted in a small forward-facing step (about 0.025 mm high)". The data from the Tunnel B tests are insensitive to Reynolds numbers over the range tested. The agreement between the Tunnel B data and the data obtained at the lowest Reynolds number tested in the Ames facility suggests that the highest Reynolds number for which data were obtained in Tunnel B is just below the value required for the onset of transition.

The Tunnel B heat-transfer data for an angle-of-attack of  $50^\circ$  are strongly dependent on the Reynolds number. The increase in pitch-plane heating at the wing:fuselage juncture is attributed to the turbulent character of the



viscous flow. The schlieren photograph of the VAC DWO at an angle-of-attack of  $60^\circ$ , which is presented in Fig. 10, shows an inflection point in the bow shock wave due to the influence of the wing. At this high angle-of-attack, an extensive, rapidly spreading mixing region can be seen dividing the inviscid flows processed by the "two different" shock waves. (The extent and rapid spreading of the mixing region is believed to be enhanced because the windward surface of the fuselage and the wing is flat.) Young et al (ref. 29) observed that the shear layer associated with an inflection point in the bow shock-wave promoted boundary-layer transition. Thus, it is believed that the primary cause of transition sticking at an  $\alpha$  of  $50^\circ$  is a flow-field perturbation associated with an alteration in the bow shock wave due to the presence of the wing. The small step on the model skin, which was noted in ref. 25, is believed to be much more important to the flow for an  $\alpha$  of  $30^\circ$ , for which the shape of the bow shock is not visibly perturbed by the presence of the wing. For the highest Reynolds number tests of ref. 25, transition occurs well upstream of the wing at an  $\alpha$  of  $50^\circ$ .

The heat-transfer-rate distributions for the windward pitch plane are presented in Fig. 11 for an angle-of-attack of  $30^\circ$ . If all the local heat-transfer measurements for a given flow condition are divided by the same reference heating rate, the resulting dimensionless heat-transfer data are independent of Reynolds number and decrease rapidly with distance from the stagnation point, as shown in Fig. 11a. By nondimensionalizing these same measurements in a different form (see Fig. 11b), it appears that the variation is not due to a flat-plate-like growth of the boundary-layer with distance from the stagnation point, but the variation is due to the flow modifications associated with the increasing body width. Surface oil-flow patterns indicate

considerable cross-flow on the windward surface of the fuselage, even at this relatively low angle-of-attack. Thus, the local heat-transfer measurements have been divided by the theoretical value of the heat-transfer to the stagnation point of a sphere whose diameter is equal to the local body width. The fact that the experimental values, thus nondimensionalized, are essentially independent of streamwise coordinate (with the exception of the three upstream-most thermocouples) suggests that the local flow is similar to that for cylindrical configurations. Included for comparison is the swept cylinder theory:

$$\frac{\dot{q}}{\dot{q}_{t,loc}} = 0.707 F (\sin \alpha)^{1.2} \quad (3)$$

The factor  $F$ , which accounts for the noncircular shape of the cross-section has been assumed to 0.685 for all stations, the value for an Apollo-like cross-section (ref. 27). Because the cross-sections for  $x < 0.2L$  are more circular than the Apollo Command Module (as shown in Fig. 5), one would expect this simple theoretical approach to underpredict the heating near the nose (even if cross-section were the dominant parameter). This is true. The agreement between the data and the swept cylinder theory in Fig. 11b is considered adequate to demonstrate the importance of the cross-section geometry.

The heat-transfer rate in the leeward pitch plane is presented in Fig. 12 as a function of the angle-of-attack. Measured values (nondimensionalized using the local body width as the characteristic dimension) are presented for two thermocouples: one very near the nose at  $x = 0.1L$  and one well downstream, at  $x = 0.6L$ . At the higher angles-of-attack ( $30^\circ$  and above), the heat-transfer rate at the upstream thermocouple is roughly twice that at the downstream thermocouple. Included for comparison are the average values of the leeward

heat-transfer data for the simulated infinite cylinders C2 and C4 (whose leeward geometry is roughly that of the Apollo) at angles-of-attack of  $30^\circ$  and of  $60^\circ$  (ref. 23).

The heat-transfer-rate distribution in the leeward pitch plane is presented in Fig. 13. The influence of the canopy clearly perturbs the heating for an angle-of-attack of  $10^\circ$  (Fig. 13a). However, for both the  $30^\circ$  case and the  $50^\circ$  case, the data indicate higher heating near the nose, decreasing to an almost constant value for  $x \geq 0.4L$ . Again, at an angle-of-attack of  $30^\circ$ , the leeward heat-transfer values for the NAR 161B DWO are compared with the averaged experimental values for a simulated infinite cylinder.

#### Wing Flow Field

Alpha of  $0^\circ$  - The nondimensionalized heat-transfer-rate distributions measured in Tunnel B for the NAR 161B DWO at an alpha of  $0^\circ$ , which are presented in Fig. 14, are only weakly Reynolds number dependent. Data are presented for all the thermocouples on the wing leading edge, i.e.,  $s_w = 0.0$ , and for three thermocouples on the upstream fuselage in the plane of the wing. Based on the results of the experimental investigations of Hiers and Loubsky (ref. 5) and of Bushnell (ref. 9), one would expect a Type VI shock-interference pattern along the highly-swept leading edge of the delta wing orbiter at zero angle-of-attack. For a basic Type VI pattern, the heating increases "uniformly" in that portion of the leading edge subjected to the flow within the bow shock and there are no localized increases in heating. However, three localized peaks can be seen in the heat-transfer distributions presented in Fig. 14 for the wing leading edge. Local maxima, as recorded by the available thermocouples, occur at  $z_r = 0.05b$ , at  $z_r = 0.15b$ , and at  $z_r = 0.75b$ . To understand the flow field

mechanisms which create these localized heating increases, flow visualization photographs are needed. Unfortunately, the authors do not have any flow visualization results for this particular configuration. Fortunately, an excellent collection of shadowgraphs and oil-streak patterns are available for a similar configuration, the NAR 134 delta-wing orbiter (ref. 30). A sketch of the shadowgraph pattern for an alpha of  $0^\circ$  is presented in Fig. 15. (The reader is encouraged to go to the original report by Cleary for additional detail and for the corresponding oil-streak pattern.) The bow shock wave intersects the wing shock at  $z_r = 0.27b$ , point 3. In the vicinity of the interaction and continuing downstream (i.e., outboard along the leading edge), the interference pattern of the bow shock-wave and the wing shock-wave is consistent with the description by Bushnell (ref. 9) for a Type VI pattern. That is, the wing shock continues downstream of the intersection point and is deflected away from the wing leading-edge. Expansion waves (which are not visible in the shadowgraph) emanate from the intersection, impinge on the wing, and are reflected back. Thus, expansion waves interact with the wing leading-edge shock and turn it back toward the leading edge. Two additional traces are evident between the bow shock wave and the body. The one nearest the body originates at the upstream intersection of the wing-root fairing with the fuselage. The shock wave intersects the wing leading edge at  $z_r = 0.04b$ , point 1. A second wave, almost parallel to the first, intersects the wing leading-edge at  $z_r = 0.14b$ , point 2. Although this wave appeared on only one side of the fuselage (in the photograph of ref. 30) and did not have an identifiable origin, its presence is noted because the maximum heat-transfer measured on the wing leading-edge of the AEDC model was recorded at the thermocouple located where this shock intersects the wing.

The proposed shock-interference pattern for the NAR 161B at zero angle-of-attack is presented in Fig. 16. The sketch of Fig. 16 depicts

(in two dimensions) a flow field containing:

- (1) a shock wave originating at the leading edge of the wing-root fairing ( $x = 0.5L$ ) and impinging on the wing leading-edge near the first thermocouple ( $z_r = 0.05b$ ),
- (2) a shock wave which is associated with the compression of the flow in the convex corner formed by the wing fairing (the existence of which is justified as much by the heat-transfer data as by the flow-field photographs),
- (3) the intersection of the bow shock-wave and the wing leading-edge shock which occurs near  $z_r = 0.27b$ ,
- (4) expansion waves emanating from the intersection of the leading-edge shock with the bow shock, and
- (5) a shear layer which divides the flow passing on one side of the intersection from that passing on the other side.

Consider now the relation between this flow model and the heat-transfer-rate distribution along the leading edge of the wing, as presented in Fig. 14. The heating rates measured on the fuselage in the plane of the wing increased markedly at the two thermocouples at and downstream of  $x = 0.4L$ . This increase in heating is attributed to the shock wave associated with the intersection of the wing-root fairing with the fuselage (although the fairing itself begins further downstream, just aft of  $x = 0.5L$ ). It might be noted that a corresponding heating increase was measured at the thermocouples located in the pitch plane of the fuselage, at these  $x$  - stations, as shown in Fig. 9. The heating rate recorded at  $z_r = 0.1b$  on the leading edge of the wing is a relative low between the two localized "peaks" associated with the impingement of the two waves. As was observed in the investigations using a swept cylinder

mounted on a shock generator, there is no locally high heating-rate associated with the intersection of the bow shock-wave and the wing leading-edge shock (i.e., in the vicinity of point 3).

To help interpret the significance of the experimental heat-transfer-rate distribution for  $0.25b \leq z_r \leq 0.8b$ , curves which indicate the relative effect of (1) taper ratio and of (2) streamwise distance from the wing root are included in Fig. 14. Both effects were calculated relative to the experimental value of the heat-transfer rate at the midpoint of the exposed span. The effect of the taper ratio was estimated as follows. The leading-edge radius as a fraction of the local chord was assumed to vary linearly from a value of  $0.0089 c_l$  for the NACA 0009-64 (ref. 24) which is the airfoil section at wing station 249.75 (ref. 21) to a value of  $0.0158 c_l$  for the NACA 0012-64 airfoil section at wing station 561.85. Multiplying the fractional value for the leading-edge radius at a particular station by the local chord length yielded the spanwise distribution of the leading-edge radius. The spanwise heat-transfer distribution was assumed to vary inversely as the square root of the leading-edge radius, thus calculated. Because the heat-transfer rates measured on "simulated" infinite cylinders at  $60^\circ$  sweep have been found (ref. 23) to be in excellent agreement with the theoretical distribution which was dependent on the streamwise distance from the apex, an estimate of this effect on the wing leading-edge heating has been calculated. To calculate the heating variation due to this effect, it was assumed that the viscous layer originated at  $z_r = 0$  and that the effective radius of the leading edge was constant (and equal to the empirical value determined using the heating rate measured at midspan). Adding the two effects (and neglecting interdependence) in the midspan region yields an essentially constant heat-transfer distribution, which is consistent with the data in this region.

The Type VI interference flow field model also includes an expansion fan and a shear layer. The present authors associate the "relatively low" heating rates at  $z_r = 0.25b$  with the expansion fan and the "relatively high" heating rates at  $z_r = 0.75b$  with the effect of the shear layer.

The flow mechanisms which produced the perturbations in the leading-edge heating continued to influence the heat transfer downstream on the wing surface, as indicated by the data presented in Fig. 17. Included in the figure is an arrow approximating the streamline which originates at  $z_r = 0.15b$ , i.e., at the peak heating on the leading edge. The streamwise direction was determined using the oil-streak patterns presented by Cleary (ref. 30). Proceeding downstream, the "streamwise" arrow continues to pass through the local maximum values of heating. Locally high heating rates were also measured on the wing surface at the thermocouples in the vicinity of  $z_r = 0.75b$  for  $s_w < 0.4 c_l$ . This increase in heating to the wing surface indicates that the flow mechanism which perturbed the leading edge heating in this region also influenced the downstream flow.

Alpha of 30° - Although additional complications are introduced by the three-dimensional character of the flow when the vehicle is at 30° angle-of-attack, the shock-interference patterns retain the essential features described thus far. In addition to the parameters of configuration geometry which affected the flow field at an alpha of 0°, parameters which characterize the windward surface of the fuselage:wing geometry become important at 30° angle-of-attack.

The "location" of the intersection of the fuselage-generated shock wave with the wing-generated shock wave is presented in Table 3 for several space-shuttle configurations. Note that the wing planform and the leading-edge sweep angle are interrelated, i.e., the straight-wing configurations are of relatively low sweep and the delta-wing orbiters are of relatively high sweep. As a rule

of thumb, for a given flow, the intersection location determined using a flow-field photograph would be inboard of the location determined using the heating to the leading-edge. Comparison of the intersection location for the straight-wing orbiter with that for the delta-wing orbiter (as obtained in the VAC HVWT during the present investigation) indicates that the intersection moves outboard as the wing sweep increases. These two configurations have identical fuselages. Furthermore, at  $30^\circ$  angle-of-attack the fuselage-generated shock wave is assumed to be essentially independent of the wing planform. Therefore, because the wing leading-edge "moves" further aft as the sweep angle increases, it intersects the fuselage-generated shock wave at a point further from the pitch plane.

That the width of the fuselage at the wing juncture is an important parameter in correlating the location of the shock:shock intersection is indicated in Table 3. If the locations of the shock:shock interactions for the two 040 delta-wing orbiters whose leading-edge sweep is  $50^\circ$  (ref. 32) are defined as the distance from the pitch plane in terms of fuselage half-widths, i.e.,  $z_a/0.5W_b$ , the values are consistent with those for the other delta-wing configurations. If these locations are presented as the fractional distance from the root of the exposed wing (the values for this parameter are designated by the \* in Table 3), the results do not correlate. It is not surprising that the parameter  $z_r/b$  does not provide a satisfactory correlation, since the wing span (relative to the fuselage width) of the two 040 configurations of ref. 32 is much greater than the wing spans for the other two delta-wing orbiters. Specifically, the ratio of the fuselage half-width ( $0.5W_b$ ) to the complete wing semi-span ( $0.5W_b + b$ ) is 0.161 for the two 040 DWOs, 0.333 for the F3:W4 DWO, and 0.382 for the NAR 134 DWO.

The curvature of the windward surface of the fuselage also affects the shock-intersection location, as can be seen in the results for the two  $60^\circ$ -



sweep delta-wing orbiters. The NAR 134 DW0, which was used by Cleary (ref. 30), has a relatively slender nose with a slightly rounded underbelly. The fuselage cross-section for the F3:W4 delta-wing orbiter is uniform (except near the nose, which is also blunt) with a flat windward surface. As a result, the bow shock-wave for the F3:W4 DW0 is flatter and, therefore, intercepts the plane of the wing leading-edge further from the pitch plane. The greater breadth of the fuselage-generated shock wave for the F3:W4 is illustrated by the photographic traces of the fuselage-generated shocks for the two configurations, which are presented in Fig. 18. Also indicated in Fig. 18 are the shock:shock intersection locations for the two configurations. Because the photographic trace (feature number 1) represents the contour of the fuselage-generated in a plane in the lee, the location of the shock:shock intersection (feature number 3) is well inboard of the photographic trace of the bow wave.

As was reported in ref. 17, the photographic trace of the bow shock-wave depends on the nose geometry. Differences in nose geometry which can affect the photographic trace of the bow wave do not necessarily significantly alter the location of the intersection associated with the intersection of the fuselage-generated shock wave with the wing-generated shock. For a given wing, the geometry of the fuselage near the wing junction determines the local shape of the fuselage-generated shock and, hence, the resultant shock:shock intersection location.

The sweep angle of the wing governs (to first order) the type of interference pattern. The effective sweep angle has, therefore, been calculated as a function of angle-of-attack using:

$$\cos \Lambda_{\text{eff}} = \sqrt{\tan^2 \Lambda \sin^2 \alpha + 1} \cos \Lambda \quad (4)$$

The relation was developed for a right-circular cylinder of constant cross-section. The shock-interference patterns obtained for cylinder mounted on a

shock generator are presented as a function of sweep angle as a guide to categorize the wing data (at zero angle-of-attack) and is included in Fig. 19. Referring to Fig. 19, one would expect that the shock-interference pattern for a delta-wing configuration at an  $\alpha$  of  $30^\circ$  would be a Type VI. For a straight-wing configuration, the interference pattern could be either Type IV or Type V, depending on the leading-edge sweep. (The actual pattern which exists and the attendant perturbation in heat transfer will be affected by the three-dimensional character of the flow.) Because of the basic differences in the shock-interference patterns, the discussion will subsequently be divided into (a) delta-wing configurations and (b) straight-wing configurations.

(a) Delta-wing configurations - The flow-field features are presented in Fig 18 for two delta-wing orbiters whose leading edge sweep is  $60^\circ$ . The shock interference patterns for the two configurations are similar and are consistent with the features of a Type VI pattern. That is, the wing-generated shock continues downstream of the intersection point and is deflected away from the wing leading-edge. Expansion waves (which were not visible in the photographs) interact with the wing leading-edge shock and turn it back toward the leading edge. The flow-field features include:

- (1) the bow shock-wave,
- (2) that portion of the wing-generated shock wave which is inboard of the shock:shock intersection,
- (3) the "point" at which the fuselage-generated shock wave intersects the wing-generated shock wave,
- (4) that portion of the wing-generated shock wave which is outboard of the shock:shock intersection, and
- (5) the photographic trace of the curve defining the intersection of the fuselage-generated shock-wave surface with the outboard portion of the wing-generated shock-wave surface.

Included in the sketch of the NAR 134 flow-field is a sixth feature, the trace of the fuselage-generated shock wave in the plane of the intersection "point", i.e., point 3.

The differences in the wing-root geometry cause significant differences in the inboard trace of the leading-edge shock. Two progressively steeper shock waves are evident (ref. 30) in the flow in the compression corner created by the wing-root fairing on the NAR 134 model. These waves intersect the wing leading-edge at points which correspond closely to the location of the maximum heating-rate, as measured on the wing leading edge of the NAR 161B (refer to the data from Tunnel B, which are presented in Fig. 20). Thus, this heating perturbation is attributed to the interaction between these shock waves and the boundary layer. For the F3:W4, the trace of the leading-edge shock inboard of the intersection location is essentially linear along its entire length. Thus, the supersonic flow along the fuselage, which has passed through the relatively flat, fuselage shock-wave, encountered the abrupt turning angle of the wing leading-edge. The abrupt turning of the flow was apparently accomplished by the single shock wave. Unfortunately, heating-rate data from the wing-root region are not available for the F3:W4.

The spanwise heat-transfer-rate distributions along the wing leading-edge are presented in Fig. 20 for the NAR 161B DW0 and for the F3:W4. The leading-edge sweep angle is  $60^\circ$  for both configurations. The nondimensionalized heat-transfer rates obtained in Tunnel B of AEDC for the NAR 161B are essentially independent of Reynolds number. The nondimensionalized data reported by Lockman and DeRose (ref. 25) for the NAR 161B are also essentially independent of Reynolds number. Unfortunately, data from the Ames tests were not available for the two thermocouples which yielded the highest heating rates in the Tunnel

B tests. Nevertheless, the experimental distributions obtained in the two facilities appear to be similar, although the values of ref. 25 are consistently higher (whereas the data from the fuselage pitch-plane of Fig. 9b are in good agreement).

To understand the flow-field for the NAR 161B DW0 at an  $\alpha$  of  $30^\circ$ , let us examine the Tunnel B data in more detail. In addition to the leading-edge measurements of Fig. 20, consider also the heat-transfer distribution over the windward surface of the wing, which is presented in Fig. 21a. Because the heat-transfer measurements for the Tunnel B tests were essentially independent of Reynolds number, contours are presented in Fig. 21a for only one test condition. A "streamline" arrow based on the oil-streak patterns of Cleary (ref. 30) has been included in this figure.

Three localized peaks can be identified in the experimental heat-transfer-rate distributions along the wing leading-edge. The local maxima occurred (1) at  $z_r = 0.15b$ , (2) at  $z_r = 0.55b$ , and (3) at  $z_r = 0.75b$ . The first peak is attributed to an interaction between boundary layer and the "lambda" shock of the compression corner, noted previously. The perturbation appears to be limited to a small region near the leading edge. The second peak was recorded by the thermocouple located where the curve defining the intersection of the two shock surfaces crossed the wing leading-edge (flow-field feature number 5 of Fig. 18b). The most extensive perturbation in heating occurred in the region downstream of this thermocouple, as can be seen in the heat-transfer contours of Fig. 21a. The heating rate measured at  $z_r = 0.75b$  appears to be relatively high because the heating rates at the adjacent thermocouples are actually relatively low. These relatively low heating rates may be the result of the expansion waves associated with the Type VI interference pattern.

The shock-interference pattern represented by the heat-transfer data of Figs. 20 and 21a for the NAR 161B is consistent with that indicated by the paint data presented in ref. 32 for the two 040 DWOs. Thus, moving spanwise near the leading edge, one encounters:

(1) a region of increased heating (for  $0.45b < z_r < 0.6b$  for the NAR 161b), depicted by the lines of constant heating "moving" further downstream onto the wing,

(2) followed by a region of decreased heating (for  $0.6b < z_r < 0.7b$ ), depicted by the contours "moving" toward the leading edge, and

(3) then a return to the "normal" heating rates.

The heat-transfer data obtained in Tunnel B for the NAR 161B indicate the perturbed heating in region (1) is approximately 1.5 times the undisturbed values along the same constant chord line and is approximately twice the value in the region of decreased heating, i.e., region (2). Using paint data, Brevig et al (ref. 31) found that peak heat-transfer coefficient in the interference area (which was at about 30% exposed span and 10% chord) was "at least two times the heat-transfer coefficient outside the interference region along the same constant chord line". The differences in the heating perturbations are attributed to the variations in geometry between the two configurations, especially differences between the leading-edge sweep angles (which is  $53^\circ$  for the GDC model and  $60^\circ$  for the NAR 161B).

It might be noted that the heating rates in the vicinity of the wing root for the NAR 161B DWO are markedly different from those reported in ref. 32 for the DWOs. No locally high heating rates are evident in the lines of constant heating based on the thermocouple measurements for the NAR 161B (Fig. 21a). Furthermore, paint data obtained in Tunnel B (ref. 33) indicated no locally high heating rates in the vicinity of the wing root for the NAR 161B. However, the constant heating contours based on the paint data of ref. 32

indicate significant increases in the wing-root heating for the 040 DWOs tested in Tunnel B. Photographs presented in ref. 31 showing the phase-change patterns on a delta-wing booster as a function of time also indicate increased heating near the wing root. These differences indicate the importance of properly designing the wing-root fairing, since the heating was perturbed over a large region.

The dimensionless heating-rates measured on the leading edge of the F3:W4 are of the same order as the values obtained for the NAR 161B. However, because of the limited instrumentation available, the leading-edge heating rates for the F3:W4 provide little information regarding the shock interference pattern. The local increase in wing heating associated with the flow perturbation at the juncture of the fuselage-generated shock wave with the wing-generated shock wave observed for the NAR 161B also occurred for the F3:W4, as can be seen in Fig. 21b in the heating rate and the surface pressure measured by the sensors located at  $z_r = 0.8b$ ,  $s_w = 0.25c_\ell$ . That this is due to shock interaction can be seen by following the photographic trace of the curve which defines the intersection of the fuselage-generated shock wave and the wing-generated shock wave (flow field feature 5) onto the wing.

(b) Straight-wing configurations - Referring to the effective sweep-angle relations presented in Fig. 19, one would expect a Type V interference pattern to exist for a straight-wing configuration at an angle-of-attack of  $30^\circ$ . Data presented by Marvin et al in ref. 13 for the NAR straight-wing orbiter, which has a leading-edge sweep angle of  $22^\circ$ , are reproduced in Fig. 22. Three distinct "dividing" traces are evident in the surface oil-flow pattern on the windward wing-surface as a result of the body and wing-shock interaction. Marvin et al reported that the pressure measured at the 25% exposed semi-span was 1.45 times the normal-shock pressure. In addition, the highest experimental heat-transfer rates were obtained at the 25% exposed semi-span, with the measurement

at the 10% chord being slightly greater than that measured at the 0% chord. These peak values for the surface pressure and for the heating rate were located just downstream of the inboard-most trace in the oil-flow pattern (designated as "a" in the sketch of Fig. 22a). The data suggests that this inboard-most trace is caused by the downstream shock wave of the Type V shock-interference pattern (Fig. 22c). Having assumed a Type V pattern exists, the other two traces which appear in the oil-flow pattern are (b) the shear layer and (c) the jet, respectively.

Categorizing the shock-interference phenomena in terms of the patterns identified by Edney correlates, at least approximately, the data near the wing leading-edge, where the most significant perturbations in surface pressure and in heat transfer occur. When presenting data for the NAR straight-wing orbiter, Marvin et al (ref. 13) note: "Although the flow over the wing is complex, the highest temperatures are confined to regions between 0% and 25% chord." It is likely that the flow field features change, or are modified, as the complex, three-dimensional flow expands downstream. Although the "three" dividing traces, which are evident in the oil-flow patterns, continue to the trailing edge, the spanwise variations in surface pressure and in heat transfer are markedly less severe downstream of 25% chord (ref. 13).

Surface-pressure and heat-transfer-rate measurements obtained in the VAC HVWT for the F3:W2 at an alpha of  $30^\circ$  are presented in Fig. 23. Since the leading-edge sweep angle is  $15^\circ$ , one would expect a Type V shock-interference pattern. Because of the close proximity of the leading-edge shock wave to the surface, only the location of the shock:shock intersection at the wing leading-edge could be determined from the schlieren. From this intersection point, three "dividing" traces have been sketched onto the wing planform, representing: (a) a shock wave, (b) a shear-layer, and (c) a jet. Since oil-flow patterns were not

made during the VAC tests, the oil-flow patterns of Marvin et al (ref. 13) were used as a guide. Thus, the three traces are considered as approximations, at best. Nevertheless, the surface pressures and heating rates substantiate their existence, at least in a broad sense. Note that the highest pressure and the highest heating rate (for thermocouples other than those on the leading edge) were recorded by those sensors located at  $z_r = 0.2b$  and  $s_w = 0.25c_\ell$  (refer to Fig. 3b). The measured pressure at this orifice was  $0.72 p_{t2}$ , which is twice the value calculated for flow past a  $30^\circ$  wedge with an attached shock wave (ref. 34). This location is just downstream of the assumed location of the shock wave trace. The surface pressure measured at  $z_r = 0.2b$  and  $s_w = 0.75c_\ell$  (the downstream orifice between traces "a" and "b") is relatively low. The experimental pressures in this region of the NAR straight-wing orbiter, as reported by Marvin et al (ref. 13), also appear to be relatively low. In addition, for both configurations, the heat-transfer rates in the vicinity of trace "c" (the assumed jet) appear to be slightly lower than the undisturbed values.

Heat-transfer data are available (ref. 15) for a NASA straight-wing orbiter whose geometry in the region governing the wing:fuselage shock interaction is roughly similar to that of F3:W2. The wing of the NASA configuration, which is swept  $14^\circ$ , is offset from the windward surface of the fuselage and has a  $7^\circ$  dihedral. The spanwise heat-transfer-rate distributions for  $s_w = 0.15c_\ell$  are presented in Fig. 24. Two localized heating peaks are clearly evident in the data obtained at the higher Reynolds number. The measurements for the lower Reynolds number exhibit one definite peak with a second, less obvious peak. The maximum heating increase occurs at the inboard peak, which would correspond to the shock-wave trace of the Type V pattern. The fact that the region of perturbed heating is further outboard for the NASA straight-wing orbiter than for the F3:W2 is attributed to the  $7^\circ$  dihedral and the slight



offset of the wing. Thus, the fuselage-generated shock wave would be expected to intersect the wing leading-edge at a point further outboard than was observed for the flush-mounted, zero-dihedral wing of the F3:W2. Because the windward surface of the fuselage is flat, the intersection of the fuselage-generated shock wave with the plane of the wing would be very sensitive to wing offset and dihedral. While the differences in the experimental heat-transfer rates obtained during these two runs are significant at specific points in the regions where the heating is perturbed, the heat-transfer rates measured in the unperturbed regions exhibited significantly less variation. The consistency of the unperturbed heating is indicated in Fig. 25 in which are presented constant heating-rate contours. The effects of flow-field perturbations on the heating in the wing-root regions are greater for the low Reynolds number test.

Alpha of 50° - The "location" of the intersection of the fuselage-generated shock wave with the wing-generated shock wave is presented in Table 4 for several space shuttle configurations at an angle-of-attack of 50°. Comparing the locations determined in the present program for the two straight-wing orbiters having in common the F3 fuselage indicates that sweeping the leading edge has a slight effect on the intersection location at this angle-of-attack. There is a significant difference in the shock:shock interference locations for the F4:W2 which is attributed to a difference between the models tested in the two facilities. Based on a post-test examination of the models, the windward-most points of the wing cross-section were tangent to the plane of the maximum-width location for the F4-fuselage of the model tested in the Martin-Marietta facility, while the chord line of the wing was in the plane of the maximum-width location for the model tested in the VAC HVWT. Thus, since the wing of the Martin-Marietta model is more offset, the "point" at which the fuselage-generated shock wave intersected the wing leading-edge

is further outboard. The location of the "u-shaped" burn pattern at the leading edge of the wing (as determined by the present authors' from the post-test photograph of the Martin-Marietta model) is in excellent agreement with the shock:shock intersection location obtained by Kessler et al (ref. 16) using the schlieren photographs from the same tests. For all but one of the configurations for which data are available, the intersection is nearer the pitch plane for the higher angle-of-attack. The exception was the intersection location for the NAR 134 delta-wing orbiter, as determined by the present authors using the shadowgraphs presented by Cleary in ref. 30.

(a) Delta-wing configurations - As the angle-of-attack is increased, the shock-wave envelope for the shuttle entry configuration changes from a surface consisting of two intersecting waves with both components clearly identifiable, i.e., a fuselage-generated shock wave and a wing-generated shock wave, to a single, albeit complex, shock surface. The data indicate that an  $\alpha$  of  $50^\circ$  is in the range where the transition occurs for the delta-wing configurations. Doughty et al (ref. 20) discussed the effects of shock:shock interaction at an  $\alpha$  of  $40^\circ$  and  $50^\circ$ , but noted that bow-shock impingement was not observed at angles-of-attack of  $60^\circ$ , and greater. A region of increased heating appeared in the paint data which were presented by Brevig et al (ref. 31). It was noted that the hot spot due to the shock interaction phenomena was much less severe at the higher angles-of-attack and that, as the angle-of-attack increased, the peak heating location moved toward the leading edge and inward toward the fuselage. Except for a region of perturbed heating near the wing root, the contours of the phase-change patterns obtained in Tunnel B for the 040C at an  $\alpha$  of  $50^\circ$  ran parallel to the wing leading-edge (ref. 32). These patterns indicate there was no appreciable shock:shock interaction for this particular configuration.

The data for the F3;W4, i.e., the VAC delta-wing orbiter, are presented in Fig. 26 for an angle-of-attack of  $50^\circ$ . The wing leading-edge shock wave is curved and detached, but appears to extend all the way to the wing root. The existence of a leading-edge shock wave in this region indicates that the flow behind the fuselage-generated shock wave is supersonic even at this high angle-of-attack. Such a conclusion is consistent with the pitot-pressure measurements obtained by Cleary (ref. 35), which indicate that the surface Mach number is approximately 1.5 at  $x = 0.6L$  in the pitch plane of the NAR 134 delta-wing orbiter. The "splitting" of the leading-edge shock wave, which can be seen near the wing tips, is attributed to the shock:shock interaction. For the few points available, the experimental heating-rate distribution for the wing leading-edge exhibits a definite peak. At the thermocouples which are located along a "streamline" originating at that leading-edge thermocouple the heat-transfer measurements appear to be slightly higher than the values at neighboring thermocouples. Again, because oil-flow patterns were not obtained for these tests, the photographs presented by Cleary (ref. 30) were used as a guide. Although the heating perturbation approaches the expected accuracy of the experimental values (based on the authors' experience, the "expected" accuracy of heat-transfer measurements from this type of facility is approximately 15%), the localized heating increases are noted because they seem to be related to a flow mechanism. Neither the surface pressure measurements nor the schlieren photograph indicate the cause of the heating perturbation. With the exception of the pressure measured at the outboard orifice, the pressure data compare favorably with the modified Newtonian value,  $0.588 p_{t2}$ .

Cleary (ref. 30) observed "no significant visible effects of wave interaction with the windward surface of the wing" for an  $\alpha$  of  $45^\circ$ . This statement apparently refers to the oil-flow patterns on the wing surface, since a

definite change occurred in the leading edge shock wave near the mid-span of the exposed wing. As indicated in Fig. 27, which is a sketch representing Cleary's data, both the strength (as indicated by the intensity of the shadow-graph trace) and the slope of the leading-edge shock wave change due to the interaction with the fuselage-generated wave. The leading-edge shock trace is evident only for a short distance inboard of the shock-shock intersection. The absence of a shock-wave trace is attributed to the further deceleration in the region of the wing-root fairing of the flow which had already been decelerated to transonic speeds by the fuselage-generated shock wave.

The spanwise heat-transfer distributions along the leading edge of the  $60^\circ$ -sweep delta-wing orbiters are presented in Fig. 28 for an  $\alpha$  of  $50^\circ$ . At this high angle-of-attack, the "stagnation line" has moved off the airfoil nose and aft onto the windward surface, as indicated by the oil-flow pattern of Cleary (which was sketched in Fig. 27) and supported by the heat-transfer data for the windward surface of the wing, which are presented in Fig. 29. Despite differences in geometry, the nondimensionalized heat-transfer rates measured on the leading edge of the F3:W4 are approximately the same as the values for the NAR 161B. Furthermore, the nondimensionalized heat-transfer distributions obtained in Tunnel B are similar to the two lower Reynolds-number distributions from the Ames facility reported by Lockman and De Rose (ref. 25), although as was the case for an  $\alpha$  of  $30^\circ$ , the values of ref. 25 are consistently higher. The high heat-transfer rates observed along the wing leading-edge at the highest Reynolds number for which data were obtained indicate boundary-layer transition has occurred. The heat-transfer distribution for the turbulent boundary-layer is qualitatively similar to the laminar distributions, having similar locations of relative maxima and of relative minima. The similarity between the laminar data and the turbulent data indicates that the

heat-transfer distribution is governed by the "inviscid flow-field" (where the intersecting shock waves and the associated shear layers have been included in the "inviscid flow-field") rather than by interactions between the inviscid flow and the wing boundary-layer.

Three localized peaks can be identified in the experimental heat-transfer-rate distributions along the wing leading-edge. Although the heating perturbations are relatively small, the governing flow mechanisms appear to be the same as those observed at an  $\alpha$  of  $30^\circ$ . Specifically, the local maxima and their causes are:

- (1)  $z_r = 0.15b$ , which is attributed to the compression in the corner formed by the wing-root fairing,
- (2) at  $z_r = 0.50b$ , which is associated with the shock:shock interaction (note that this thermocouple is very near the intersection location observed in the shadowgraph of Cleary, refer to Fig. 27), and
- (3) at  $z_r = 0.75b$ , which appears to be a relative local maxima because the heating rates at the adjacent thermocouples are actually relatively low.

At an  $\alpha$  of  $50^\circ$ , the heat-transfer distribution over the windward surface of the wing is complicated by the onset of transition. Because the heat-transfer data were Reynolds-number sensitive, contours are presented in Fig. 29 for both flow conditions. A limited region of increased heating occurs near the leading-edge in the vicinity of the shock:shock intersection. Further outboard (in the vicinity of  $z_r = 0.7b$ ) the relatively low heating-rates near the leading edge suggest the presence of expansion waves.

Chordwise heat-transfer distributions are presented in Fig. 30 for those thermocouples located at 25% exposed span, 50% exposed span, and 75% exposed

span. Heat-transfer measurements from the Ames 3.5-ft. Hypersonic Wind Tunnel (ref. 25) are included in Fig. 30 for comparison. These data provide insight into the transition process. At the lower Reynolds number tested, the boundary layer is laminar for the entire windward surface of the wing. As the Reynolds number is increased, transition occurs downstream near the trailing edge of the wing, as indicated in the heat-transfer distribution from Tunnel B for  $Re_{\infty,L} = 6.22 \times 10^6$ . Not surprisingly in view of the many variables which affect the transition location, e.g., ref. 36, the measurements from the two facilities yield different transition criteria, since the Ames data at a  $Re_{\infty,L} = 8.42 \times 10^6$  indicate the boundary layer is wholly laminar, while boundary-layer-transition effects appear in the Tunnel B when  $Re_{\infty,L} = 6.22 \times 10^6$ . Since the local chord lengths,  $c_l$ , are 0.51 ft, 0.38 ft, and 0.25 ft, for  $z_r = 0.25b$ ,  $z_r = 0.50b$ , and  $z_r = 0.75b$ , respectively, the wetted distance from the stagnation line to the transition location is roughly the same for each station. The onset of transition progresses upstream, until finally the boundary layer along the "stagnation line" itself becomes turbulent (which has occurred at the highest Reynolds number of the Ames tests). The transition patterns indicated by the heat-transfer measurements for the NAR 161B differ markedly from those observed by Doughty et al (ref. 20). Recall from the brief discussion of ref. 20 in the "Introduction", that the boundary layer "tended toward a laminar condition within the bow-shock field and a turbulent condition outboard of the shock".

The chordwise heat-transfer distributions support the conclusion that the stagnation line has moved off the leading edge, a conclusion based originally on the oil-flow patterns of Cleary. Providing the flow over the wing is either laminar or turbulent, the maximum heating rate for each of the three spanwise stations occurs at the thermocouple at  $s_w = 0.1c_l$ . Of course, when transition occurs on the wing surface, the peak heating occurs where the boundary layer becomes turbulent.

(b) Straight-wing configurations - The angle-of-attack at which the shock-wave envelope changes from a surface consisting of two identifiable component waves to a single, complex surface appears to be greater for the straight-wing configurations. The value of  $\alpha$  at which this change occurs is affected by many geometric parameters including: the wing planform area, the leading-edge sweep, wing offset and dihedral, and the curvature of the windward surface of the fuselage. Using a (truncated) model of an MSC orbiter configuration, Henderson et al (ref. 37) found that large regions of interference heating occurred at an  $\alpha$  of  $40^\circ$  due to bow-shock impingement but did not occur at an  $\alpha$  of  $60^\circ$ . It was noted further that electron-beam flow-visualization studies indicated a change of flow pattern at an  $\alpha$  between  $50^\circ$  and  $60^\circ$ . Schlieren photographs from the VAC HVWT are presented both for the F3:W2 and for the F3:W3 at an  $\alpha$  of  $50^\circ$  in Fig. 31 and for the F3:W2 at an  $\alpha$  of  $60^\circ$  in Fig. 32. At an  $\alpha$  of  $50^\circ$ , shock:shock intersections are clearly evident for both configurations. However, one could not establish the existence of shock:shock interaction using the flow field photograph for this flat-bottomed configuration at an  $\alpha$  of  $60^\circ$ . Furthermore, the standoff distance for the wing-generated shock wave is significantly greater than it was at an  $\alpha$  of  $50^\circ$ . Scottoline et al (ref. 38) found no fuselage-shock:wing-shock interference effects in the heat-transfer distributions obtained at an  $\alpha$  of  $60^\circ$  using the phase-change paint technique for a NAR swept-wing orbiter. It might be noted that the leading-edge sweep angle for this NAR configuration is  $45^\circ$ , which is closer to the sweep angles typical of the delta-wing configurations rather than to the typical values for the straight-wing configurations. However, heat-transfer-rate measurements reported by Seegmiller (ref. 14) and by Rogers (ref. 15) indicated

increases in the local heating due to shock:shock interaction phenomena at angles-of-attack up to  $70^\circ$  for MSC orbiter configurations (which have wing offset and dihedral).

The surface pressures and the heat-transfer rates measured on the wing of the F3:W2 at an  $\alpha$  of  $50^\circ$  are presented in Fig. 33. Although the instrumentation is not sufficient to define the shock-interference pattern, the data clearly indicate the existence of a shock:shock intersection. Also included in the figure are three "dividing" lines originating at the shock:shock intersection location as determined from the schlieren of Fig. 31. Using very approximate models of the shock-wave structure, the calculated pressure at the inboard spanwise-station varies from  $2.4 p_{t2}$  at the "stagnation line" to  $0.53 p_{t2}$  at points far downstream of the leading edge. At  $z_r = 0.2b$ , the measured pressures are  $1.226 p_{t2}$  at the quarter chord and  $0.544 p_{t2}$  at the three-quarter chord. Thus, the pressure data indicate that trace "a", the inboard-most trace, is due to a shock wave, which becomes progressively weaker as one proceeds downstream. The pressure measurements at the other two spanwise stations appeared to be essentially unaffected by the shock:shock interaction. If one assumes that the shock-interference pattern is a Type V (an assumption based primarily upon the photographs of the leading-edge flow-field and the presence of three dividing traces in the oil-flow patterns) then trace "b" corresponds to the shear layer and trace "c" corresponds to the jet. The flow phenomena which cause the variations in the heat-transfer rates along the (assumed) shear layer are not understood at present. However, as indicated in Fig. 34, considerable variations are evident in the heat-transfer rates measured at this station,  $z_r = 0.2b$ , for all three tests employing W2-configurations. Thus, the variations at this station are attributed to a complex interaction between the shock-interference pattern and the flow perturbation associated with the wing root.



The surface pressures and the heat-transfer rates measured on the wing are summarized in Fig. 34 for all three tests at an alpha of  $50^\circ$  for the configurations using the W2 wing. With few exceptions, the similarity of the chordwise heat-transfer distributions at the stations  $z_r = 0.4b$ ,  $0.6b$ , and  $0.8b$ , indicates these limited variations in geometry and in test conditions have little effect on the heat transfer. The pressure measurements appear to be independent of the limited variations in geometry and in test conditions for all six orifices, even at the upstream, inboard orifice, where the perturbed pressure indicates the existence of a shock:shock interaction.

The surface pressures and the heat-transfer rates measured on the F3:W3 at an alpha of  $50^\circ$  are presented in Fig. 35. The pressure data give no indication of a shock-interference pattern. However, a flow-field perturbation is evident in the heat-transfer measured at the upstream thermocouple at  $z_r = 0.6b$ . It might be noted that the shock:shock intersection location determined using the schlieren photograph was  $z_r = 0.2b$  for this "highly-swept" straight-wing configuration.

The surface pressures and the heat-transfer rates measured on the configurations using W2 wings are presented in Fig. 36 for an alpha of  $60^\circ$ . At this angle-of-attack, there was no shock:shock interaction (of the type observed at the lower angles-of-attack) evident in the schlieren photograph of Fig. 32. The post-test photographs of the F4:W2 model tested in the Martin-Marietta Hotshot Wind Tunnel also indicated the absence of the shock:shock intersection. That is, there was no region near the midspan of the exposed wing where the model surface had degraded due to locally high heating, as was the case at an alpha of  $50^\circ$ , e.g., refs. 16 and 17. However, the pressure measurements for the upstream orifice (i.e.,  $s_w = 0.25c_\ell$ ) located at  $z_r = 0.2b$  for the VAC models are higher than the values at the upstream orifices at the other spanwise

stations. As was the case at an alpha of  $50^\circ$ , the heat-transfer-rate measurements presented in Fig. 36 for the  $z_r = 0.2b$  spanwise station reflect significant flow-field perturbations. The perturbations are due, at least in part, to wing-root interference as evidenced by the fact that the heat transfer at the downstream thermocouple exhibits the greatest variation and is greatest in the corner formed by the junction of the curved fuselage with the offset wing for the F4:W2 configuration. The problem of wing-root heating at high angles-of-attack has been reported previously. Henderson et al (ref. 37) noted that the "intensity of the interference flow at the body:wing juncture is, if anything, increased as alpha increases to  $60^\circ$ ". Seegmiller (ref. 14) found that, at an alpha of  $60^\circ$ , the maximum heating occurred in the root-interference region, with the most significant interactions occurring in the inner 10% of the span.

It has been observed (ref. 14) that "the major shock-interference heating effects at  $60^\circ$  angle-of-attack occur on the wing between about 25% and 55% span and forward of the 30% chord location". Therefore, the spanwise heat-transfer distributions for the instrumentation locations nearest the quarter-chord are presented in Fig. 37 for a variety of straight-wing configurations at an alpha of  $60^\circ$ . If one measurement from the VAC program is assumed to be an errant value (the triangular symbol which appears to be low), then the experimental distributions for the VAC models agree approximately with the distribution reported by Marvin et al (ref. 13) for an NAR straight-wing orbiter. For these configurations, the heating is a relative minimum in the midspan region. No effect of shock:shock intersection is evident in the heat-transfer distribution for the few available sensors. However, as noted previously, local increases in the heating rate distributions are evident in the data of Seegmiller (ref. 14) and of Rogers (ref. 15). These data were obtained on the MSC straight-wing orbiter at chordwise locations upstream of the other data.

### Additional Measurements for the Delta-Wing Configurations

The chordwise heat-transfer distributions calculated using the Eckert-reference-temperature distributions in the "modified" flat-plate relations (the modification being the calculation of local flow conditions using experimental pressures) were found to be in reasonable agreement with the nonperturbed data for the straight-wing configurations (ref. 17). The chordwise heat-transfer distributions are presented in Fig. 38 for the delta-wing configurations at an alpha of 30°. It is evident that flat-plate theory does not provide a satisfactory correlation of the heat-transfer measurements. A similar lack of correlation occurred for the data at other angles-of-attack, although the data are not presented. The chordwise heat-transfer distributions are presented in terms of (a) the distance from the leading edge as a fraction of the local chord lengths,  $s_w/c_l$ , (b) the actual distance from the leading edge,  $s_w$ , and (c) the distance from the leading-edge in terms of the leading-edge radius for the spanwise station of interest,  $s_w/r_{le}$ . The latter parameter,  $s_w/r_{le}$ , which is often used in correlating data on a flat plate with a rounded leading-edge, appears to provide the best correlation of the data.

As mentioned when discussing the "Model Program", two problems were encountered during the phase of the VAC HVWT tests conducted after the tunnel modification: (1) wrinkling of the model skin and (2) uncertain flow quality at high Reynolds number. The chordwise heat-transfer distributions for the VAC DWO, i.e., the F3:W4, are presented in Fig. 39 for an alpha of 30° and for an alpha of 50°. The lower-Reynolds-number data have been discussed previously. Based on the higher-Reynolds-number heat-transfer data, one would conclude that the boundary layer is turbulent for both angles-of-attack, even at some thermocouples along the leading edge. However, the surface pressures obtained at the high Reynolds

number of the VAC tests (refer to Table 5) are questionable. The high-Reynolds-number pressure measurements differ markedly from Newtonian values, while the low-Reynolds-number data are in approximate agreement, as expected. Furthermore, for both angles-of-attack, the data of Figs. 21 and 29 indicate that the boundary layer was laminar on the windward surface of the wing for the NAR 161B DWO at Reynolds numbers greater than those of the VAC tests. Thus, the validity of the high-Reynolds-number data is subject to question. However, for completeness, complete tabulations of the surface pressures and of the heat-transfer rates are presented in Tables 5 and 6, respectively.

## SUMMARY

The analysis of heat-transfer data, surface-pressure measurements, and flow-field photographs for a variety of space-shuttle entry configurations indicates that the shock-interference patterns exhibit many of the characteristics of the patterns identified by Edney. For the shock:shock interaction on the wing, the shock wave generated by the bow of the shuttle serves as the impinging shock. Therefore, because it is at low angles-of-attack that the bow shock of the shuttle corresponds most closely to the wedge-generated shock wave in the studies of Edney, the analysis began with the low angle-of-attack data. At an  $\alpha$  of  $0^\circ$ , the aerothermodynamic data clearly indicated that the shock-interference pattern for the highly swept delta-wing was a Type VI, as was expected. At angles-of-attack of  $30^\circ$  to  $50^\circ$ , the aerothermodynamic data from the shock:shock interaction region retain the characteristics of the Type V pattern for the low-sweep straight-wing configurations and of the Type VI pattern for the high-sweep delta-wing configurations. However, the data indicate the flow field is very sensitive to the geometry of the wing-root fairing. The sensitivity of the flow field to the wing-root geometry is evident in the heat-transfer measurements and the flow-field photographs. For example, the irregular heat-transfer distribution due to the "gradual" compression of the rotational flow in the wing-root region of the NAR 161B differs markedly from the "classical" distribution, e.g., Bushnell (ref. 9). Furthermore, the flow-field of the NAR delta-wing orbiters, whose planforms have a large radius fairing of the wing leading-edge into the fuselage, exhibited two unique trends (counter to those observed for the other delta-wing configurations considered):

- (1) the shock:shock interaction "location" moved outboard as  $\alpha$  increased, and
- (2) no chordwise regions of locally high heating were observed in the wing-root region.

While the photographic trace of the bow-generated shock wave was affected by nose bluntness, the interaction between the fuselage-generated shock wave and the wing-generated shock wave depends primarily on the local geometry, i.e., that in the vicinity of the wing. The "type" of shock-interference pattern appeared to be dominated by the leading-edge sweep. However, the spanwise location of the shock:shock interaction and the severity of the heat-transfer perturbation was affected by the curvature of the windward fuselage, the wing offset, and the wing dihedral.

The maximum perturbation in heat transfer observed in the data presented herein was a factor of 3 for a straight-wing configuration, which would be the result of a "Type V" shock-interference pattern. Two possible reasons of this relatively low interference factor are: (1) insufficient instrumentation density (the rapid variation of surface pressure and of heat transfer in the perturbed region is clearly evident in the results of Keyes and Hains (ref. 39) or (2) the "relief" provided by the three-dimensional character of the expanding flow over the wing. Although the flow field for the wing is complex, the highest heat-transfer rates are confined to regions between 0% and 25% chord.

There were not sufficient data to establish the effect of Reynolds number. However, the heat-transfer due to shock-wave:boundary-layer interactions, interactions between jets and the boundary layer, and impingement of shear layers would be expected to be dependent on the boundary-layer character (ref. 40). For the hypersonic flows considered, there appeared to be no significant effect of Mach number. However, these data were obtained in facilities where

$\gamma$  was approximately 1.4, regardless of the Mach number. When applying these data to hypersonic flight, the real-gas effects are the important phenomena associated with the Mach number variation. Calculations of the pressure amplification for a Type IV interaction (ref. 41) were found to be very sensitive to  $\gamma$ , with a maximum pressure amplification in excess of 60 for  $\gamma = 1.2$  compared to an amplification of 18 for  $\gamma = 1.4$ . In a subsequent study (ref. 39), heat-transfer tests were not possible and pressure tests were limited because of problems encountered in the wind tunnel using tetrafluoromethane as the test gas. Calculations made in this same study indicated that the perturbation for the Type IV interference pattern would increase markedly as  $\gamma$  decreases. The heating perturbation for the Type V pattern increases somewhat as  $\gamma$  decreases. Because the Type VI interference pattern produced an expansion-fan:boundary-layer interaction, the calculations of ref. 39 were limited to the pressure reduction (which was slightly less for  $\gamma = 1.2$  than for  $\gamma = 1.4$ ). Recall from the "Introduction" that Hunt and Creel (ref. 18) concluded that, because the delta-wing configuration "reenters at lower angles of attack and is essentially free of imbedded shock, real-gas shock-density-ratio effects will be less significant" than, those for the straight-winged orbiter.

## CONCLUSIONS

Based on the data and analyses presented herein, the following conclusions are made for the configurations and test conditions of this program.

1. Configuration geometry - The "type" of shock-interaction pattern is dominated by leading-edge sweep (although inboard of the shock: shock intersections, the flow-field is sensitive to the angle-of-attack). The interaction between the fuselage-generated shock wave and the wing-generated shock wave depends primarily on the local model geometry, i.e., that in the vicinity of the wing. The wing-root fairing has a marked effect on the heat-transfer rates over an extensive surface area.
2. Reynolds number - There were not sufficient data to establish the effect of Reynolds number other than as it relates to transition.
3. Mach number - For the hypersonic flows considered (for which  $\gamma$  was approximately 1.4, regardless of the Mach number), there appeared to be no significant effect of Mach number.
4. Heat-transfer perturbation - The maximum perturbation in heat transfer was only a factor of 3 which was observed for straight-wing configurations.



## REFERENCES

1. B. M. Ryan: "Summary of the Aerothermodynamic Interference Literature", Technical Note 4061-160, April 1969, Naval Weapons Center.
2. R. H. Korkegi: "Survey of Viscous Interactions Associated with High Mach Number Flight", AIAA Journal, Vol. 9, No. 5, May 1971, pp. 771-783.
3. C. E. Gulbran, E. Redeker, D. S. Miller, and S. L. Strack: "Heating in Regions of Interfering Flow Fields, Part II: Leading Edge Shock Impingement", Technical Report AFFDL-TR-65-49, Part II, January 1967, The Boeing Company.
4. B. Edney: "Anomalous Heat Transfer and Pressure Distributions on Blunt Bodies at Hypersonic Speeds in the Presence of an Impinging Shock", Report 115, 1968, Flygtekniska Försöksanstalten (The Aeronautical Research Institute of Sweden).
5. R. S. Hiers and W. J. Loubsky: "Effects on Shock-Wave Impingement on the Heat Transfer on a Cylindrical Leading Edge" TN D-3859, February 1967, NASA.
6. E. C. Knox: "Measurements of Shock-Impingement Effects on the Heat-Transfer and Pressure Distributions on a Hemicylinder Model at Mach Number 19", TR-65-245, November 1965, AEDC.
7. F. D. Hains and J. W. Keyes: "Shock Interference Heating in Hypersonic Flows", AIAA Paper 72-78, presented at the AIAA 10th Aerospace Sciences Meeting at San Diego, California, January 1972.
8. J. J. Bertin, F. E. Williams, R. C. Baker, W. D. Goodrich, and W. C. Kessler, "Aerothermodynamic Measurements for Space Shuttle Configuration in Hypersonic Wind Tunnels", Space Shuttle Aerothermodynamics Technology Conference, Volume II - Heating, TM X-2507, February 1972, NASA.
9. D. M. Bushnell: "Interference Heating on a Swept Cylinder in Region of Intersection with a Wedge at Mach Number of 8", TN D-3094, December 1965, NASA.
10. I. E. Beckwith and J. J. Gallagher: "Local Heat Transfer and Recovery Temperature on a Yawed Cylinder at a Mach Number of 4.15 and High Reynolds Number", TR R-104, 1961, NASA.
11. G. C. Lorenz, P. J. Sartell, and S. L. Strack: "Experimental Investigation of Heat Transfer to Complex Aerodynamic Configurations at Hypersonic Speeds", ASD-TDR-63-530, September 1963, The Boeing Company.
12. R. A. Jones, D. M. Bushnell, and J. L. Hunt: "Experimental Flow Field and Heat Transfer Investigation of Several Tension Shell Configuration at a Mach Number of 8", TN D-3800, January 1967, NASA.

55

13. J. G. Marvin, W. K. Lockman, G. G. Mateer, H. L. Seegmiller, C. C. Pappas, C. DeRose, and G. E. Kaattari: "Flow Fields and Aerodynamic Heating of Space Shuttle Orbiters", NASA Space Shuttle Technology Conference, Volume I - Aerothermodynamics, Configurations, and Flight Mechanics, TM X-2272, April 1971, NASA.
14. H. L. Seegmiller: "Shock Interference Heating and Density Ratio Effects, Part I - Flow Field Visualization, Thermocouple Measurements, and Analysis", NASA Space Shuttle Technology Conference, Volume I - Aerothermodynamics, Configurations, and Flight Mechanics, TM X-2272, April 1971, NASA.
15. C. E. Rogers: "Experimental Investigation of Leading-Edge Shock Impingement and Interaction Heating on a 1/80 Scale Model of a NASA Straight Wing Orbiter Configuration at Mach Numbers of 8 and 16", CAL Report No. AA-2977-Y-1, August 1971, Cornell Aeronautical Laboratory.
16. W. C. Kessler, J. R. Reilly, and E. Sampatacos: "Hypersonic Shock Wave Interaction and Impingement", MDC E0476, October 1971, McDonnell Douglas Astronautics Company-East.
17. J. J. Bertin, F. E. Williams, R. C. Baker, C. L. Smith, and T. C. Pope: "Aerothermodynamic Measurements for Space-Shuttle Configurations in Hypersonic Wind Tunnels", Aerospace Engineering Report 71006, September 1971, University of Texas at Austin.
18. J. L. Hunt and T. R. Creel, Jr.: "Shock Interference Heating and Density Ratio Effects, Part II - Hypersonic Density Ratio Effects", NASA Space Shuttle Technology Conference, Volume I - Aerothermodynamics, Configurations, and Flight Mechanics, TM X-2272, April 1971, NASA.
19. A. R. Mendelsohn, M. Bourbin, M. Jew, and C. W. Osonitsch: "A Review of the Grumman Orbiter Wind Tunnel Heat Transfer Tests", Space Shuttle Aerothermodynamics Technology Conference, Volume II - Heating, TM X-2507, February 1972, NASA.
20. R. O. Doughty, R. C. Erickson, O. R. Brock, T. W. Moore, and J. V. Clifton: "Convective Heating on Delta-Wing Space-Shuttle Boosters Including Interference Effects", AIAA Paper 72-315, presented at the AIAA 7th Thermophysics Conference at San Antonio, April 1972.
21. J. D. Warmbrod, W. R. Martindale, and R. K. Mathews: "Heat Transfer Rate Measurements on North American Rockwell Orbiter (161B) at Nominal Mach Number of 8", DMS-DR-1177, Volume III, December 1971, Arnold Engineering Development Center.
22. J. J. Bertin, J. P. Lamb, K. R. Center and B. W. Graumann: "Flow Field Measurements for Cylindrical Configurations in a Hypersonic Wind Tunnel: Windward and Leeward Flow Fields", Aerospace Engineering Report 71007, December 1971, University of Texas at Austin.

23. J. J. Bertin, J. P. Lamb, J. L. Zickler, and W. D. Goodrich: "Flow Field Measurements for Space-Shuttle-Related Cylindrical Configurations in Hypersonic Streams", AIAA Paper 72-294, presented at the AIAA 7th Thermophysics Conference at San Antonio, April 1972.
24. I. H. Abbott and A. E. von Doenhoff: Theory of Wing Sections, Dover Publications, New York, 1959.
25. W. K. Lockman and C. E. DeRose: "Aerodynamic Heating Distributions on a Space Shuttle Delta-Wing Orbiter", TM X-62,114, March 1972, NASA.
26. J. A. Fay and F. R. Riddell: "Theory of Stagnation Point Heat Transfer in Dissociated Air", Journal of the Aeronautical Sciences, Vol. 25, No. 2, February 1958, pp. 73-85, 121.
27. J. C. Boison and H. A. Curtiss: "An Experimental Investigation of Blunt Body Stagnation Point Velocity Gradient", ARS Journal, Vol. 29, No. 2, February 1959, pp. 130-135.
28. M. H. Betram, W. V. Feller, and J. C. Dunavant: "Flow Fields, Pressure Distributions, and Heat Transfer for Delta Wings at Hypersonic Speeds", TM X-316, September 1960, NASA.
29. C. H. Young, D. H. Reda, and A. M. Roberge: "Hypersonic Flow Field and Heat Transfer Studies on a Lifting Entry Vehicle at Angles of Attack from 0° to 60°, GDC-ERR-1418, September 1970, General Dynamics, Convair Division.
30. J. W. Cleary: "Experimental Surface Flow Patterns and Flow-Field Phenomena of a Delta-Wing Space-Shuttle Orbiter", TM X-62,113, February 1972, NASA.
31. O. Brevig, R. L. Otwell, and R. C. Day, Jr.: "Aerodynamic Heat Transfer Distribution on Phase B Space Shuttle Booster Vehicles at Angles of Attack from -5° to 60°", 584-TP-342, March 1971, General Dynamics, Convair Division.
32. R. C. Baker, K. W. McGee, and H. D. Schultz: "Heat Transfer Distributions on the LMSC 040C and 040A-L4 Delta Wing Orbiters", LMSC-D157394, May 1972, Lockheed Missiles and Space Company.
33. R. K. Matthews, W. R. Martindale, and J. D. Warmbrod: "Heat Transfer Rate Distribution on North American Rockwell Delta Wing Orbiter Determined by Phase Change Paint Technique at a Mach Number of 8", DMS-DR-1231, Volume I, March 1972, Arnold Engineering Development Center. (NASA CR 120,048)
34. Ames Research Staff: "Equations, Table, and Charts for Compressible Flow", Report 1135, 1953, NACA.
35. J. W. Cleary: "Pitot-Pressure Distributions of the Flow Field of a Delta-Wing Orbiter", TM X-62,122, May 1972, NASA.
36. M. V. Morkovin: "Critical Evaluation of Transition from Laminar to Turbulent Shear Layers with Emphasis on Hypersonically Traveling Bodies", AFFDL-TR-68-149, March 1969, Air Force Flight Dynamics Laboratory.

37. A. Henderson, J. C. Dunavant, and R. A. Jones: "Heating Studies on Manned Space Shuttle Concepts", presented at the ASME Space Technology and Heat Transfer Conference, June 1970, Los Angeles, California.
38. C. A. Scottoline, J. W. Haney, and M. H. Harthun: "An Experimental Investigation of the Aerodynamic Heating Characteristics of a Swept Wing Space Shuttle Orbiter at  $M = 8$ ", SD 70-13, June 1970, Space Division, North American Rockwell.
39. J. W. Keyes and F. D. Hains: "A Study of Shock Interference Heating in Hypersonic Flows", proposed NASA TN, February 1972.
40. C. F. Markarian: "Heat Transfer in Shock Wave-Boundary Layer Interaction Regions", NWC TP 4485, November 1968, Naval Weapons Center.
41. B. E. Edney, T. T. Bramlette, J. Ives, F. D. Hains, and J. W. Keyes: "Theoretical and Experimental Studies of Shock Interference Heating", Report No. 9500-920-195, October 1970, Bell Aerospace Company.

Table 1. - Run schedule of nominal test conditions

Configuration	$\alpha$	Nominal test condition <sup>†</sup>				
		Martin HWT	VAC HVWT			
		Cond 1	Cond 2	Cond 3	Cond 4	Cond 5
F2:W2	40°	2625*	—	—	—	—
	50°	2625*	—	—	—	—
	60°	2621*	—	—	—	—
F3:W2	30°	—	1011	1010	—	—
	40°	2627*	—	—	35*	—
	50°	2622*	1012	—	36*	—
	60°	2620*	—	—	37*	—
F3:W3	40°	—	1006	1007	38,39*	—
	50°	—	1005	1009	40*	—
	60°	—	—	—	41*	—
F3:W4	20°	—	1019	1020	—	—
	30°	—	1013	1024	—	—
	40°	2656*	1018	1027	—	—
	50°	2658*	1014	1025	—	—
	60°	2660*	1017	1028	—	—
F4:W1	40°	2629*	—	—	—	—
	44°	2631*	—	—	—	—
	50°	2635*	—	—	—	—
	60°	2637*	—	—	—	—
F4:W2	30°	—	1002	1004	—	—
	40°	2640*	—	—	26,25*	34*
	50°	2639*	1003	—	24,27,29*	31*
	60°	2636*	—	—	21,22,23*	33,32*
F4:W3	40°	2642*	—	—	—	—
	50°	2645*	—	—	—	—
	60°	2638*	—	—	—	—

<sup>†</sup>The nominal test conditions are:

	$M_\infty$	$Re_\infty/\text{ft}$	Tunnel
Cond 1	14	$0.7 \times 10^6$	Martin HWT
Cond 2	10	$2.0 \times 10^6$	VAC HVWT
Cond 3	10	$13.0 \times 10^6$	VAC HVWT
Cond 4	12	$4.0 \times 10^6$	VAC HVWT
Cond 5	17	$2.0 \times 10^6$	VAC HVWT

\*The data from these runs have been discussed previously, ref. 17.

Table 2. - Run schedule  
(a) VAC Hypervelocity Wind Tunnel

Run No.	Conf	$\alpha$	$M_\infty$	$Re_\infty / ft$ $\times 10^{-6}$	$P_{t2}$ (psia)	$T_t$ (°R)
1011	F3:W2	30	10.31	2.3538	15.4113	3660
1012	F3:W2	50	10.29	2.2080	14.7986	3700
1010	F3:W2	30	10.97	16.6716	38.6678	2175
1006	F3:W3	40	10.63	2.7608	14.5818	3340
1005	F3:W3	50	10.17	2.2615	14.8303	3600
1007	F3:W3	40	9.27	9.6830	40.4940	2520
1009	F3:W3	50	10.03	14.6508	38.3869	2100
1019	F3:W4	20	10.94	2.5661	14.4732	3600
1013	F3:W4	30	10.61	2.5853	16.1724	3675
1018	F3:W4	40	10.56	2.7125	16.5701	3600
1014	F3:W4	50	10.60	2.8623	17.9352	3685
1017	F3:W4	60	10.20	2.1983	15.2348	3740
1020	F3:W4	20	9.82	13.9949	40.3570	2160
1024	F3:W4	30	9.94	13.9862	34.5859	2000
1027	F3:W4	40	10.09	13.5212	40.5318	2285
1025	F3:W4	50	9.93	13.2971	38.6967	2200
1028	F3:W4	60	9.91	14.0723	38.8564	2115
1002	F4:W2	30	10.80	2.8725	15.0967	3395
1003	F4:W2	50	10.32	2.2138	14.3079	3630
1004	F4:W2	30	9.83	12.7003	40.9189	2300

Table 2. - Concluded

(b) NAR 161B DWO tests in AEDC Tunnel B

<u>Run No.</u>	<u><math>\alpha</math></u>	<u><math>M_\infty</math></u>	<u><math>Re_\infty/ft</math> (<math>\times 10^{-6}</math>)</u>	<u><math>P_{t2}</math> (psia)</u>	<u><math>T_t</math> (°R)</u>
96	30°	8.00	3.74	7.273	1341
98	50°	8.00	3.73	7.289	1346
99	50°	8.00	2.50	4.687	1310
101	30°	8.00	2.50	4.697	1311
103	10°	8.00	2.52	4.718	1307
104	10°	7.94	0.790	1.419	1261
106	30°	7.94	0.839	1.456	1232
108	0°	7.94	0.841	1.459	1233
111	0°	8.00	3.81	7.278	1325
113	10°	8.00	3.73	7.259	1343

Table 3. - Intersection of the fuselage-generated shock wave with the wing-generated shock wave in the vicinity of the wing leading-edge for an alpha of 30°.

Ref	$\Lambda$ ; Model	$\frac{z_a}{0.5W_b}$	Comments
present	15°; F3:W2 (straight-wing orbiter)	1.81 (0.27*)	Intersection just ahead of wing leading-edge using schlieren
13	22°; NAR straight-wing orbiter	2.00 (0.25*)	Peak-heating location at 0% (and at 10%) chord determined using thermocouple measurements
32	50°; 040C (delta-wing orbiter)	2.00 (0.30*)	Present authors' interpretation of paint data of ref. 32
32	50°; 040A-L4 (delta-wing orbiter)	1.92 (0.31*)	Present authors' interpretation of paint data of ref. 32
31	53°; delta-wing booster	2.05 (0.31*)	Peak-heating location at 10% chord determined using paint data
present	60°; F3:W4 (delta-wing orbiter)	2.02 (0.51*)	Intersection just ahead of wing leading-edge using schlieren
30	60°; NAR 134 (delta-wing orbiter)	1.68 (0.42*)	Intersection just ahead of wing leading-edge using shadowgraph
present	60°; NAR 161B (delta-wing orbiter)	1.95 (0.55*)	Heat-transfer distribution obtained using thermocouples along the leading-edge

\*coordinate given in parenthesis is  $\frac{z_r}{b}$



Table 4. - Intersection of the fuselage-generated shock wave with the wing-generated shock wave in the vicinity of the wing leading-edge for an alpha of 50°

Ref	$\Lambda$ ; Model	$\frac{z_a}{0.5W_b}$	Comments
present	15°; F3:W2 (straight-wing orbiter)	1.66 (0.22*)	Intersection just ahead of wing leading-edge using schlieren
16	15°; F3:W2 (straight-wing orbiter)	1.63 (0.21*)	Schlieren photographs
present†	15°; F4:W2 (straight-wing orbiter)	1.78 (0.26*)	Intersection just ahead of wing leading-edge using schlieren
16††	15°; F4:W2 (straight-wing orbiter)	1.93 (0.31*)	Schlieren photographs
present†††	15°; F4:W2 (straight-wing orbiter)	1.96 (0.32*)	Burn pattern on surface of wing in post-test photograph
present	30°; F3:W3 (straight-wing orbiter)	1.72 (0.24*)	Intersection just ahead of wing leading-edge using schlieren
32	50°; 040C (delta-wing orbiter)	No Interaction	Present authors' interpretation of paint data
31	53°; delta-wing booster	1.93 (0.25*)	Present authors' interpretation of paint data
30	60°; NAR 134 (delta-wing orbiter)	2.32 (0.52*)	Present authors' interpretation of the shadowgraph for $\alpha = 45^\circ$
present	60°; NAR 161B (delta-wing orbiter)	1.85 (0.50*)	Heat transfer distribution obtained using thermocouples along the leading-edge.
present	60°; F3:W4	---	The location of an intersection was difficult to define

\*coordinate given in parenthesis is  $\frac{z_r}{b}$

†Data were obtained in the VAC HWWT

††Data were obtained in the Martin Marietta Hotshot Tunnel

Table 5. - Pressure measurements for the delta wing

Nondimensionalized pressure data, $\frac{p}{p_{t2}}$									
$\alpha$	Nominal flow cond	$z_r=0.02b$ $s_w=0.125c_\ell$	$z_r=0.2b$ $s_w=0.250c_\ell$	$z_r=0.2b$ $s_w=0.750c_\ell$	$z_r=0.4b$ $s_w=0.250c_\ell$	$z_r=0.6b$ $s_w=0.250c_\ell$	$z_r=0.8b$ $s_w=0.250c_\ell$	$z_r=0.8b$ $s_w=0.750c_\ell$	Mod Newt
20°	2	.170	.163	.138	.126	.146	.159	.109	.122
	3	.207	.206	.145	.155	.180	.243	.142	
30°	2	.320	.321	.259	.315	.313	.400	.169	.254
	3	.460	.502	.421	.478	.449	—	.441	
40°	2	.434	.457	.417	.463	.439	.543	.394	.415
	3	.507	.599	.579	.482	.269	—	.573	
50°	2	.607	.607	.547	.611	.608	.728	—	.588
	3	.380	.817	.799	.814	—	—	.720	
60°	2	.768	.745	.720	.730	.699	.816	—	.751
	3	.612	.715	.940	.521	.337	—	.762	

Table 6. - Heat-transfer data from the wing thermocouples  
of the VAC DWO, i.e., F3;W4

(a) Nominal flow condition 2;  $M_\infty = 10$ ,  $Re_\infty/ft = 2 \times 10^6$

tc	$\frac{s_w}{c_l}$	$\frac{z_r}{b}$	$\dot{q}$ , Btu/ft <sup>2</sup> sec				
			$\alpha = 20^\circ$	$\alpha = 30^\circ$	$\alpha = 40^\circ$	$\alpha = 50^\circ$	$\alpha = 60^\circ$
11	0.0	.2	107.3	123.5	113.4	105.9	71.2
13	0.25	.2	26.0	49.3	44.1	43.3	59.2
14	0.50	.2	92.3	37.0	32.9	34.8	32.1
15	0.75	.2	88.4	32.1	31.0	35.8	32.3
16	0.0	.4	116.9	146.9	137.9	130.2	82.8
17	0.125	.4	48.1	71.1	88.1	83.1	76.8
18	0.25	.4	24.9	34.5	41.9	44.3	42.3
20	0.75	.4	18.5	26.7	28.0	34.4	32.2
21	0.0	.6	83.3	110.3	111.0	98.6	62.5
22	0.125	.6	40.7	61.0	76.8	84.6	72.6
23	0.25	.6	20.4	32.8	47.5	53.4	49.6
24	0.50	.6	9.5	27.0	33.1	37.7	36.1
25	0.75	.6	9.5	22.1	29.9	32.8	34.6
26	0.125	.8	36.9	—	67.7	—	66.5
27	0.25	.8	29.8	48.1	58.0	66.5	62.5
29	0.75	.8	24.9	30.9	38.7	44.8	43.5
$\dot{q}_{t,R=1 \text{ ft}}$ (Btu/ft <sup>2</sup> sec)			623.3	670.8	666.9	708.0	660.3

Table 6. - Concluded

(b) Nominal flow condition 3;  $M_\infty = 10$ ,  $Re_\infty/ft = 13 \times 10^6$

<u>tc</u>	$\frac{s_w}{c_l}$	$\frac{z_r}{b}$	$\dot{q}$ , Btu/ft <sup>2</sup> sec				
			$\alpha = 20^\circ$	$\alpha = 30^\circ$	$\alpha = 40^\circ$	$\alpha = 50^\circ$	$\alpha = 60^\circ$
11	0.0	.2	85.1	82.0	—	89.9	—
13	0.25	.2	44.1	78.2	112.1	89.7	84.8
14	0.50	.2	32.6	61.8	74.4	67.3	61.7
15	0.75	.2	24.4	48.4	66.8	65.5	58.9
16	0.0	.4	115.9	163.0	149.9	94.9	59.8
17	0.125	.4	85.5	—	—	—	91.0
18	0.25	.4	36.5	56.9	141.0	73.9	65.0
20	0.75	.4	28.1	52.6	89.5	64.8	—
21	0.0	.6	83.2	106.5	120.2	74.9	44.5
22	0.125	.6	56.5	99.0	134.6	107.7	83.3
23	0.25	.6	38.2	66.1	108.6	87.7	75.4
24	0.50	.6	32.5	65.7	83.5	72.9	60.4
25	0.75	.6	28.7	37.3	90.1	74.6	55.9
26	0.125	.8	50.6	82.4	125.4	99.7	75.3
27	0.25	.8	46.9	75.0	125.4	95.1	76.0
29	0.75	.8	66.4	76.7	113.7	108.3	67.7
$\dot{q}_{t,R=1 \text{ ft}}$ (Btu/ft <sup>2</sup> sec)			520.9	425.0	571.1	525.4	493.9

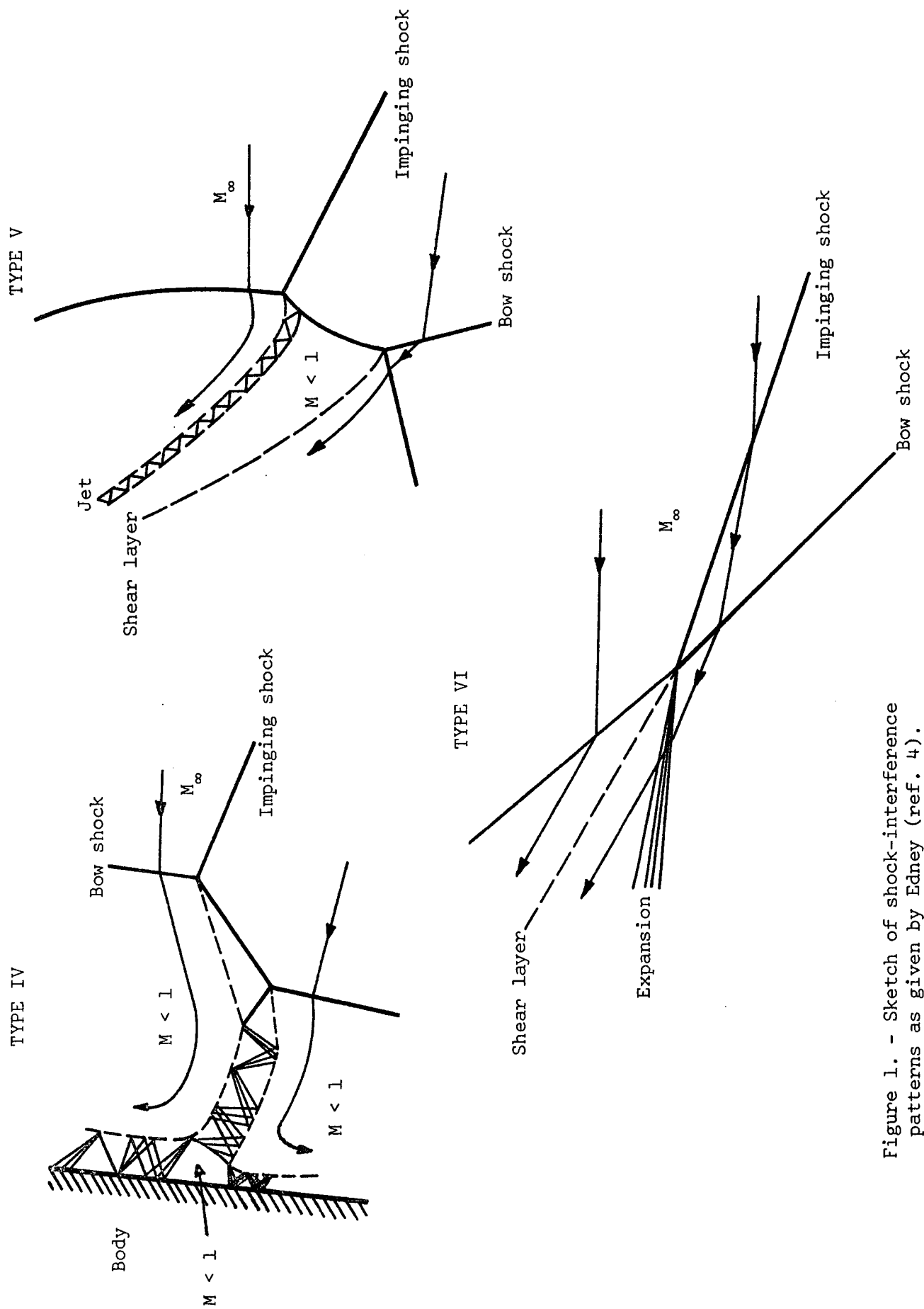
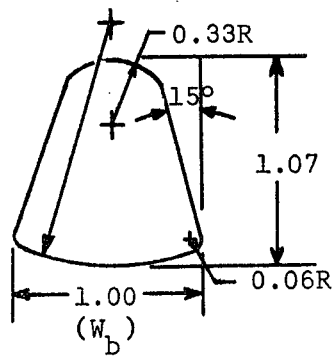
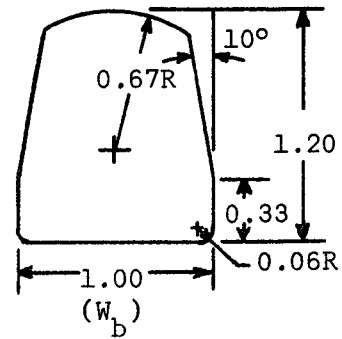


Figure 1. - Sketch of shock-interference patterns as given by Edney (ref. 4).

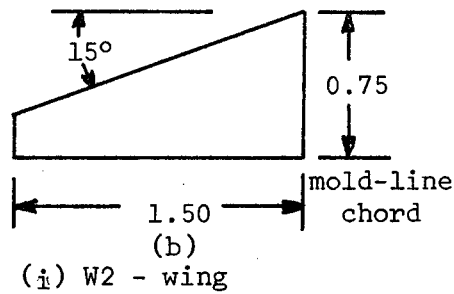


(i) F4 - fuselage

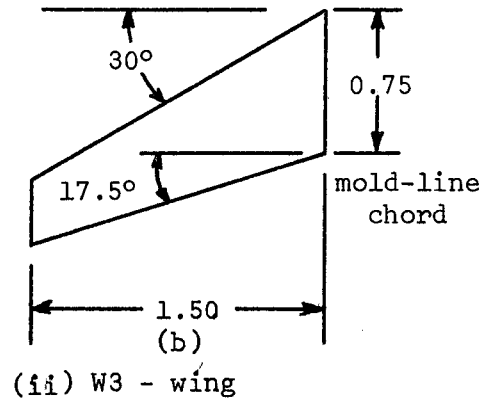


(ii) F3 - fuselage

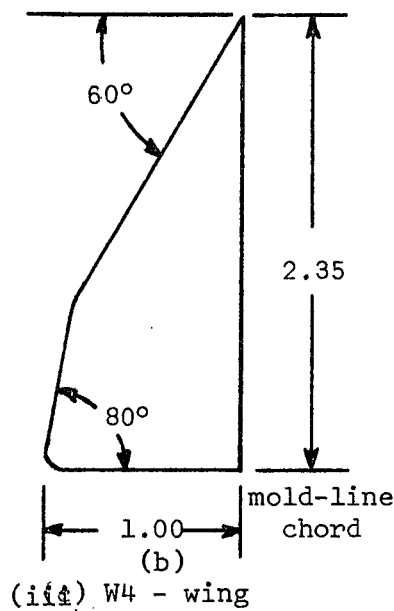
(a) Fuselage cross-sections



(i) W2 - wing



(ii) W3 - wing

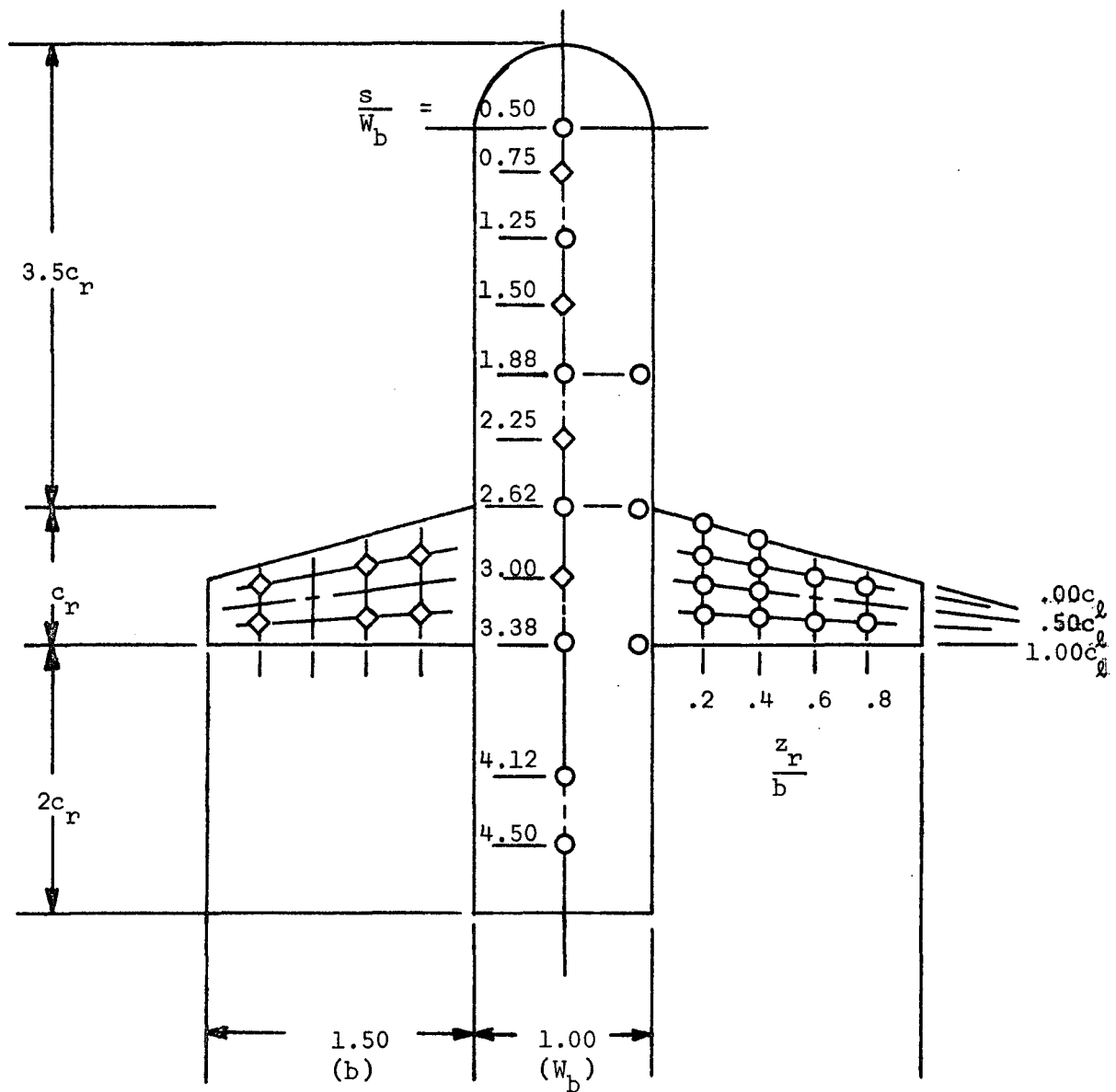


(iii) W4 - wing

(b) Wing planforms

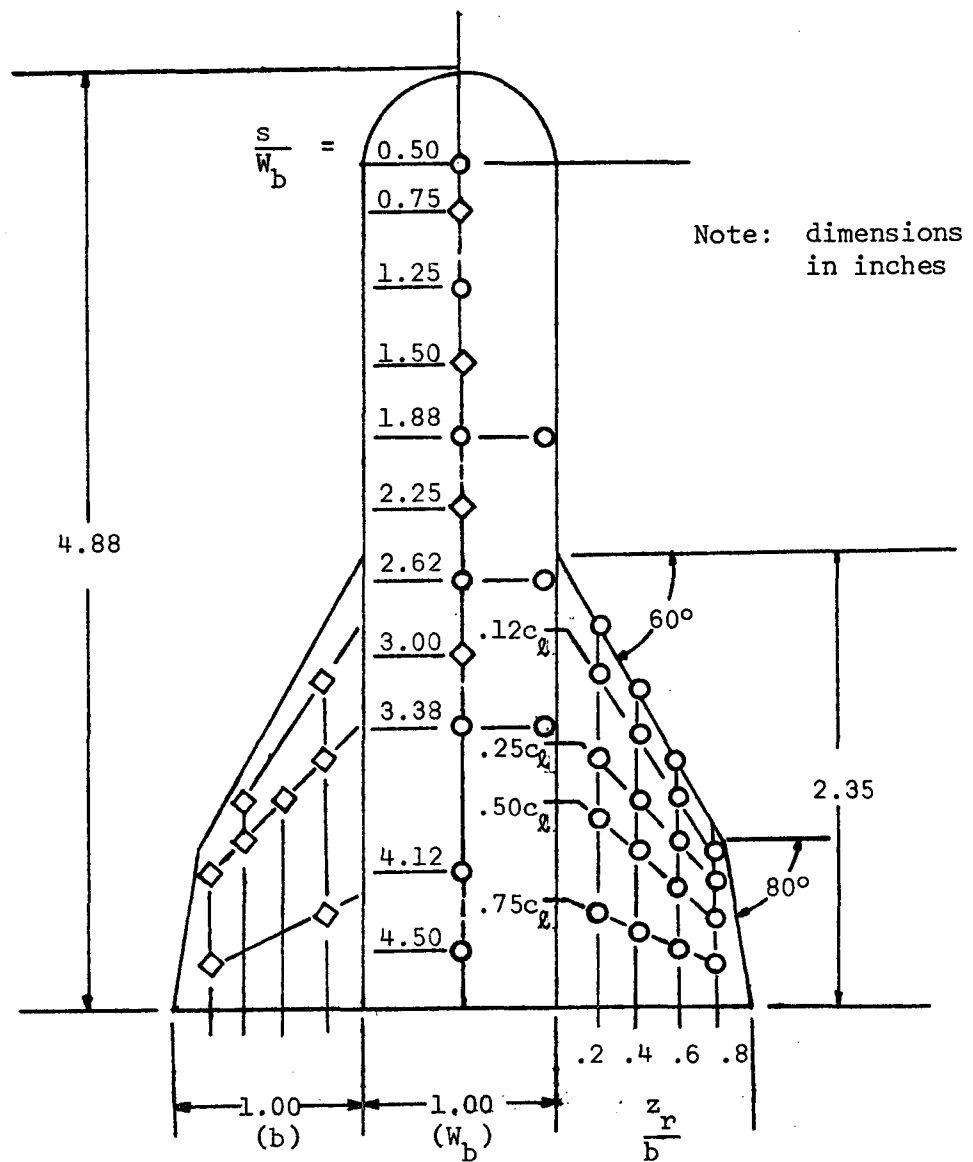
Note: All dimensions in inches

Figure 2. - Component details for VAC HVWT models.



(a) Sketch of straight-wing model

Figure 3. - Instrumentation locations for the space shuttle models used in the VAC HVWT.

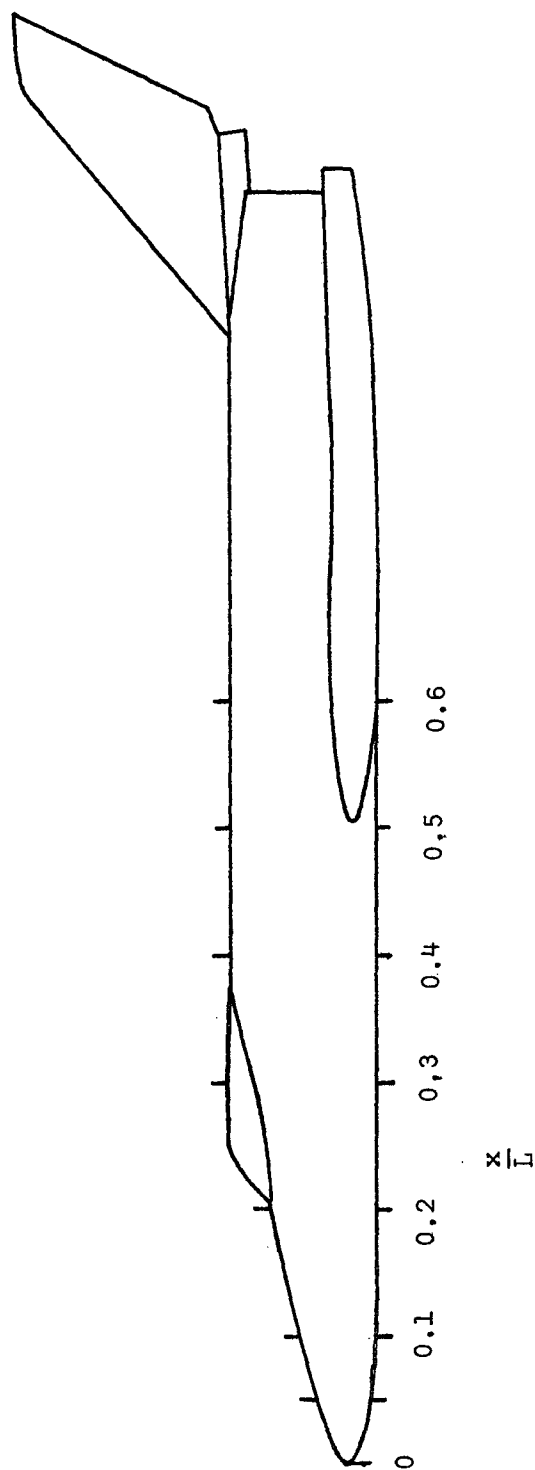


- Thermocouples
- ◇ Pressure orifices

(b) Sketch of delta-wing model

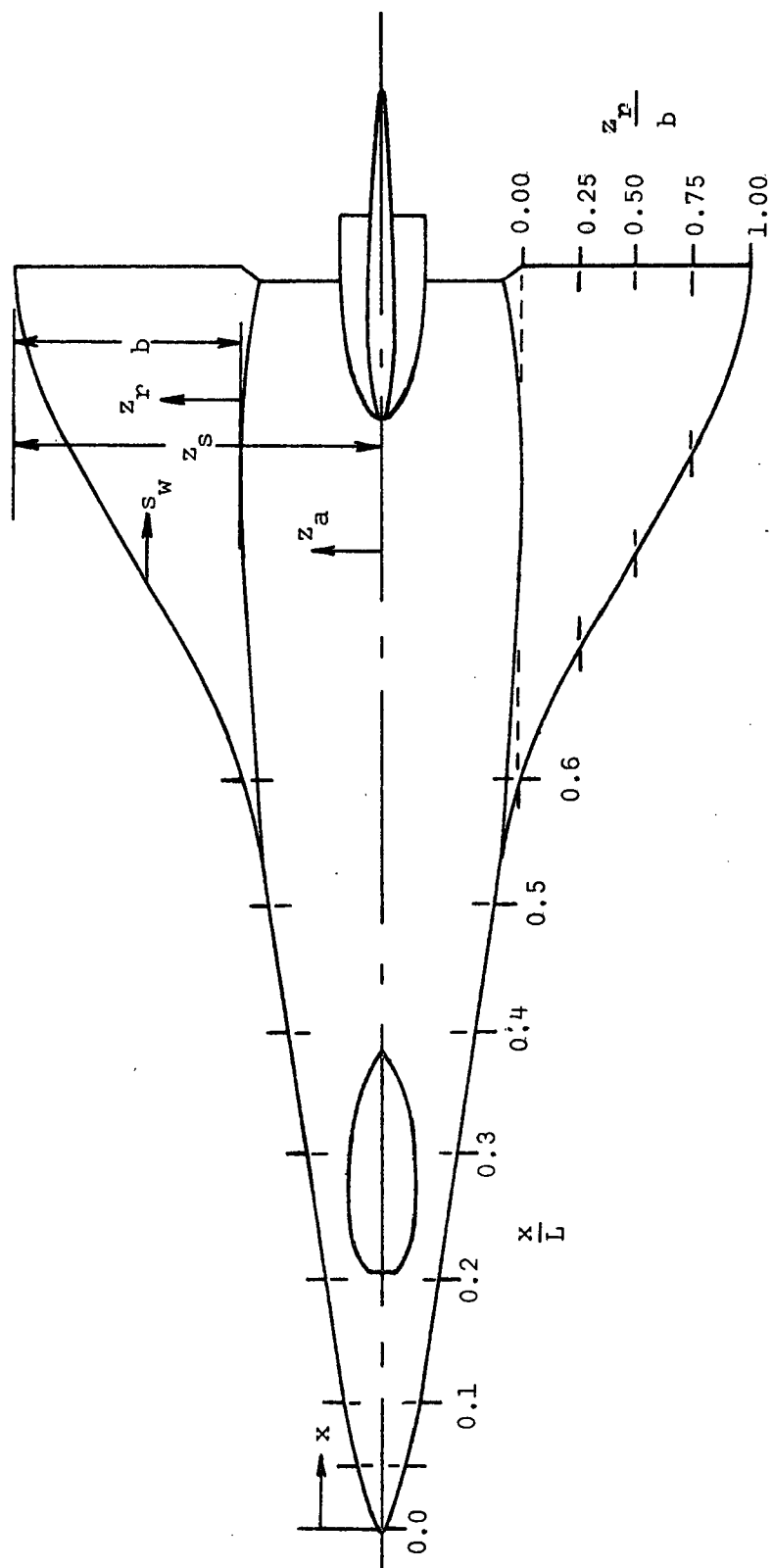
Figure 3. - Concluded





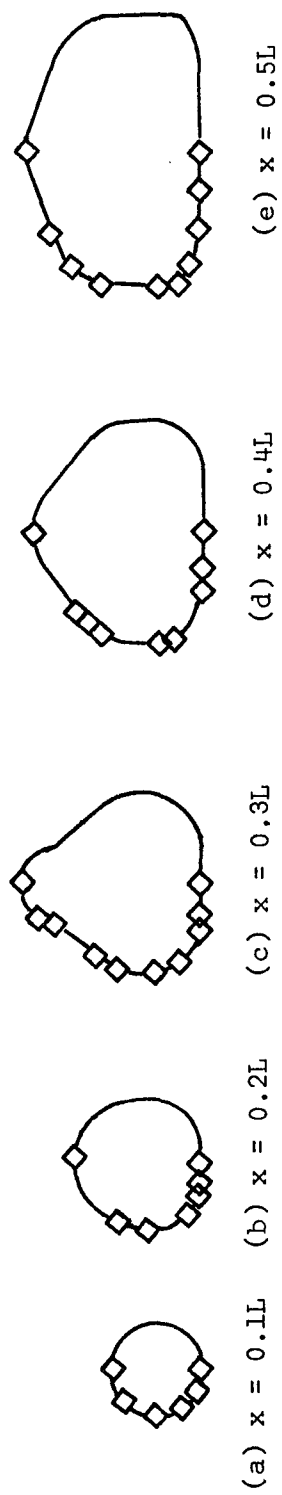
(a) Side View

Figure #. ~ Sketch of the NAR 161B DW0

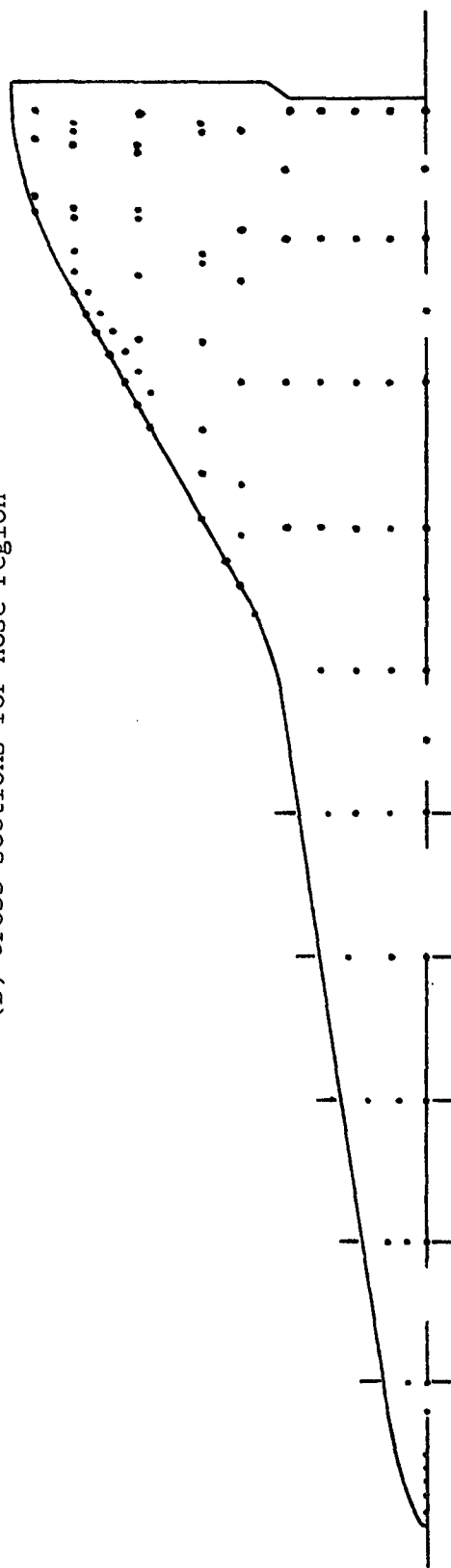


(b) Plan view

Figure 4. - Concluded



(b) Cross-sections for nose region



(a) Bottom view

Figure 5. - Sketch of thermocouple locations for NAR 161B DWO.



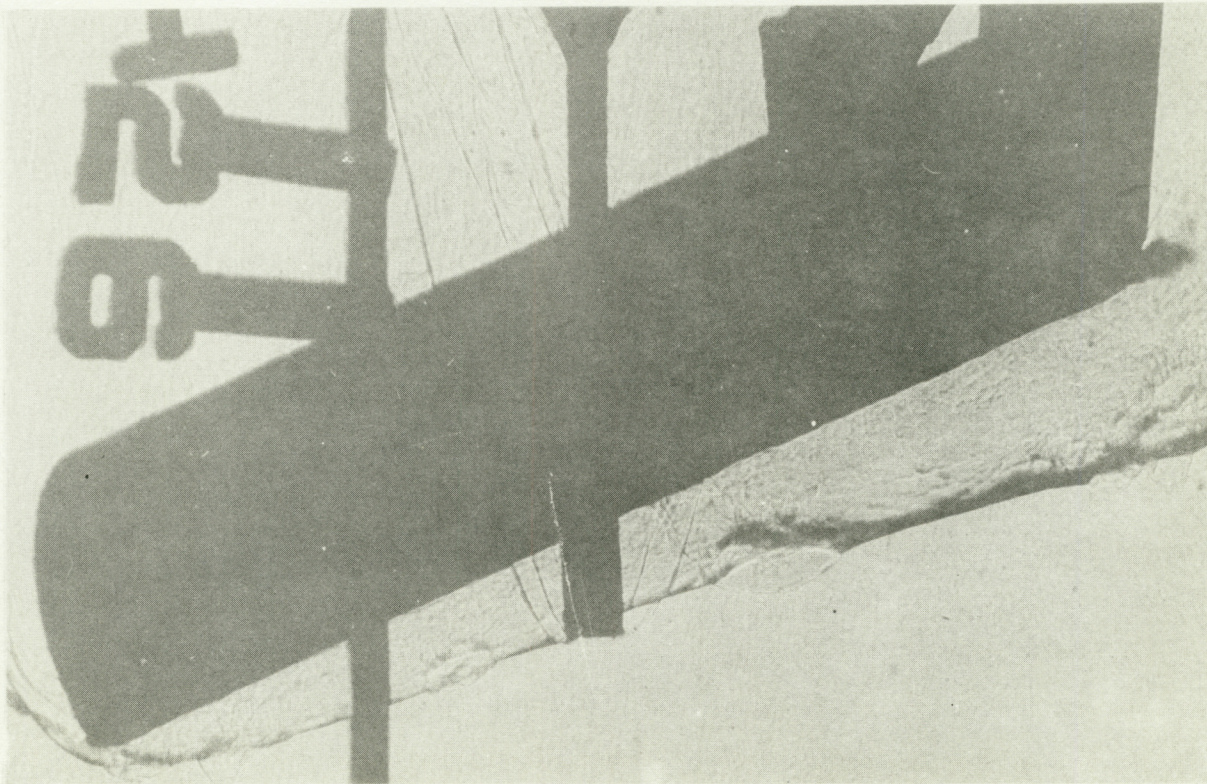


Figure 6. - Flow-field photographs for the VAC DWO at an  
alpha of  $60^\circ$ , nominal flow condition 3.



---calculated pressure for modified Newtonian flow

◇ pressure data or orifice location

○ heat transfer data, or thermocouple location

◇ ○ F4:W2,  $M_\infty = 12.0$ ,  $Re_\infty/ft = 4.0 \times 10^6$

◆ ● F4:W2,  $M_\infty = 17.0$ ,  $Re_\infty/ft = 2.0 \times 10^6$

◆ ● F4:W2,  $M_\infty = 10.3$ ,  $Re_\infty/ft = 2.2 \times 10^6$

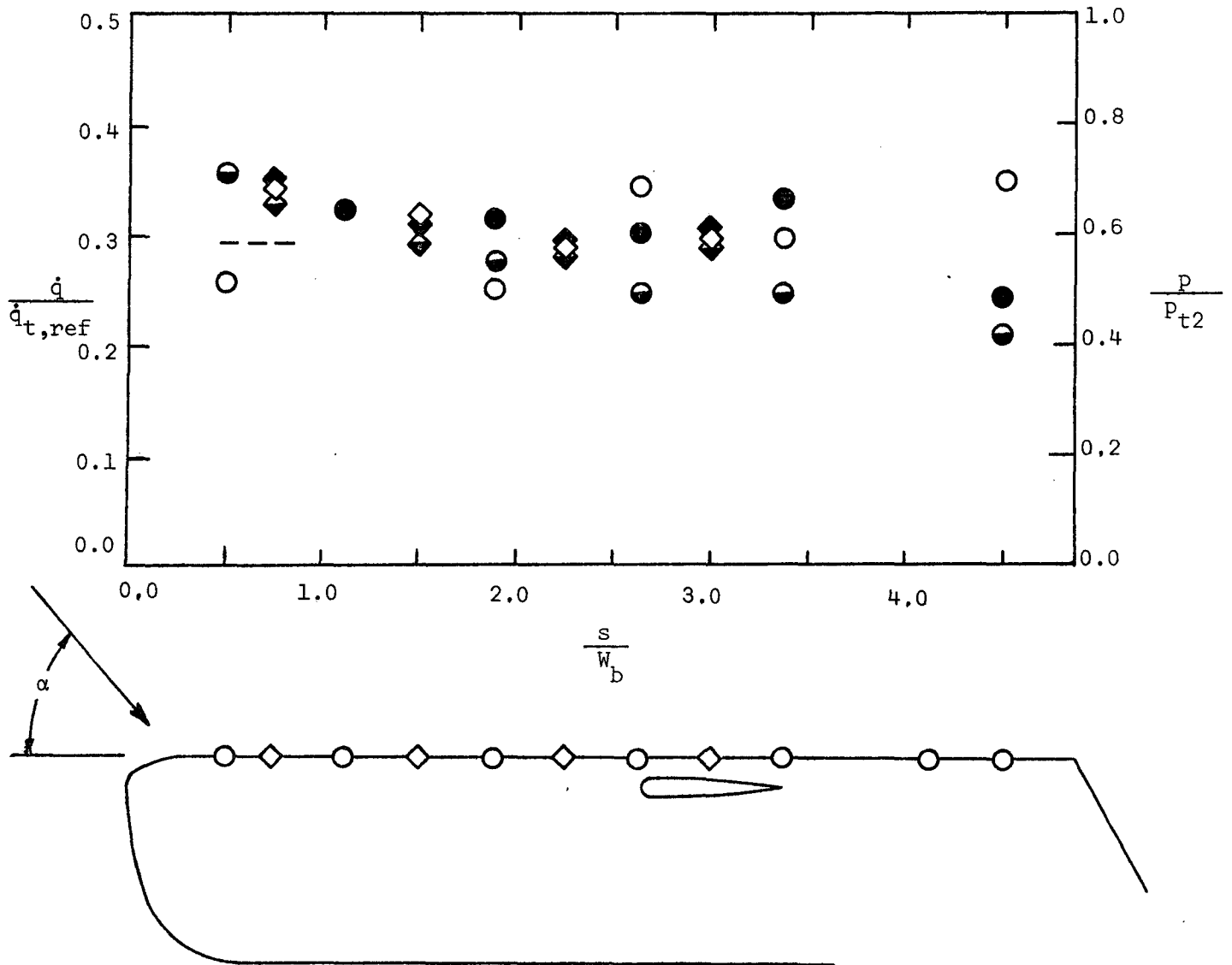


Figure 7. - Surface-pressure and heat-transfer-rate distributions in the pitch plane of the F4:W2 for  $\alpha = 50^\circ$ .

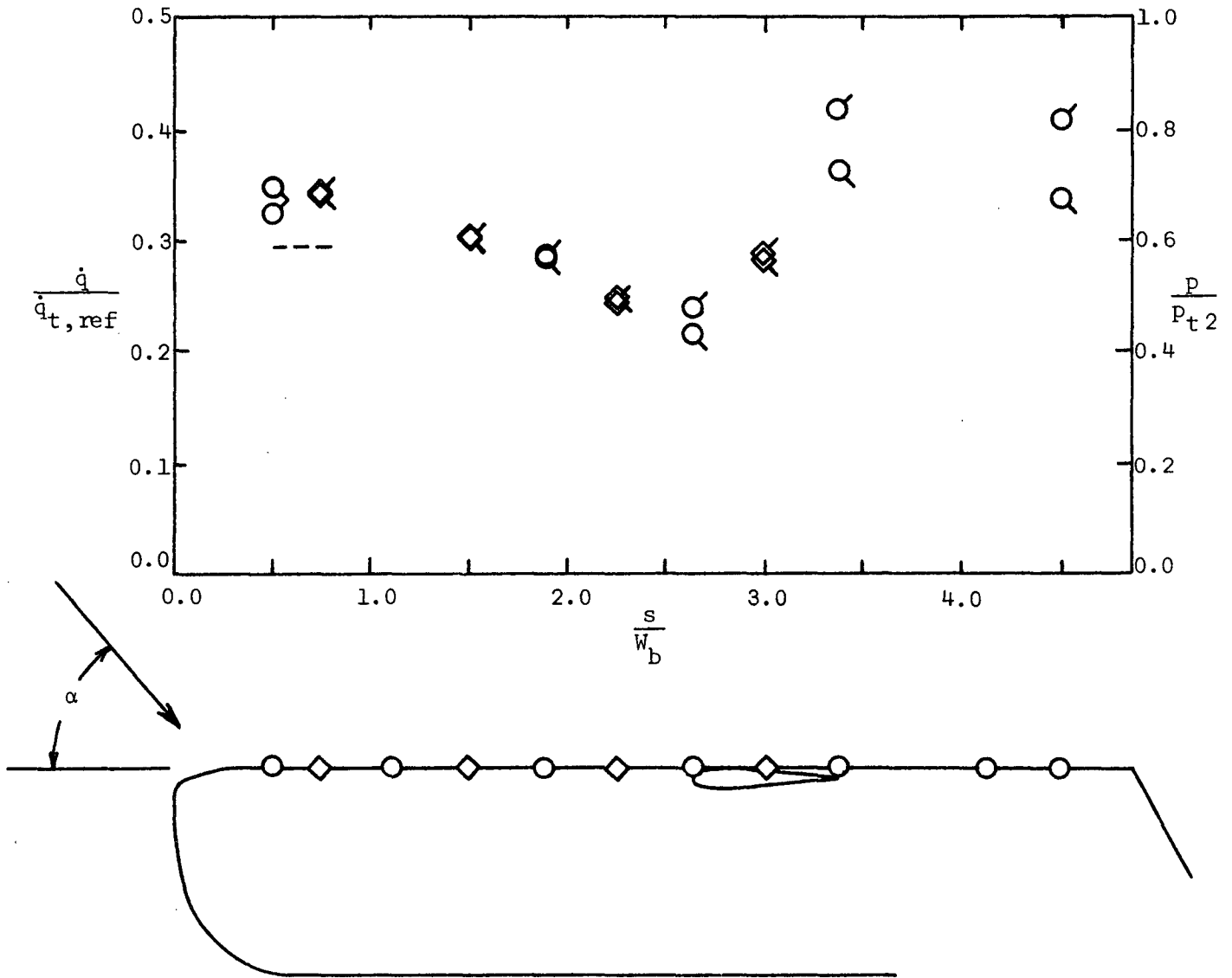
--- calculated pressure for modified Newtonian flow

◇ pressure data, or orifice location

○ heat transfer data, or thermocouple location

◇ ○ F3:W3 ,  $M_\infty = 11.9$  ,  $Re_\infty/ft = 4.3 \times 10^6$

◇ ○ F3:W2 ,  $M_\infty = 11.9$  ,  $Re_\infty/ft = 4.2 \times 10^6$



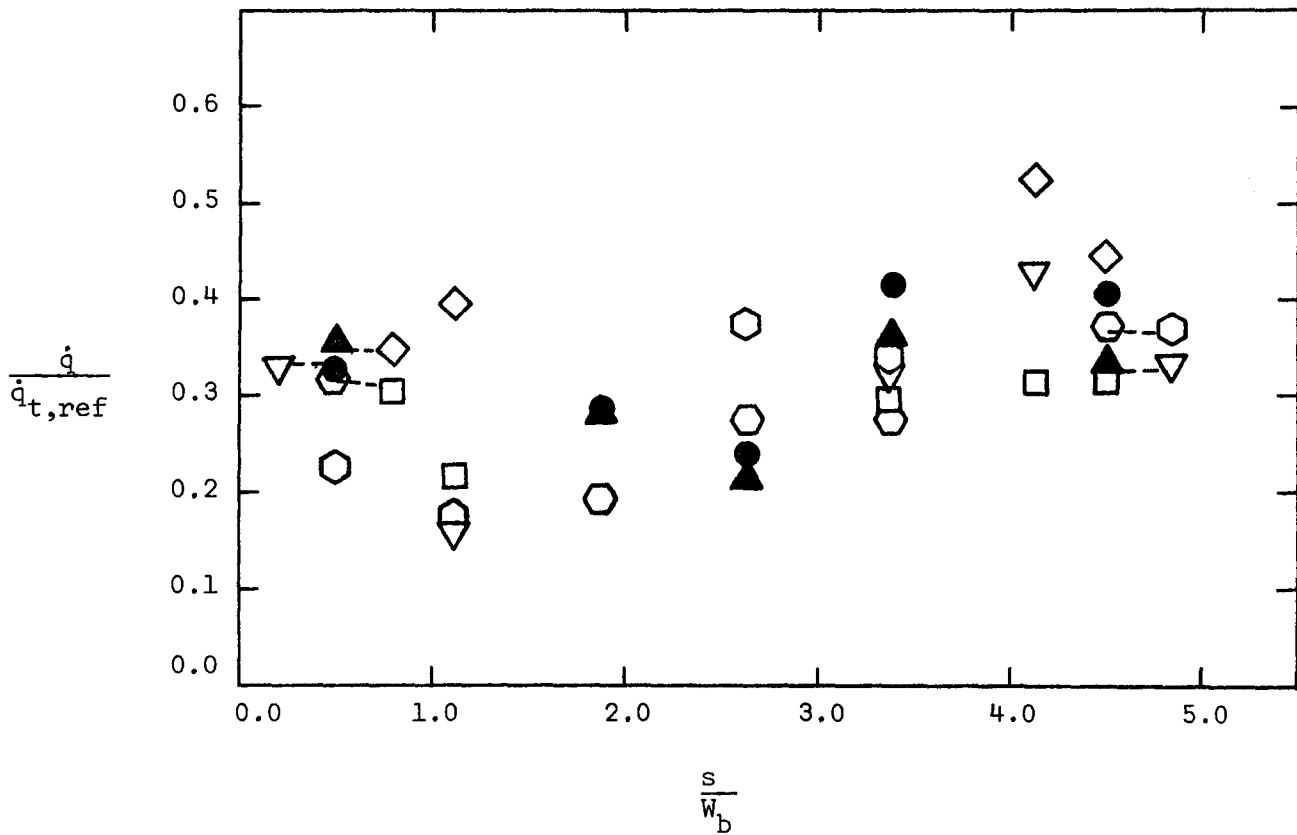
(a) Data of ref. 17 only

Figure 8. - Surface-pressure and heat-transfer-rate distributions in the pitch plane of straight-winged orbiters with an F3-fuselage for  $\alpha = 50^\circ$ .

- ▲ F3:W2,  $M_\infty = 12.0$ ,  $Re_\infty/ft = 4.0 \times 10^6$
- ▽ F3:W2,  $M_\infty = 10.3$ ,  $Re_\infty/ft = 2.2 \times 10^6$
- F3:W3,  $M_\infty = 12.0$ ,  $Re_\infty/ft = 4.0 \times 10^6$
- ⬡ F3:W3,  $M_\infty = 10.2$ ,  $Re_\infty/ft = 2.3 \times 10^6$
- ⬢ F3:W3,  $M_\infty = 10.0$ ,  $Re_\infty/ft = 14.6 \times 10^6$
- F3:W4,  $M_\infty = 10.6$ ,  $Re_\infty/ft = 2.9 \times 10^6$
- ◇ F3:W4,  $M_\infty = 9.9$ ,  $Re_\infty/ft = 13.3 \times 10^6$

filled symbols are data obtained before the tunnel-mod

open symbols are data obtained after the tunnel-mod

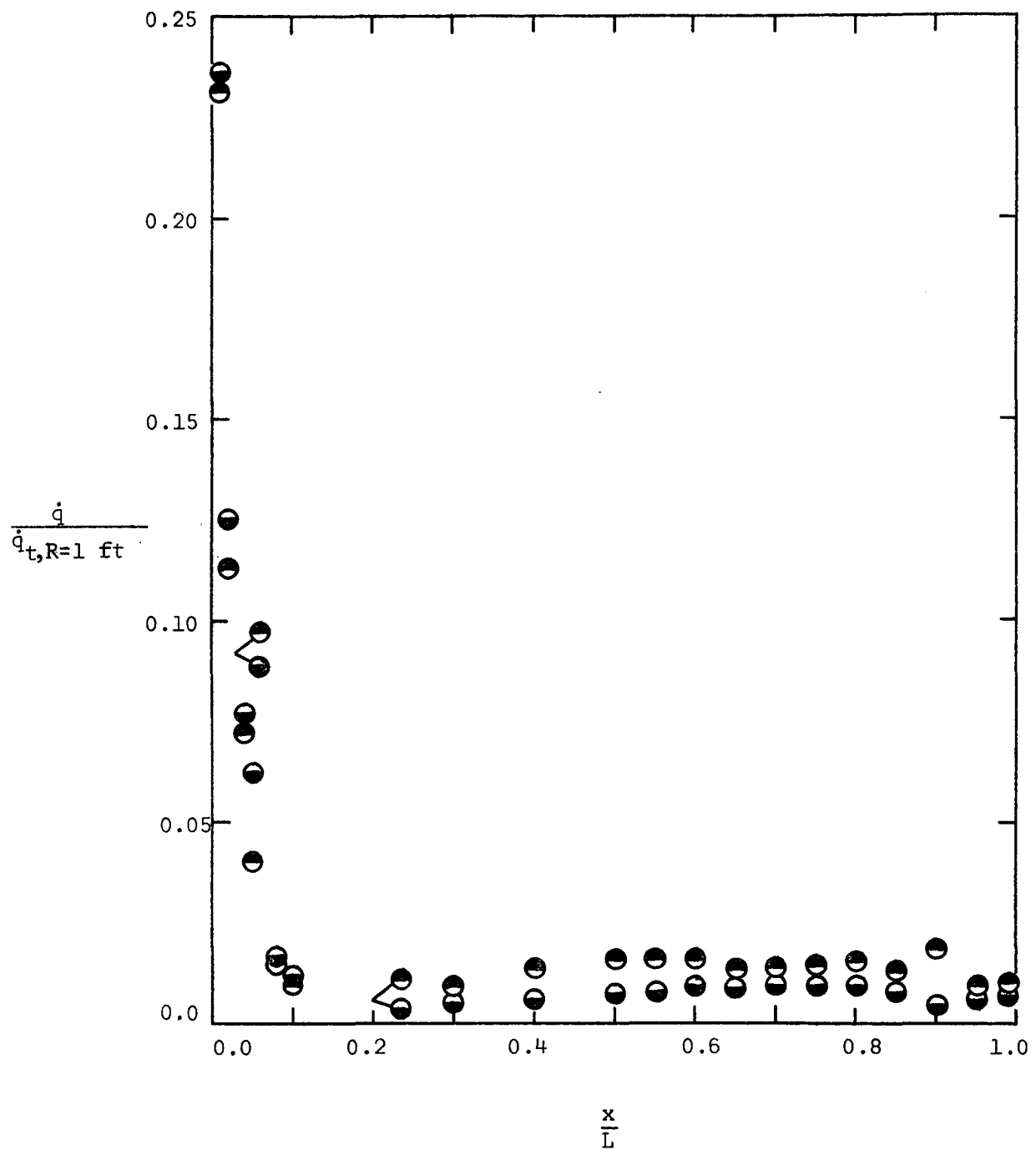


(b) All data

Figure 8. - Concluded

$$\bullet \text{Re}_{\infty,L} = 1.40 \times 10^6, M_{\infty} = 7.94$$

$$\bullet \text{Re}_{\infty,L} = 6.35 \times 10^6, M_{\infty} = 8.00$$

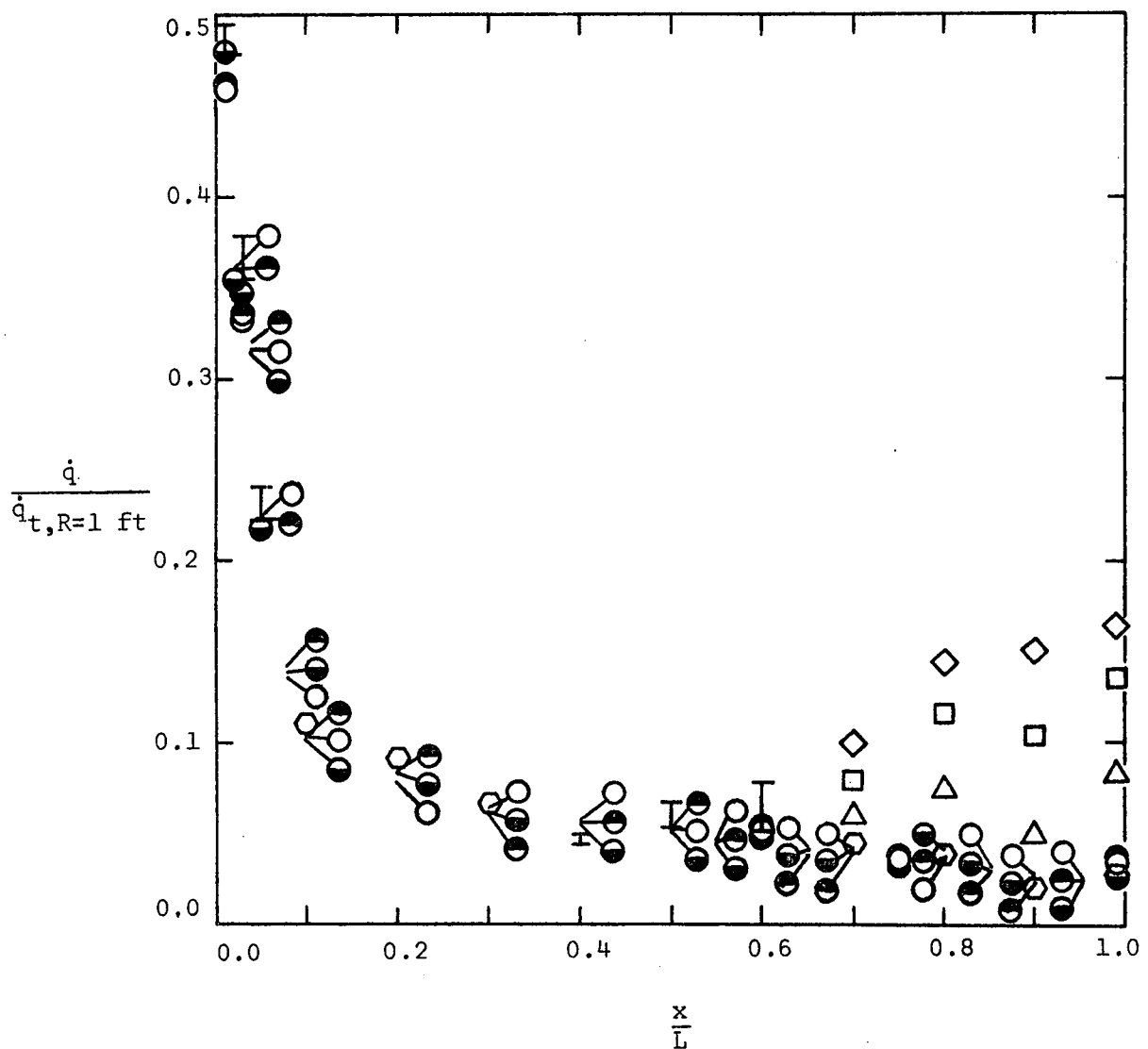


(a)  $\alpha = 0^\circ$

Figure 9, - Heat-transfer distribution in the windward pitch plane of the NAR 161B DWO, Tunnel B at AEDC.



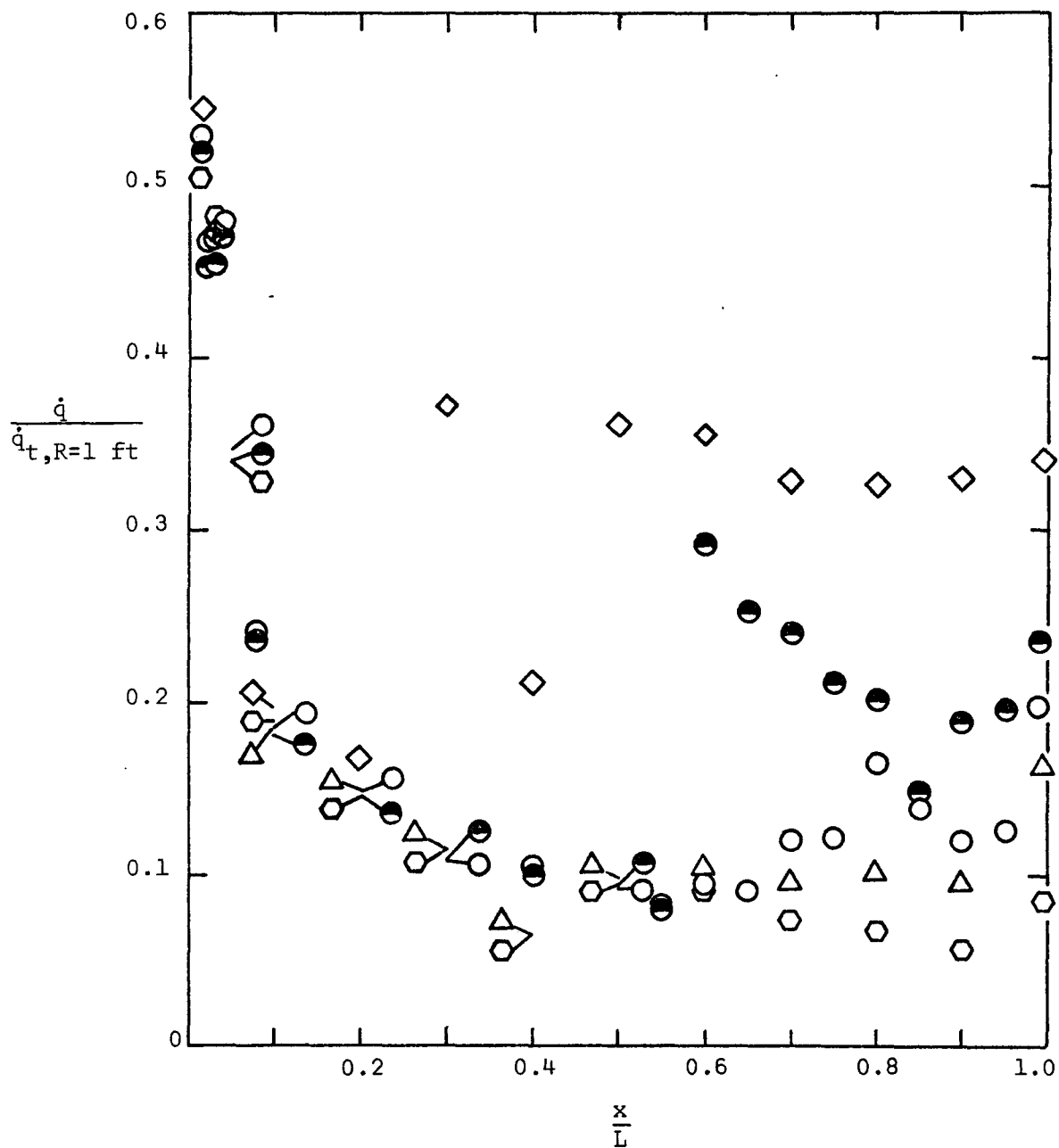
- $Re_{\infty,L} = 1.40 \times 10^6$ ,  $M_{\infty} = 7.94$
- $Re_{\infty,L} = 4.16 \times 10^6$ ,  $M_{\infty} = 8.00$
- $Re_{\infty,L} = 6.23 \times 10^6$ ,  $M_{\infty} = 8.00$
- ◻  $Re_{\infty,L} = 2.13 \times 10^6$ ,  $M_{\infty} = 7.4$ , ref 25
- △  $Re_{\infty,L} = 7.74 \times 10^6$ ,  $M_{\infty} = 7.4$ , ref 25
- ◻  $Re_{\infty,L} = 10.03 \times 10^6$ ,  $M_{\infty} = 7.4$ , ref 25
- ◇  $Re_{\infty,L} = 12.62 \times 10^6$ ,  $M_{\infty} = 7.4$ , ref 25



(b)  $\alpha = 30^\circ$

Figure 9. - Continued

- $Re_{\infty,L} = 4.16 \times 10^6$ ,  $M_{\infty} = 8.00$
- $Re_{\infty,L} = 6.22 \times 10^6$ ,  $M_{\infty} = 8.00$
- ◊  $Re_{\infty,L} = 2.32 \times 10^6$ ,  $M_{\infty} = 7.4$ , ref. 25
- △  $Re_{\infty,L} = 8.42 \times 10^6$ ,  $M_{\infty} = 7.4$ , ref. 25
- ◇  $Re_{\infty,L} = 13.37 \times 10^6$ ,  $M_{\infty} = 7.4$ , ref. 25



(c)  $\alpha = 50^\circ$

Figure 9. - Concluded



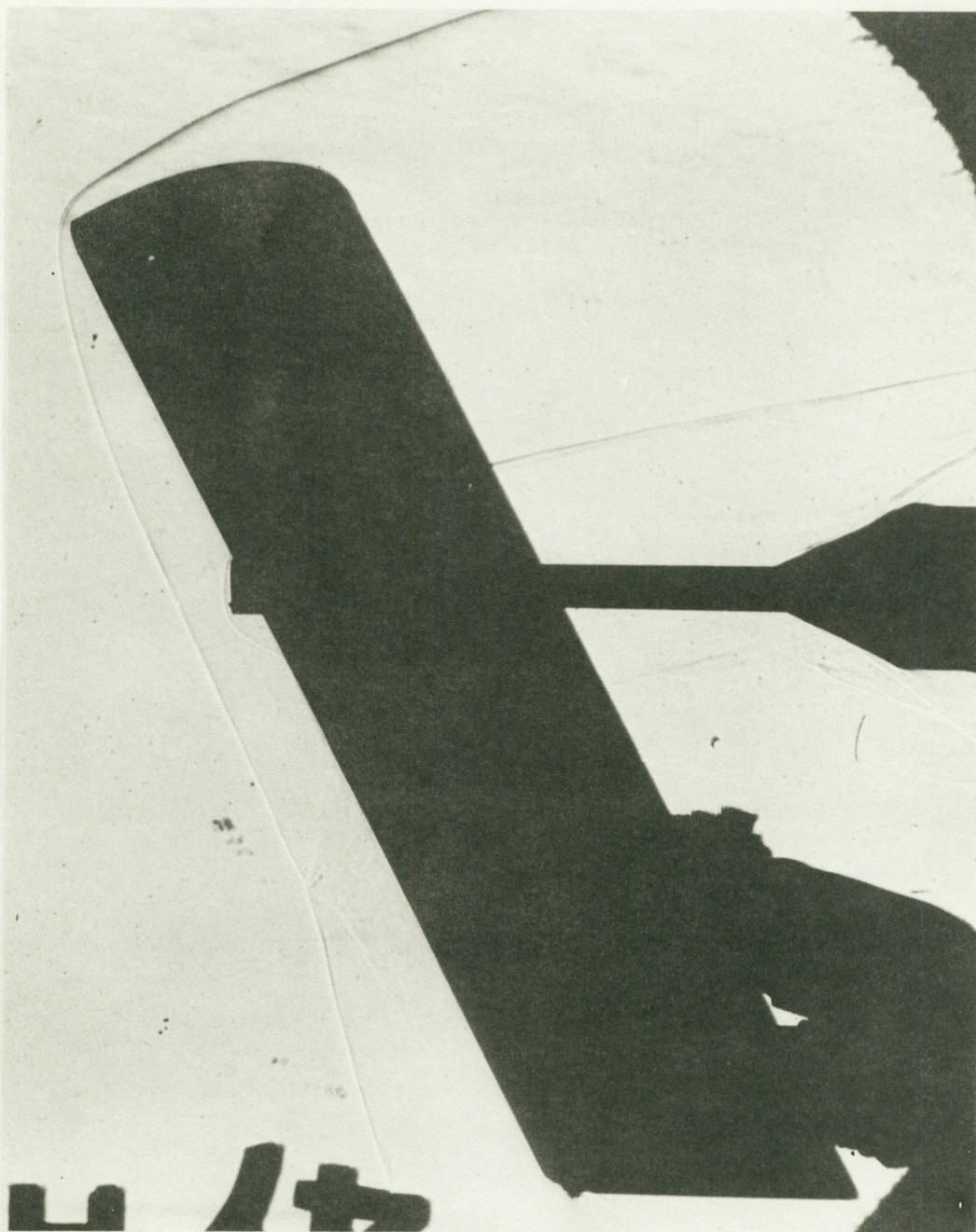


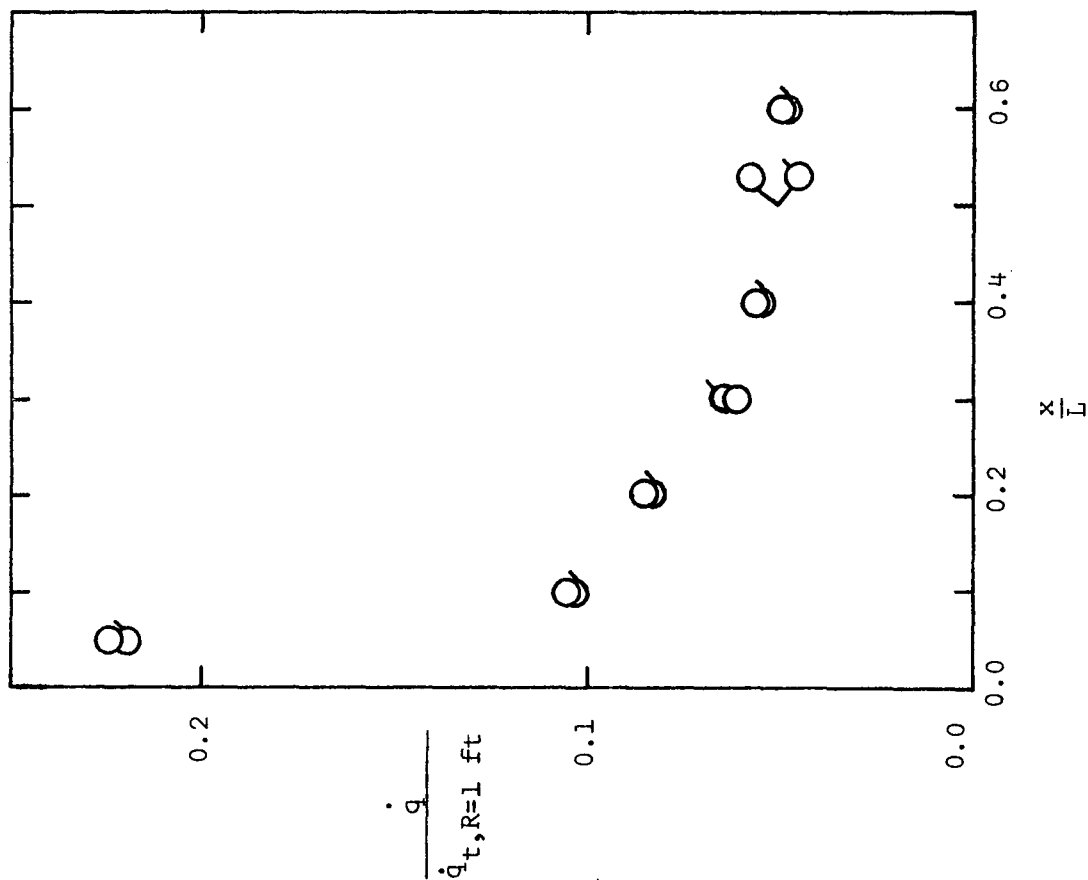
Figure 10. - Flow-field photograph of the VAC DWO  
at alpha of  $60^\circ$ ,  $M_\infty = 10.20$ ,  $Re_\infty/ft = 2.20 \times 10^6$ .



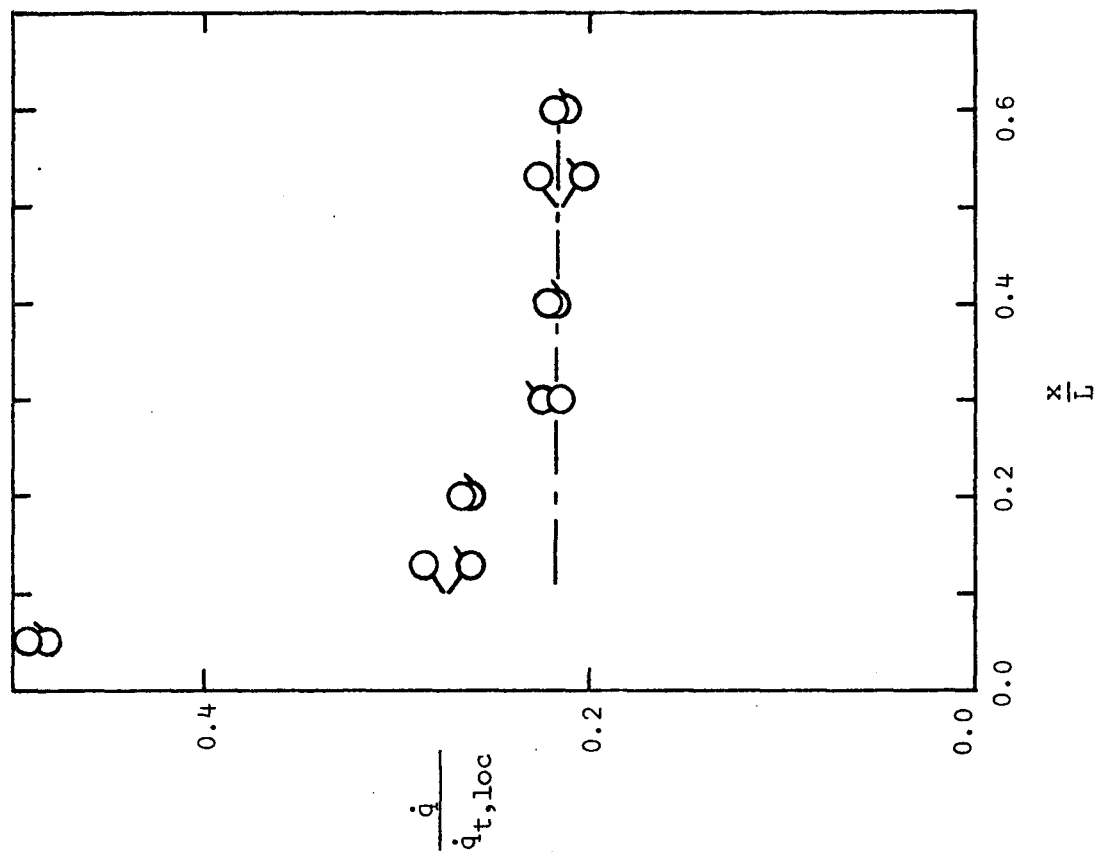
$$\sigma M_\infty = 7.94, Re_\infty/ft = 0.84 \times 10^6,$$

$$\bigcirc M_\infty = 8.00, Re_\infty/ft = 3.74 \times 10^6$$

— swept cylinder theory, equation 3



(a) Nondimensionalized by a single reference value



(b) Nondimensionalized by a reference value based on local dimensions

Figure 11. - Heat-transfer-rate distribution in the windward pitch plane for an angle-of-attack of  $30^\circ$ .

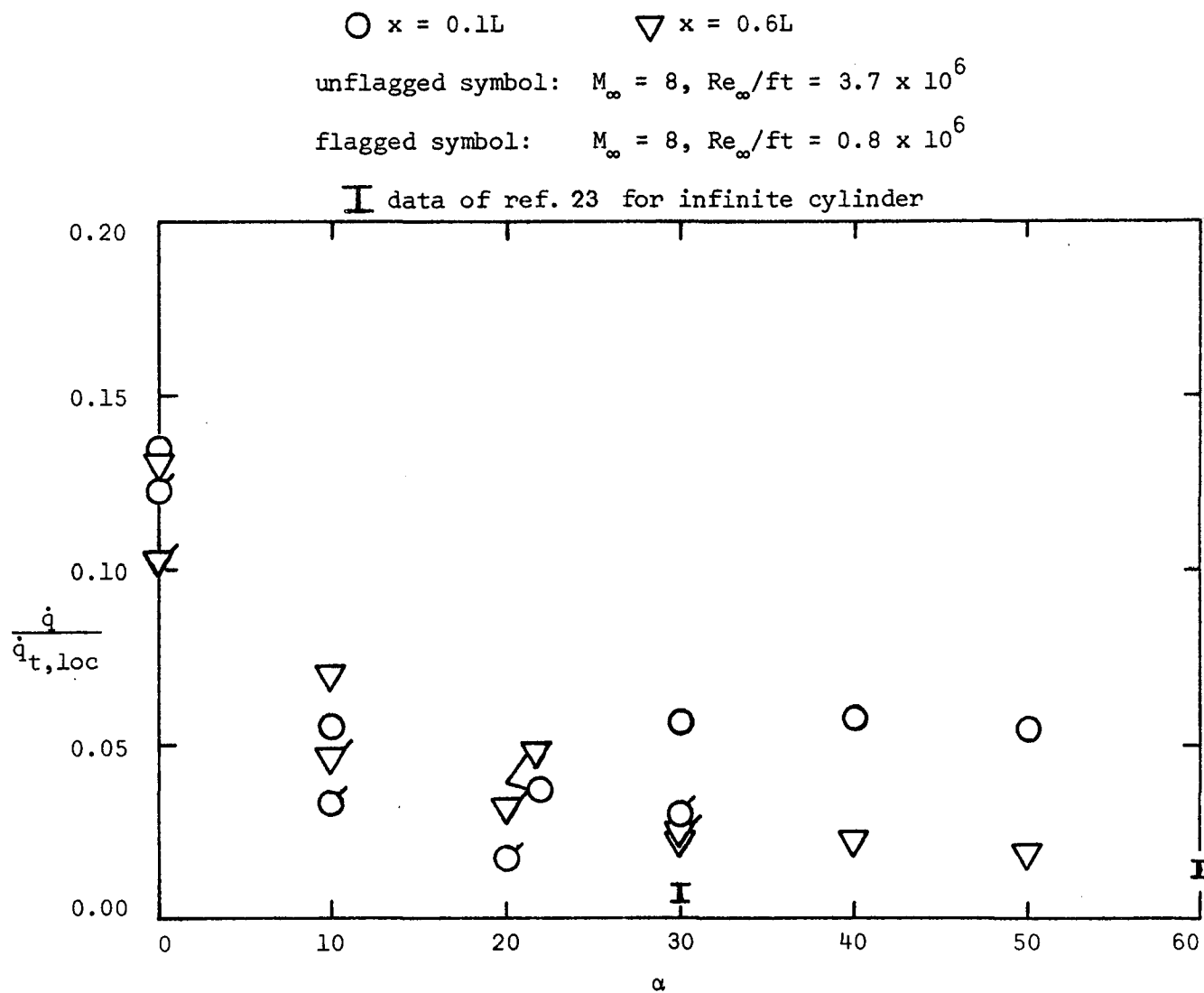
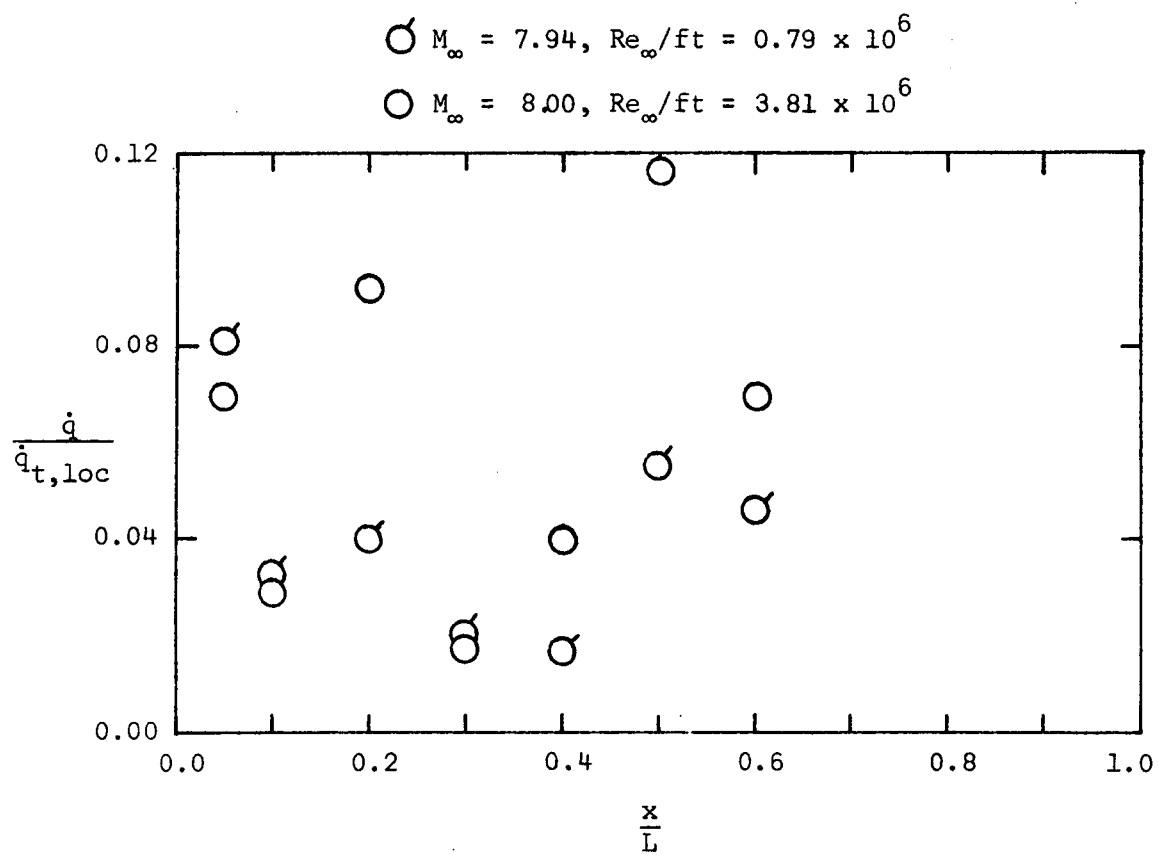
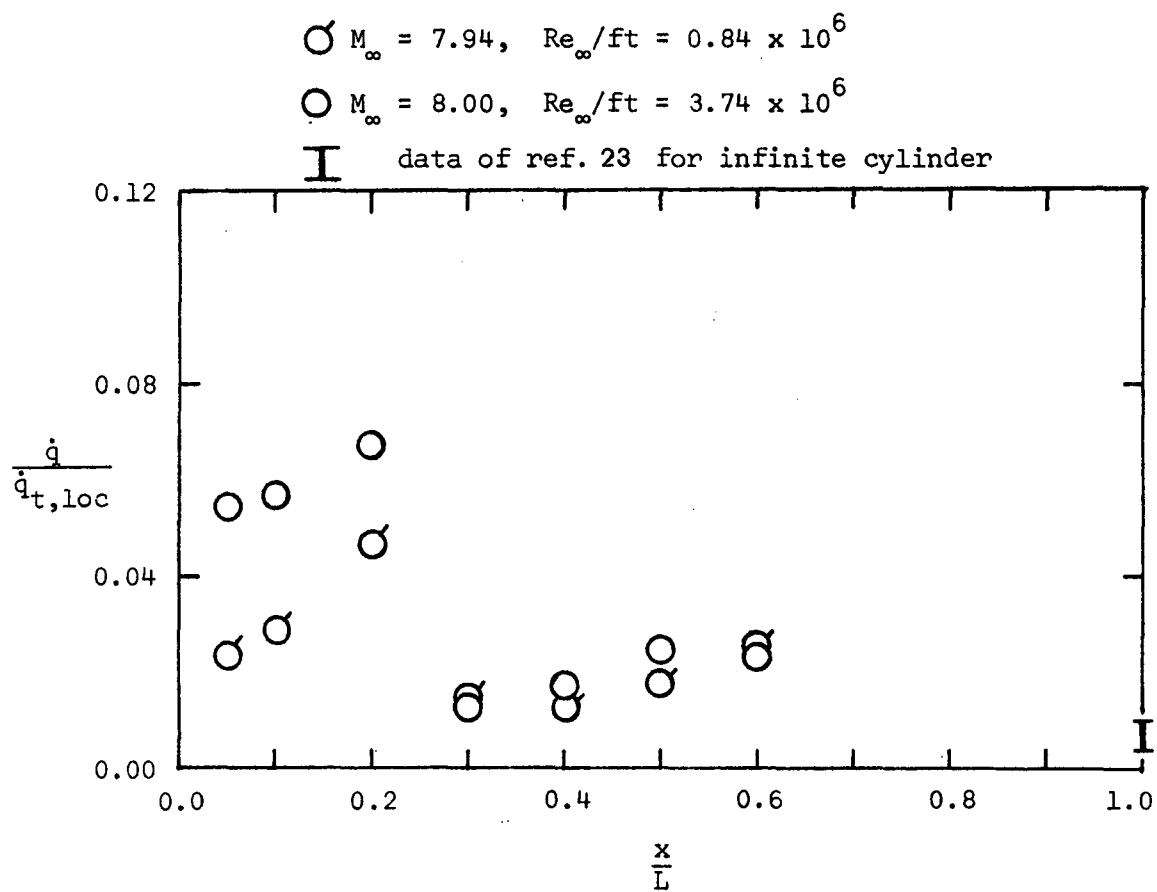


Figure 12.- Local heat-transfer rates in the leeward pitch plane as a function of the angle-of-attack.



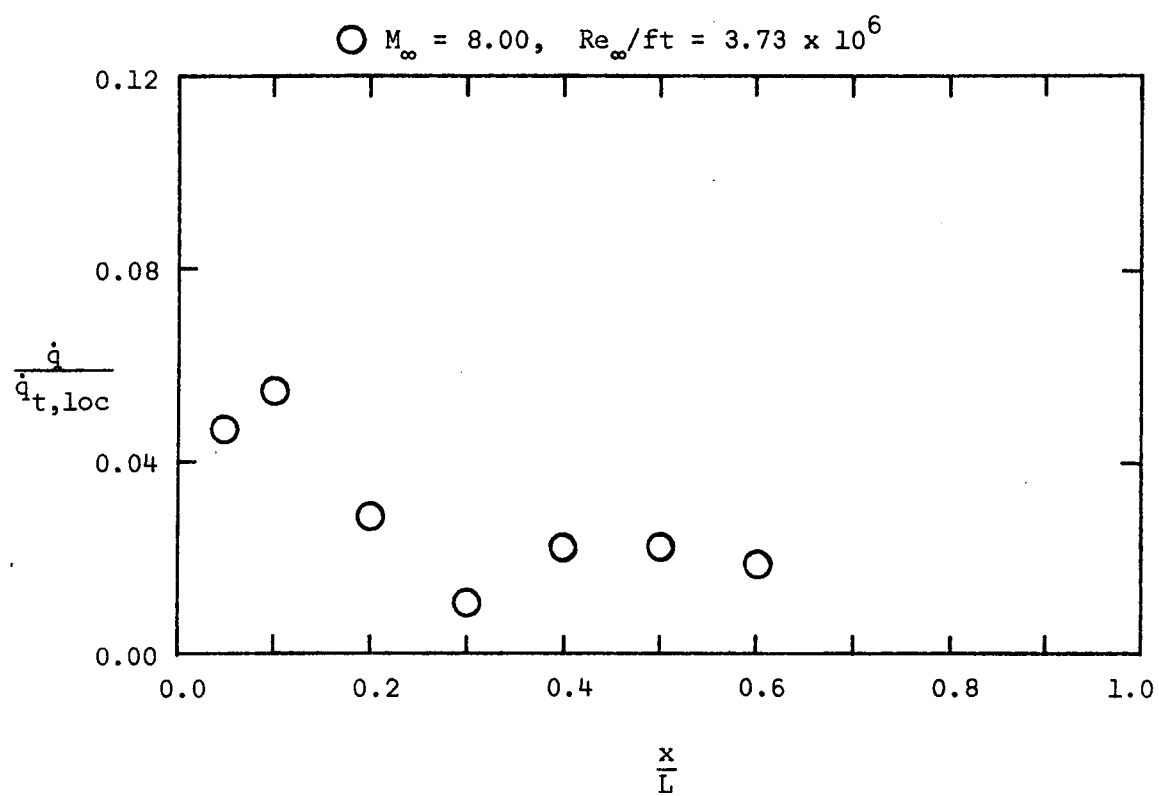
(a)  $\alpha = 10^\circ$

Figure 13.- Heat-transfer distribution in the leeward pitch plane.



(b)  $\alpha = 30^\circ$

Figure 13.- Continued.



(c)  $\alpha = 50^\circ$

Figure 13.- Concluded.



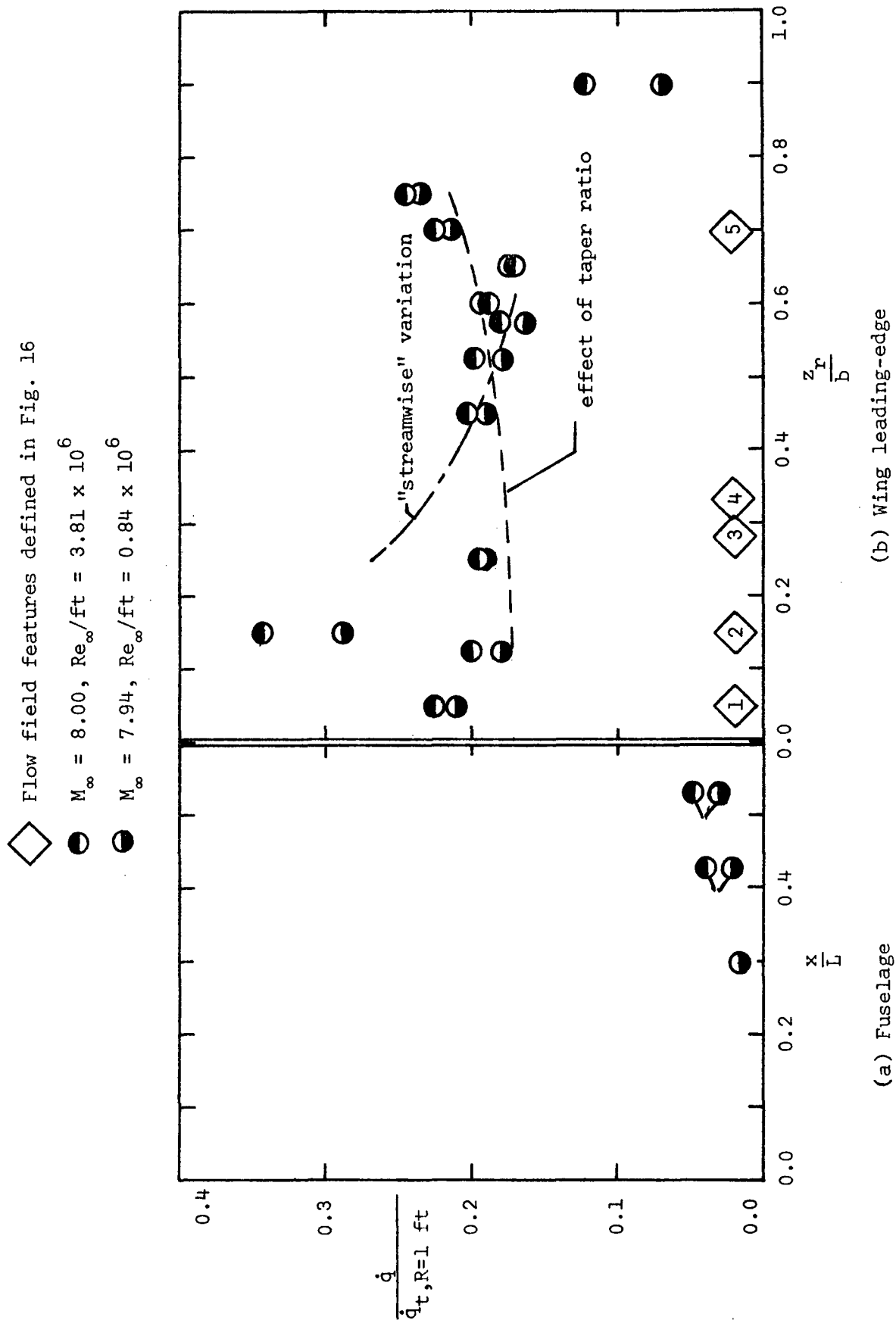
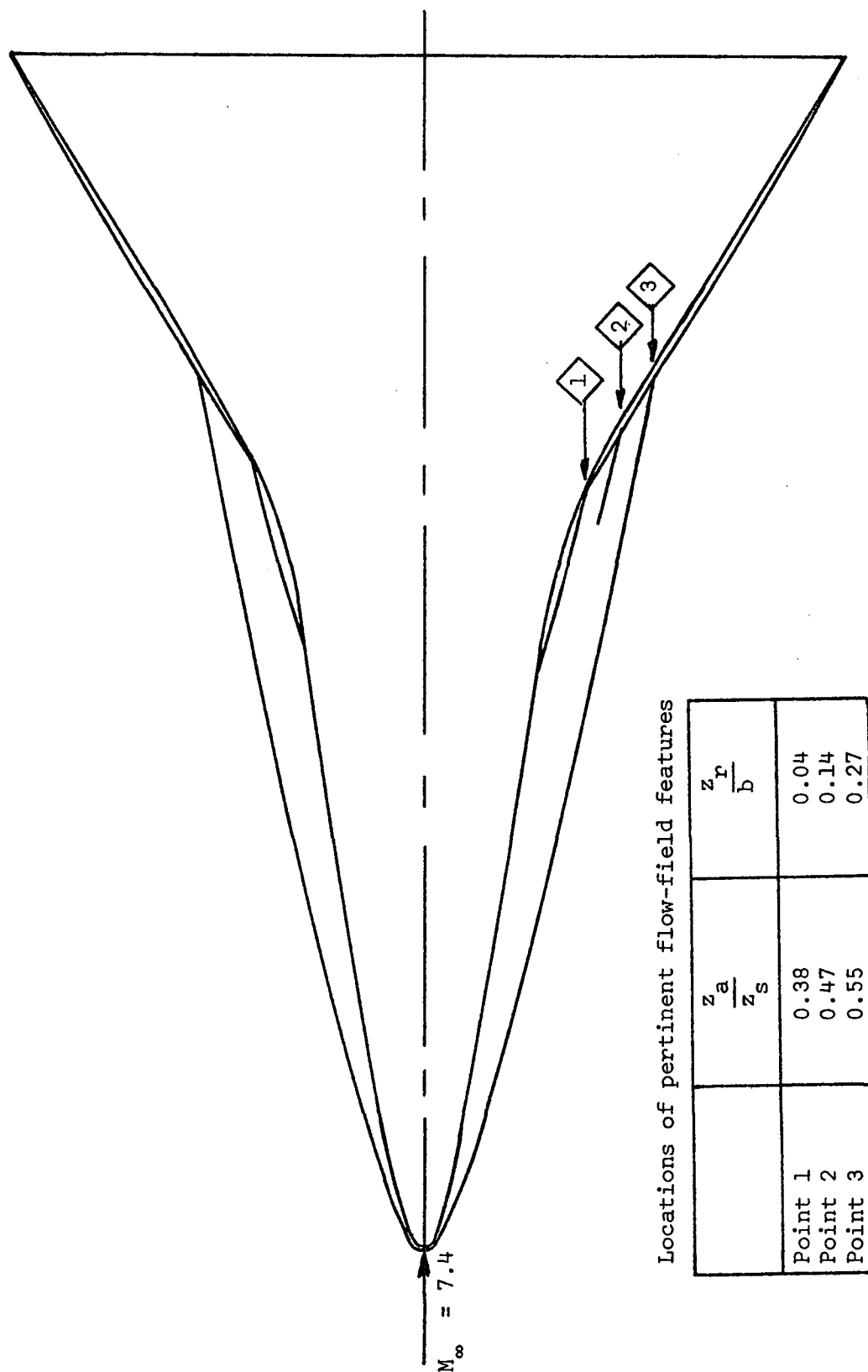


Figure 14. - The heat-transfer distribution indicating the shock-interference pattern for the NAR 161B DWO at  $\alpha = 0^\circ$ , Tunnel B.



Locations of pertinent flow-field features

	$\frac{z_a}{z_s}$	$\frac{z_r}{b}$
Point 1	0.38	0.04
Point 2	0.47	0.14
Point 3	0.55	0.27

Figure 15. - Sketch of flow-field for NAR 134 DWO as taken from Cleary (ref. 30).

Flow-field features:

1. Shock wave originating at leading edge of wing root fairing
2. Shock wave "associated" with compression of flow along fairing
3. Intersection of bow shock and wing leading-edge shock
4. Expansion waves
5. Shear layer

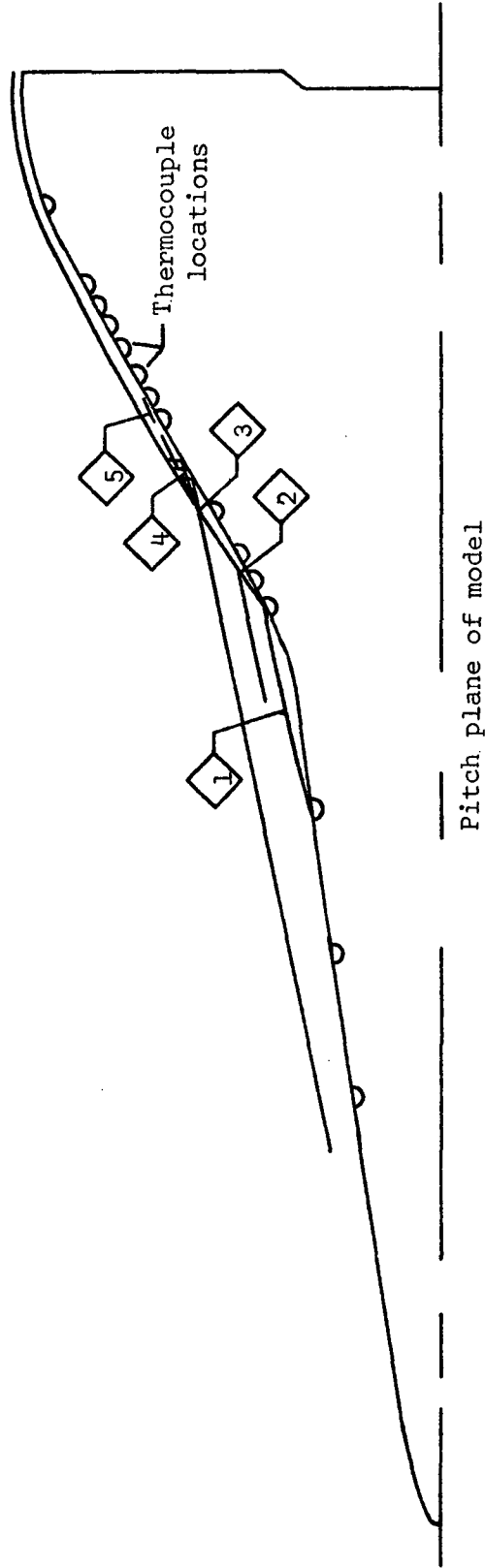


Figure 16. - The proposed shock-interference pattern for the NAR 161B DWO for  $\alpha = 0^\circ$ . (Modified Type VI interference pattern)

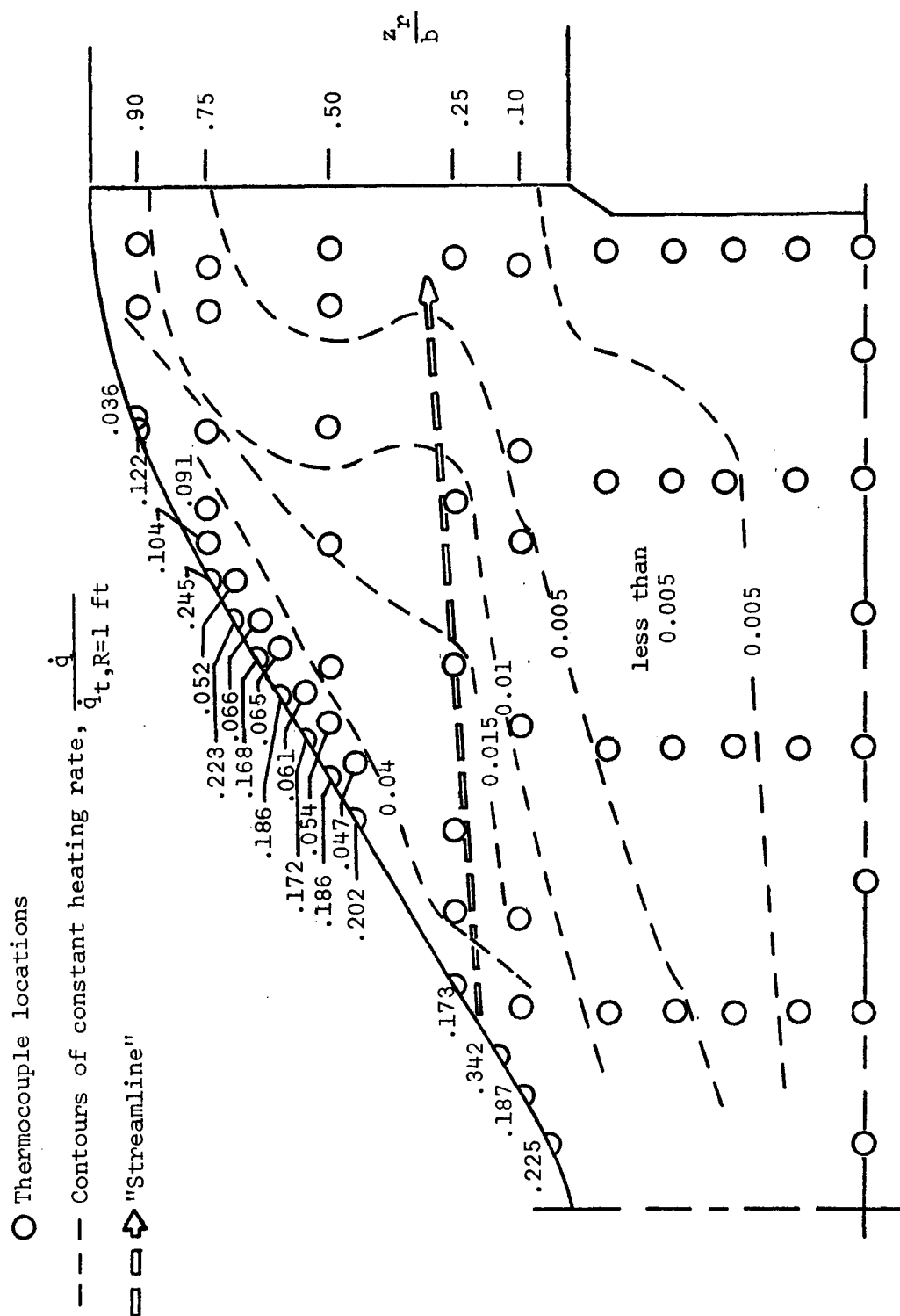
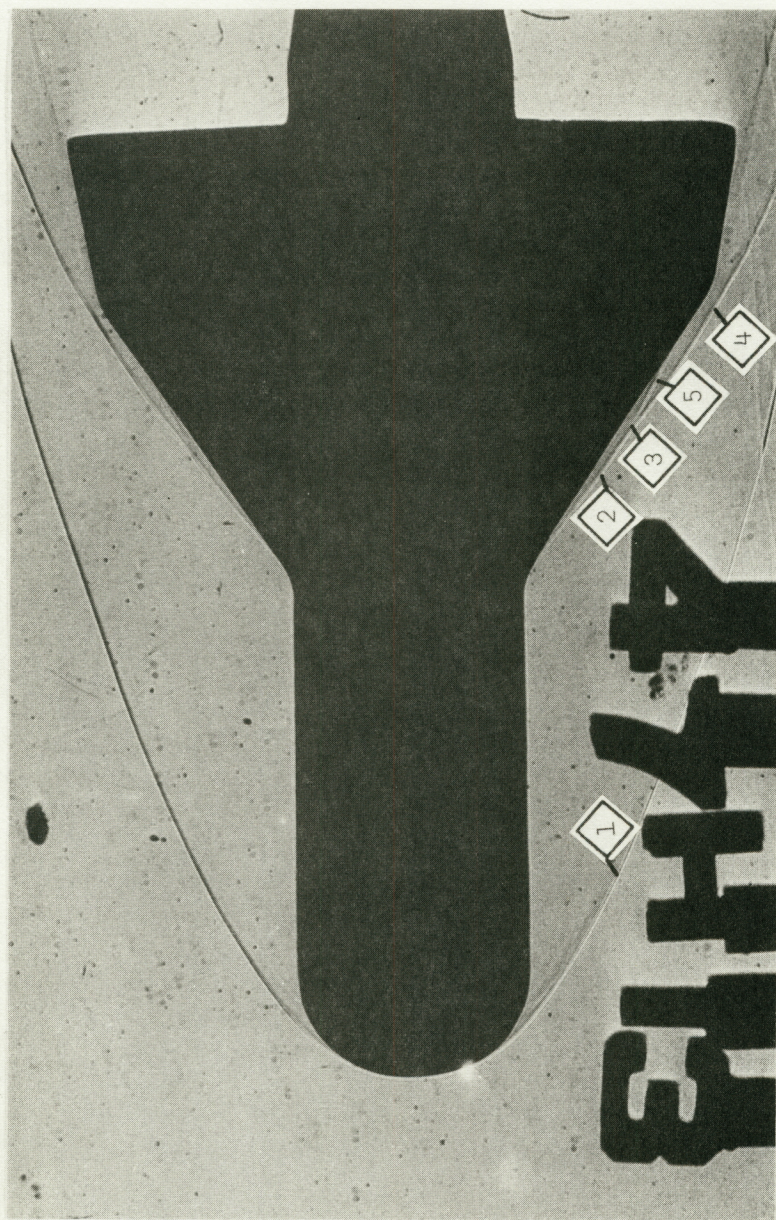



Figure 17. - Windward heat-transfer distribution over the wing and fuselage of the NAR 161B DWO at an  $\alpha = 0^\circ$ ,  $M_\infty = 8.00$ ,  $Re_\infty / ft = 3.81 \times 10^6$ .





$M_\infty = 10.61$   


(a) F3:W4 (Run No. 1013 in Table 2)

Figure 18. - Flow fields for delta-wing orbiters at an alpha of 30°



# Flow-field features

1. Trace of the fuselage-generated (or bow) shock wave
2. Wing-generated shock wave inboard of the shock:shock intersection
3. The "location" of shock:shock intersection
4. Wing-generated shock wave outboard of the shock:shock intersection

$M_{\infty} = 7.4$  →

5. Curve which traces the intersection of the surface of the bow-generated shock wave with the "outboard" surface of the wing-generated shock wave
6. (assumed) Fuselage-generated shock wave in the plane of the shock:shock intersection

(b) NAR 134 DWO (ref. 30)

Figure 18. - Concluded.

Shock-interference  
pattern (for an  
alpha of 0°)

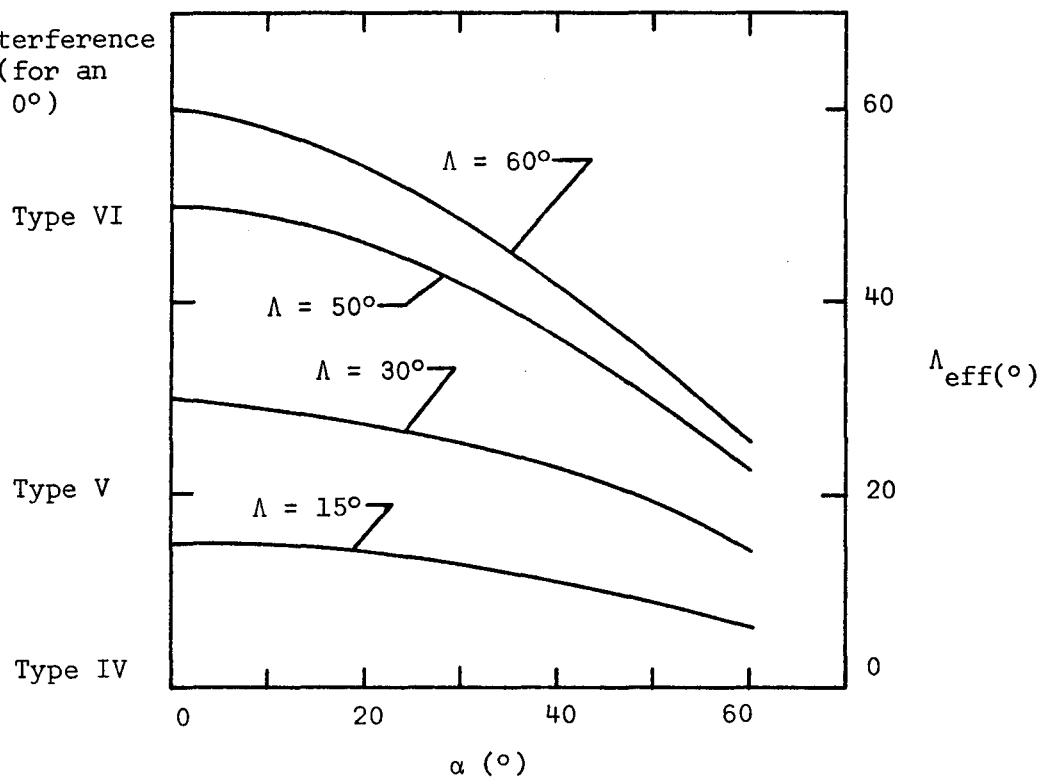


Figure 19. - Effective sweep-angle as a function  
of the angle-of-attack.

$\Delta M_\infty = 10.61, Re_{\infty,L} = 1.05 \times 10^6$	F3:W4, VAC HVWT
$\bullet M_\infty = 7.94, Re_{\infty,L} = 1.40 \times 10^6$	} NAR 161B, Tunnel B
$\circ M_\infty = 8.00, Re_{\infty,L} = 4.19 \times 10^6$	
$\bullet M_\infty = 8.00, Re_{\infty,L} = 6.25 \times 10^6$	
$\text{I} M_\infty = 7.4, Re_{\infty,L} = 2.13 \times 10^6$ to $12.28 \times 10^6$	NAR 161B, ref. 25

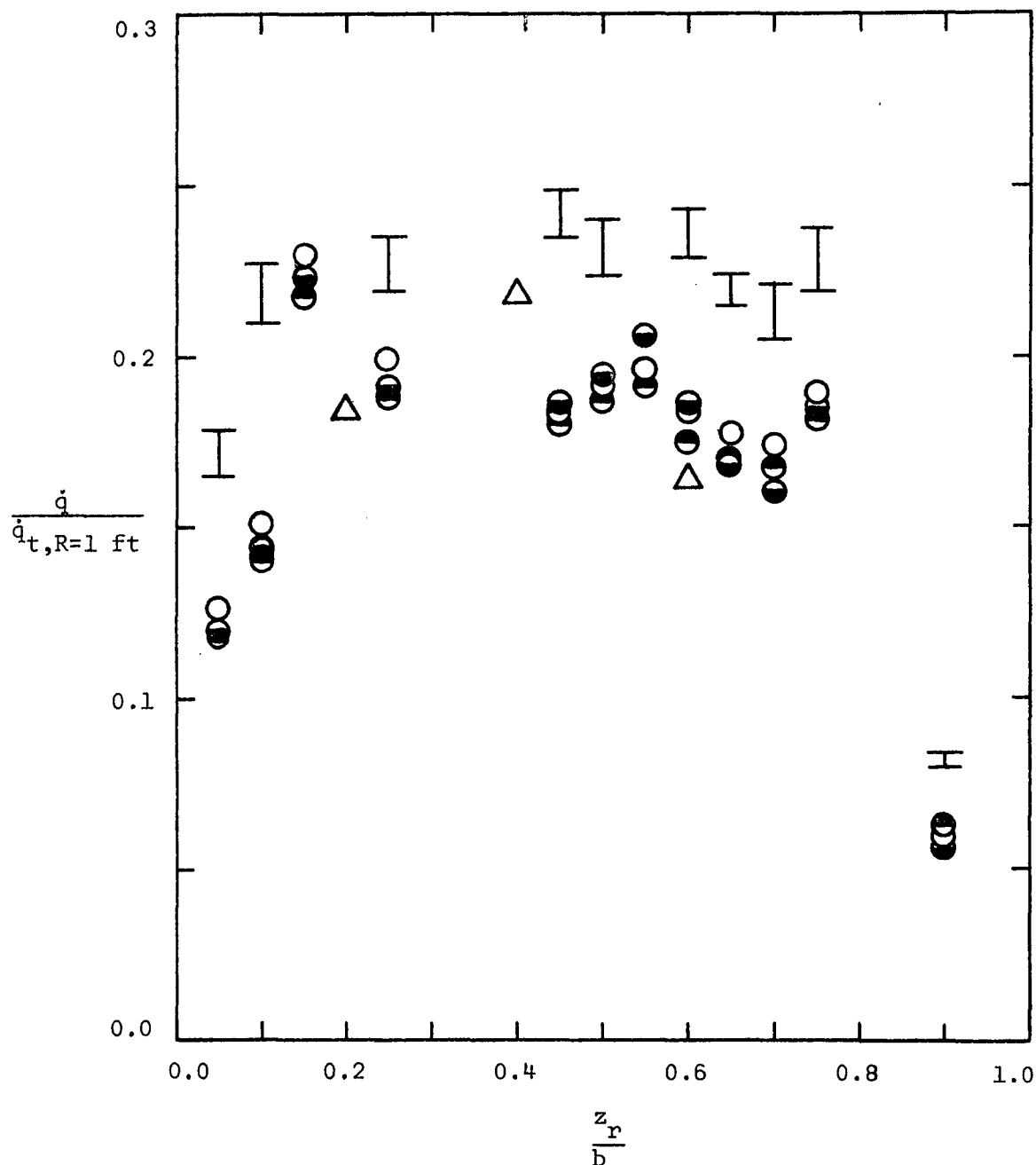


Figure 20. - The heat-transfer distribution along the wing leading-edge for delta-wing orbiters ( $\Lambda = 60^\circ$ ) at an  $\alpha$  of  $30^\circ$ .



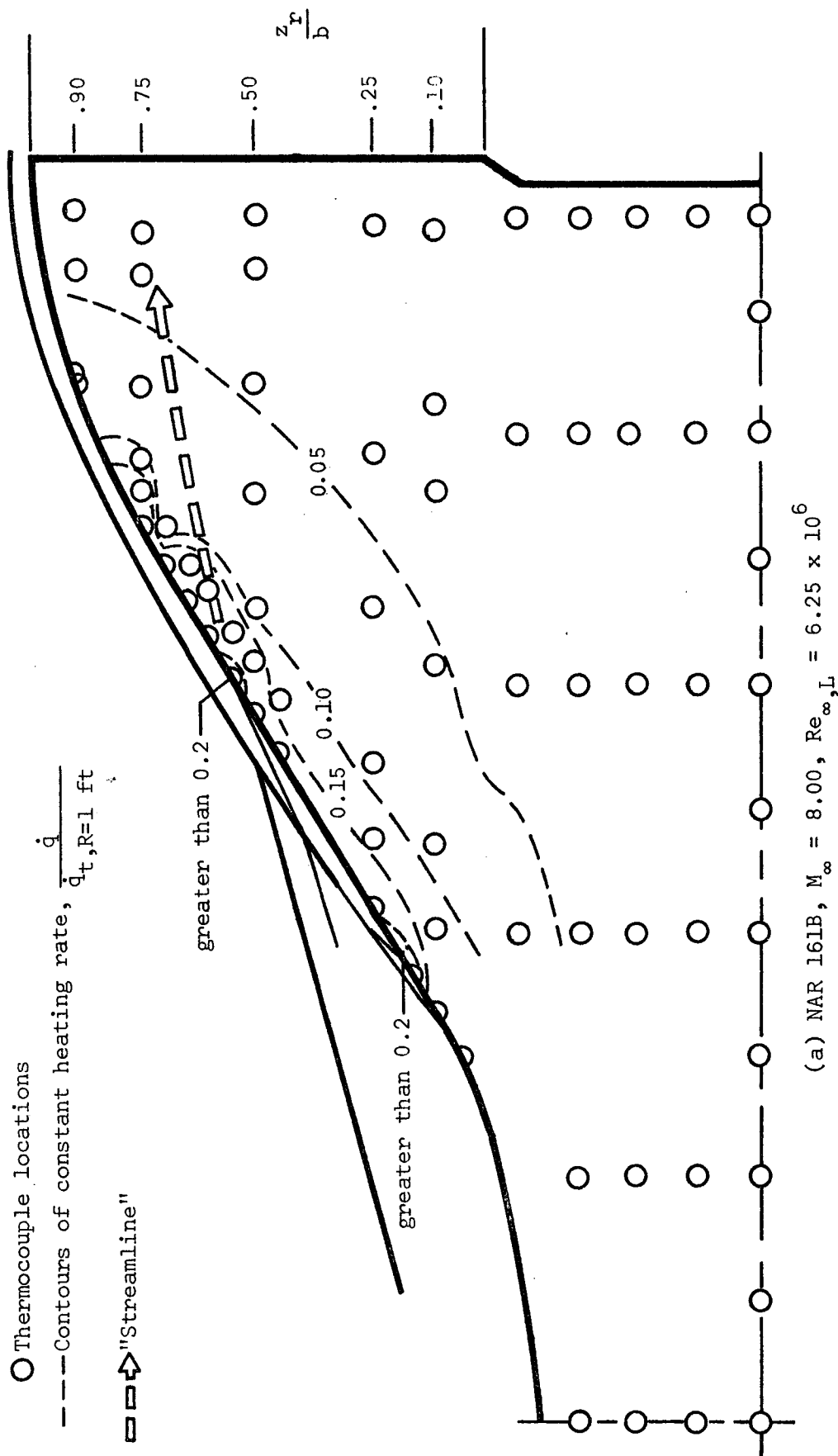
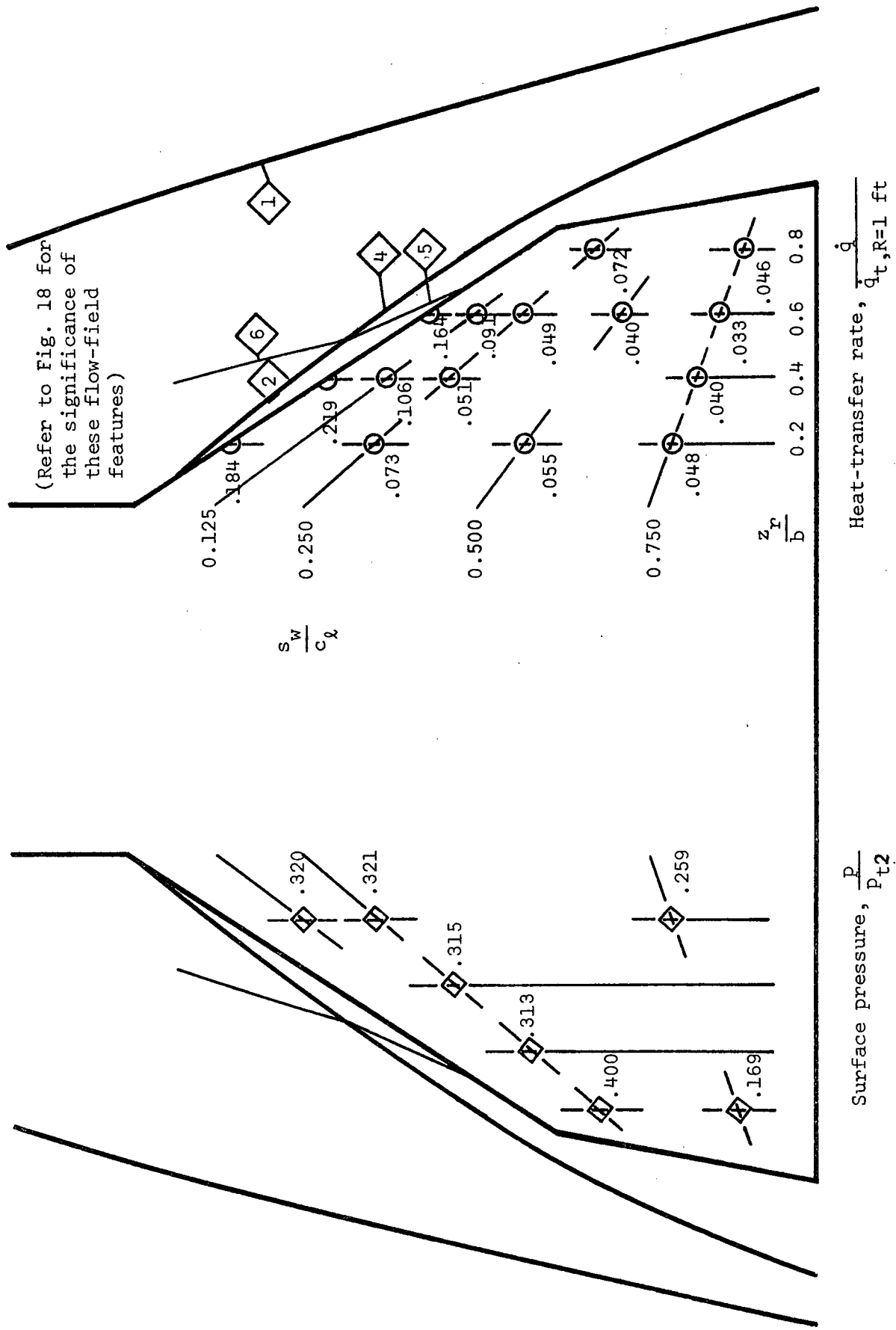
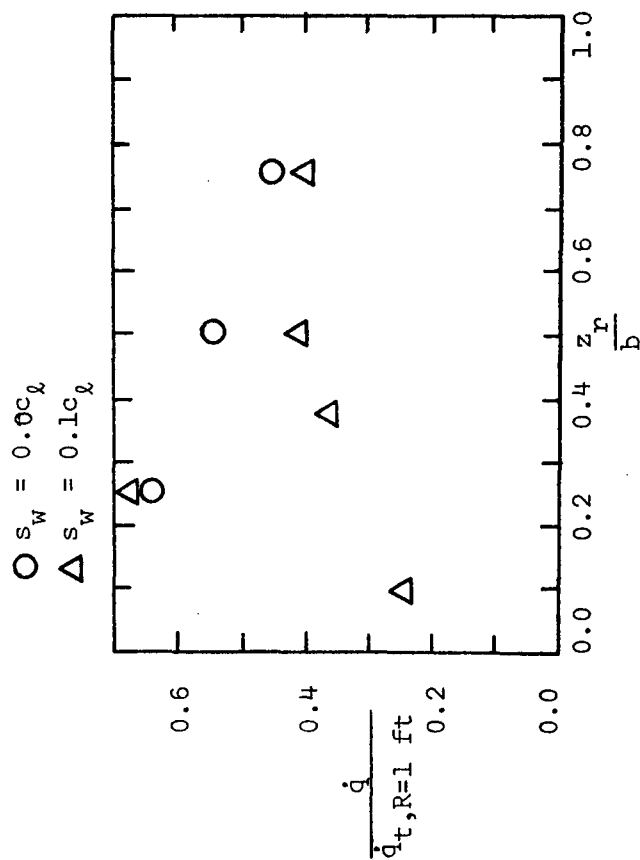
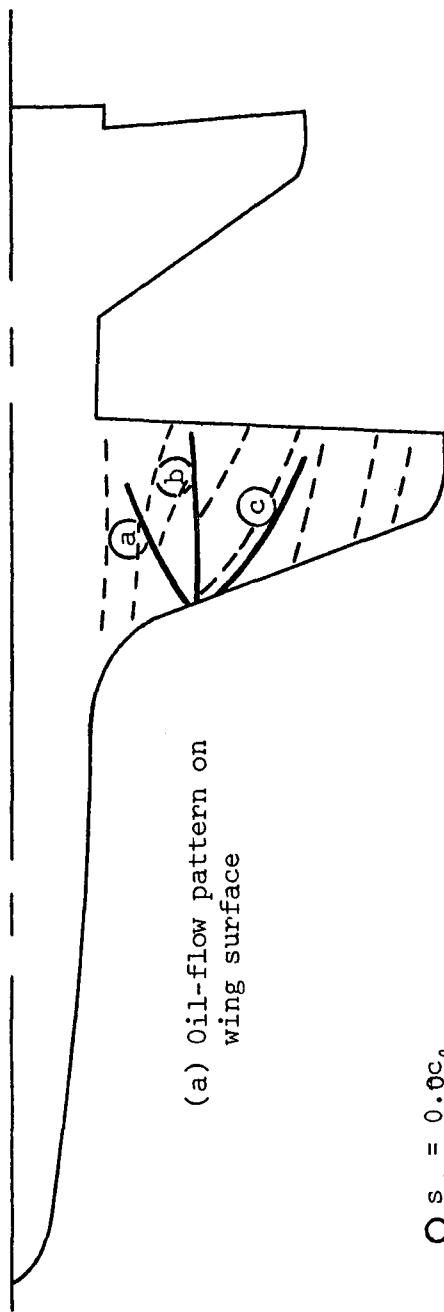


Figure 21. - Flow-field measurements on the wing surface for the delta-wing orbiters at an alpha of 30°.



(b) F3:W4,  $M_\infty = 10.61$ ,  $Re_{\infty, L} = 1.05 \times 10^6$

Figure 21. - Concluded



(b) Spanwise heating-rate distribution;  
 $M_\infty = 7.4$ ,  $Re_{\infty,L} = 1.05 \times 10^6$

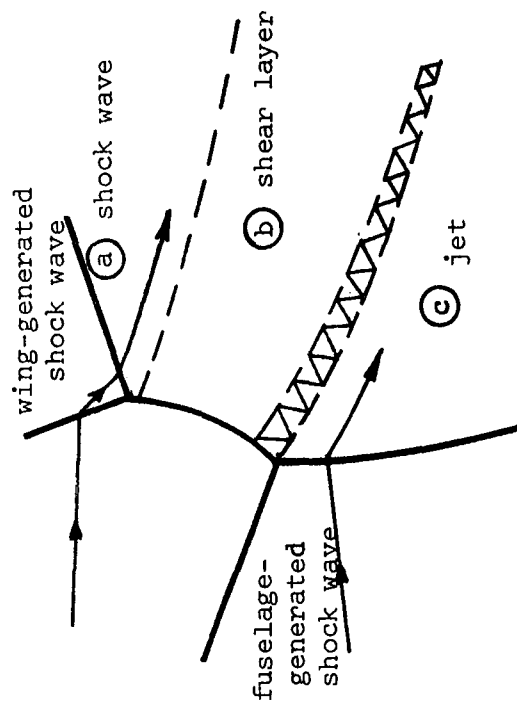


Figure 22. - Flow-field for the wing surface of the NAR straight-wing orbiter at an alpha of 30° (ref. 13).

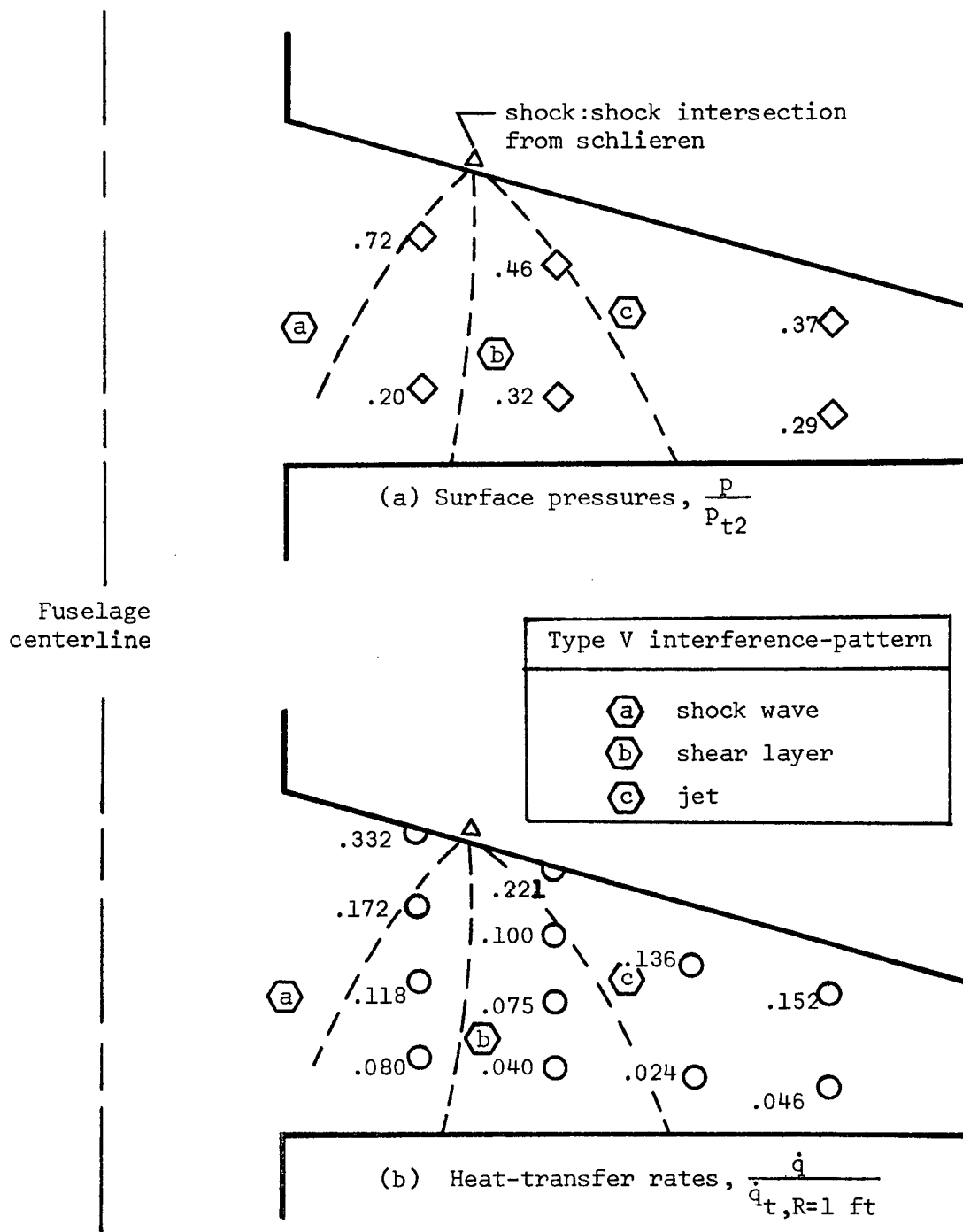


Figure 23. - Surface-pressures and heat-transfer rates on the windward wing surface of the F3:W2 at an alpha of 30°.  $M_\infty = 10.31$ ,  $Re_\infty/\text{ft} = 2.35 \times 10^6$ .

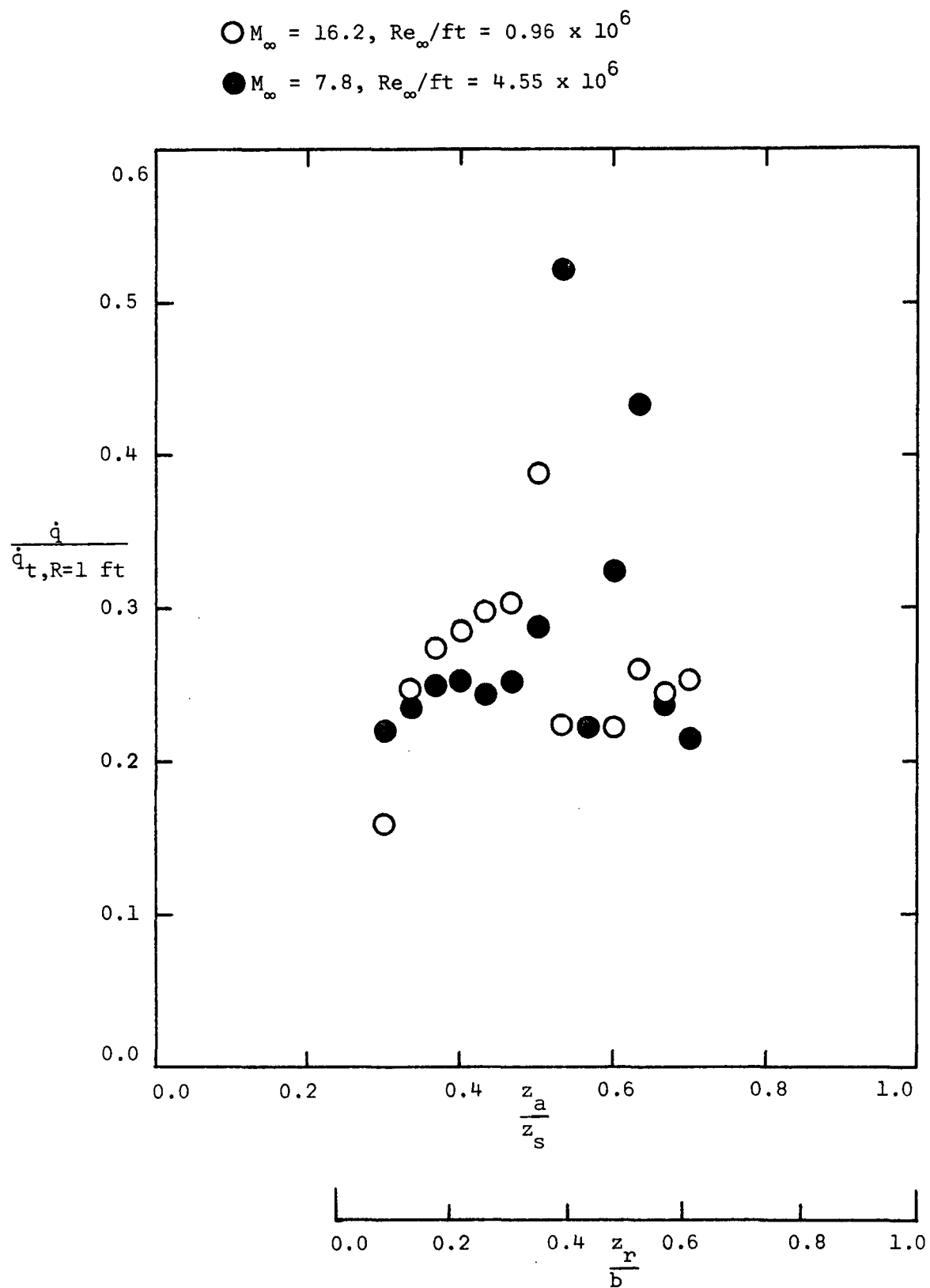


Figure 24. - Spanwise heat-transfer distribution for  $s_w = 0.15c_l$  on NASA SWO at an alpha of  $30^\circ$ .

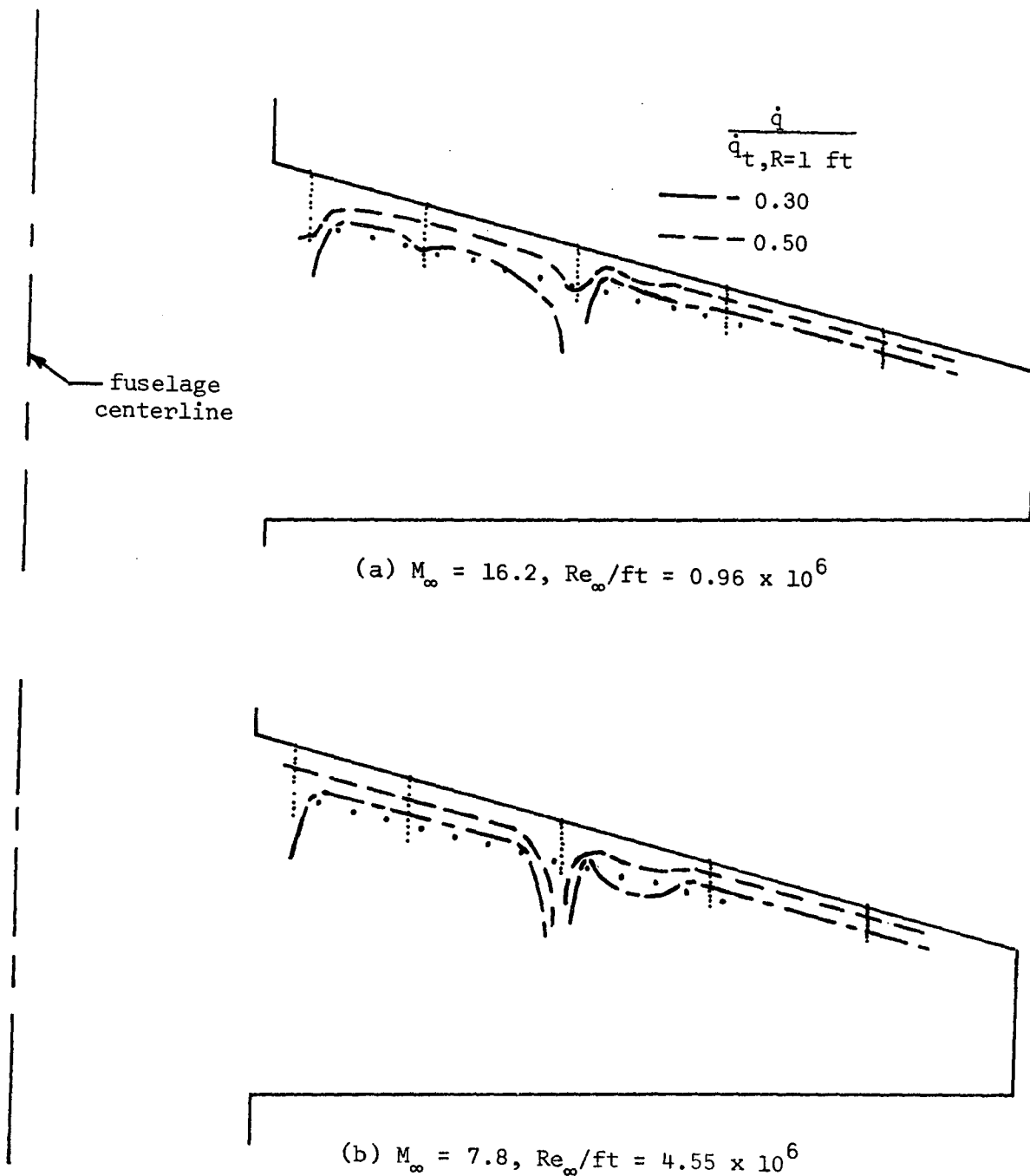
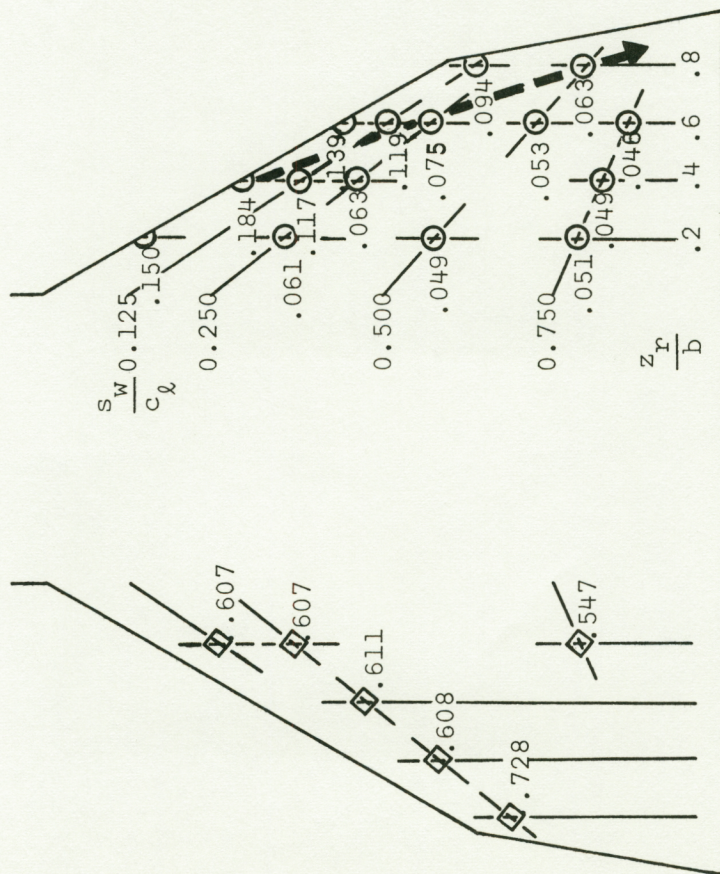


Figure 25. - Constant heating-rate contours in the vicinity of the leading edge of the NASA SWO at an alpha of  $30^\circ$ .

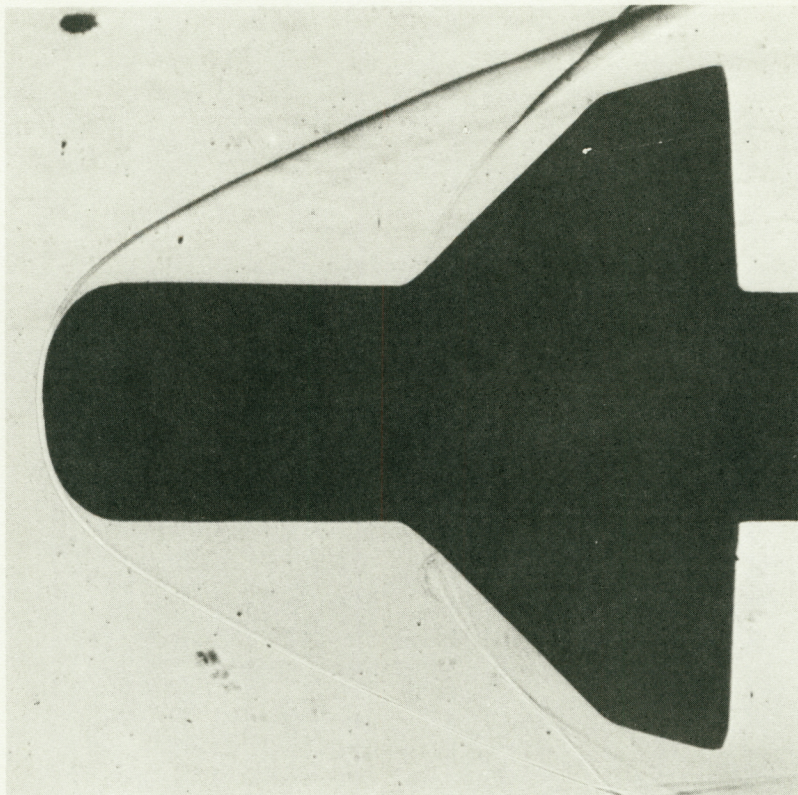


- > "Streamline"
- Thermocouple
- ◇ Pressure orifice



(a) Surface pressure,  $\frac{P}{P_{t2}}$

(b) Heat-transfer rate,  $\frac{\dot{q}}{\dot{q}_t, R=1 \text{ ft}}$



(c) Flow-field photograph

Figure 26. - Flow-field data for the wing of the F3:W4 at an alpha of 50°.

$M_\infty = 10.60$ ,  $Re_{\infty, L} = 1.16 \times 10^6$ .



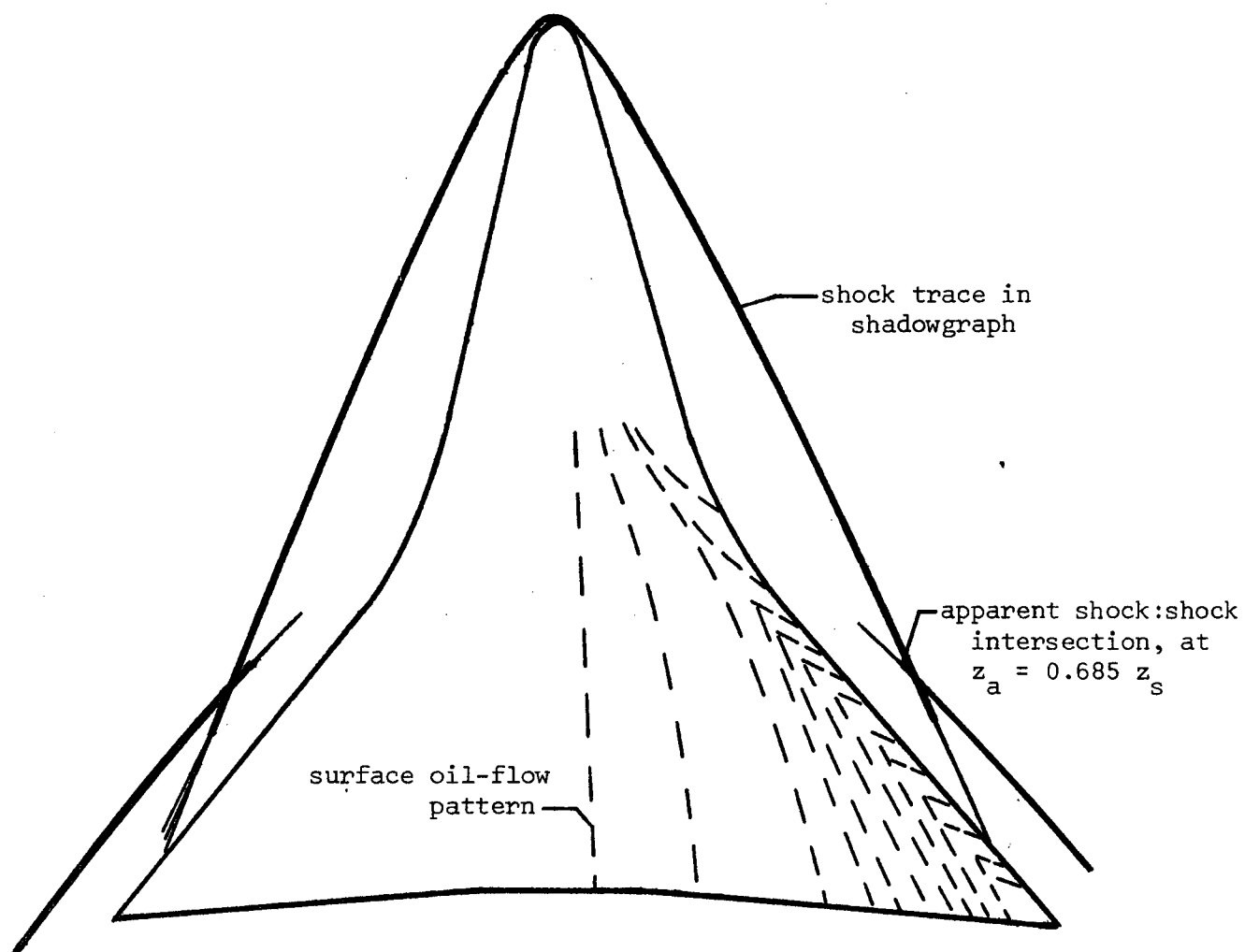


Figure 27. - Sketch of flow-field for NAR 134 DW0 at an alpha of  $50^\circ$  as taken from Cleary (ref. 30).



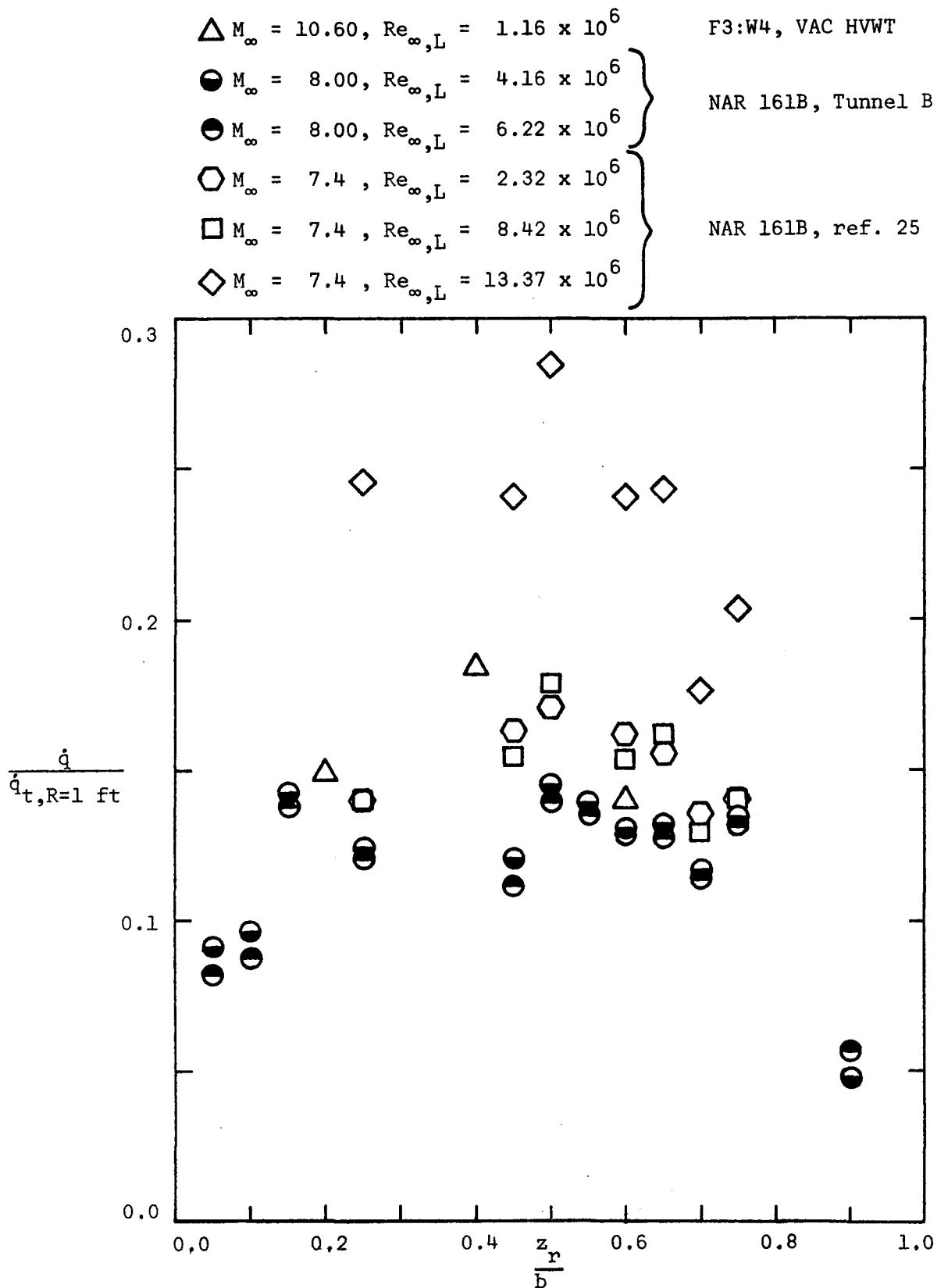


Figure 28, - The heat-transfer distribution along the wing leading-edge for delta-wing orbiters ( $\Lambda = 60^\circ$ ) at an alpha of  $50^\circ$ .

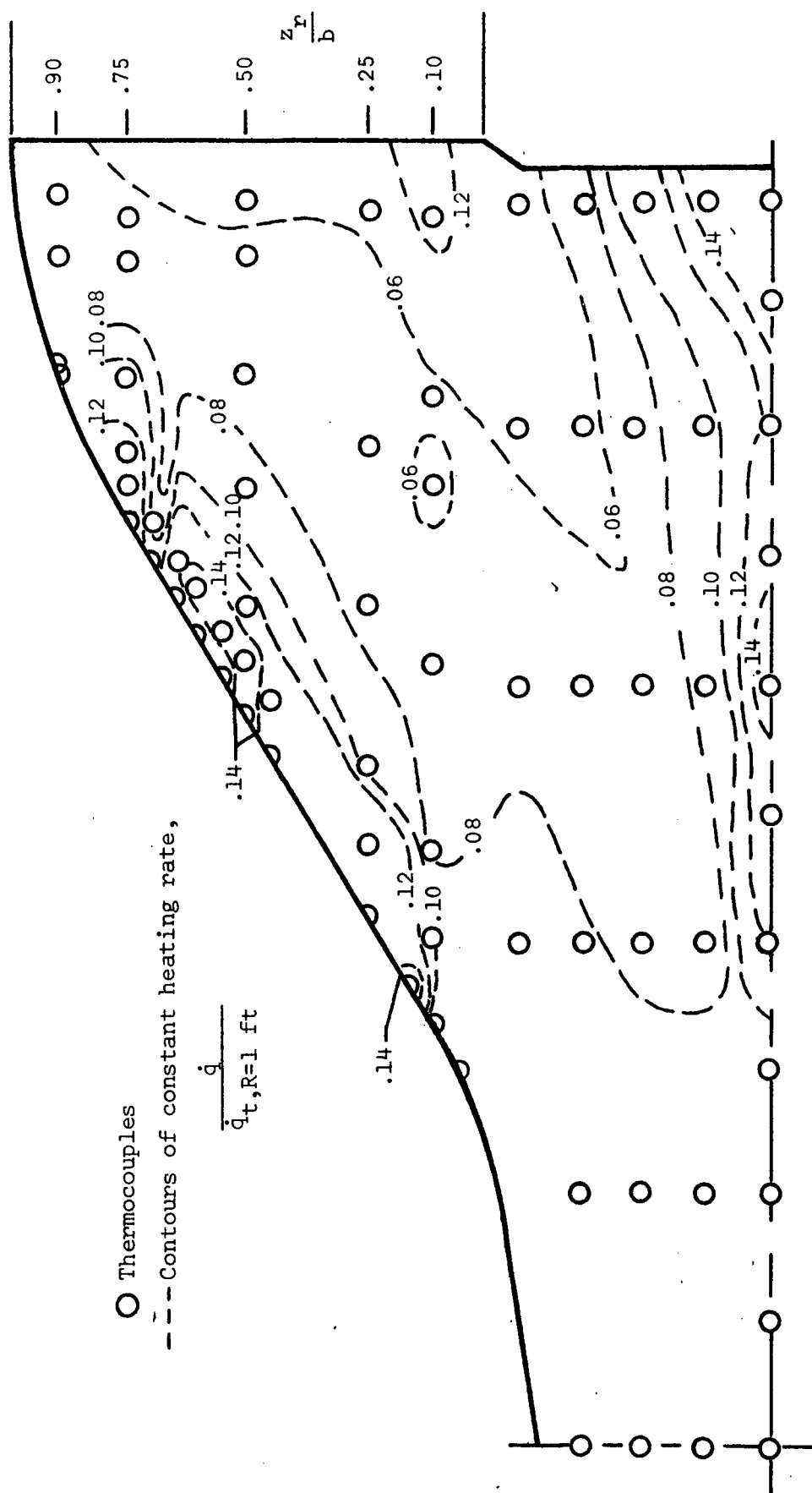
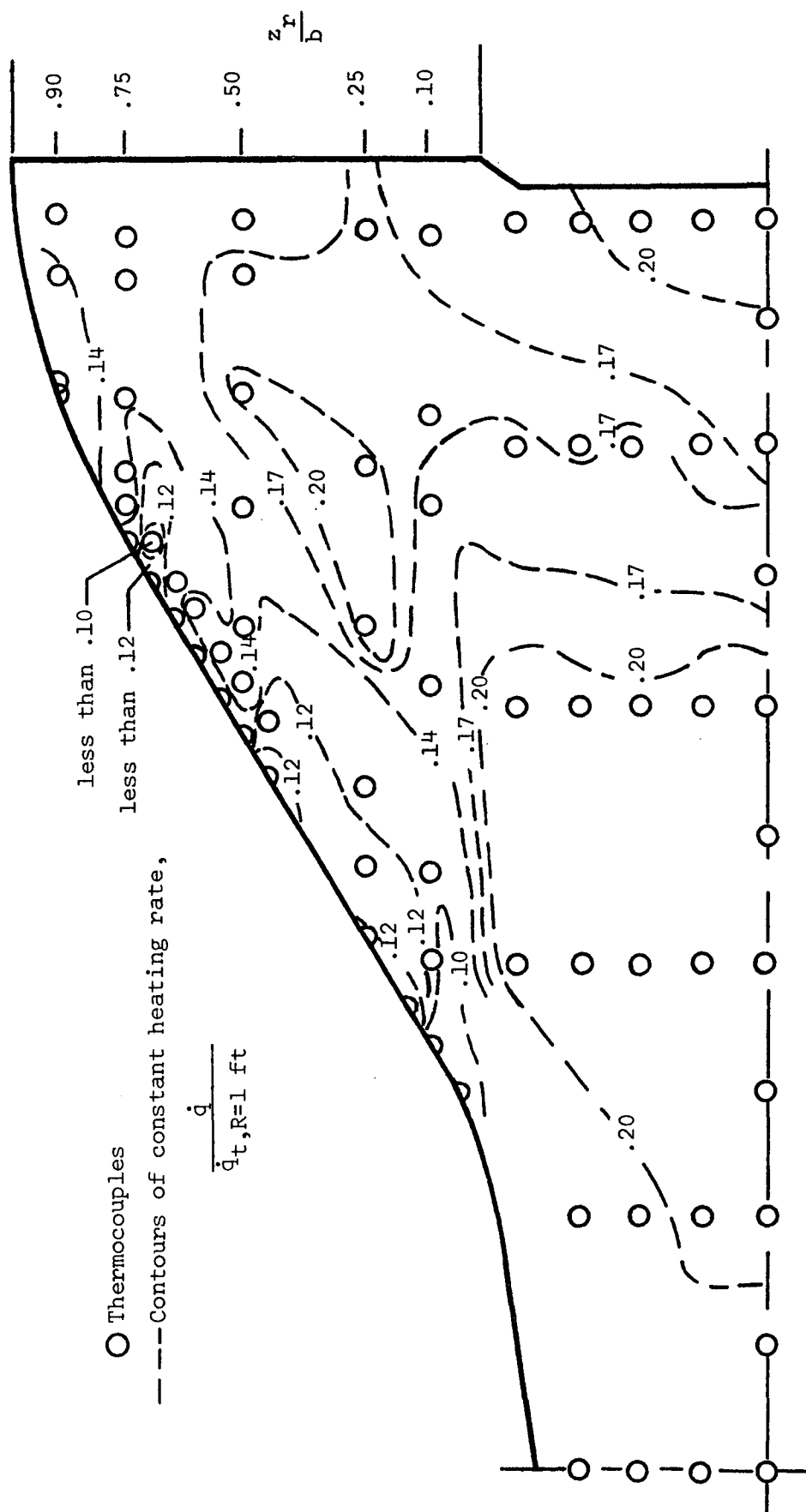


Figure 29. - Windward heat-transfer distribution over the wing and fuselage of the NAR 161B at an alpha of 50°.



(b)  $M_\infty = 8.00$ ,  $Re_{\infty, L} = 6.22 \times 10^6$

Figure 29. - Concluded

Tunnel B, AEDC

3.5-ft Hypersonic, ARC (ref. 25)

●  $M_\infty = 8.00$ ,  $Re_{\infty,L} = 4.16 \times 10^6$

◻  $M_\infty = 7.4$ ,  $Re_{\infty,L} = 2.32 \times 10^6$

●  $M_\infty = 8.00$ ,  $Re_{\infty,L} = 6.22 \times 10^6$

◻  $M_\infty = 7.4$ ,  $Re_{\infty,L} = 8.42 \times 10^6$

◊  $M_\infty = 7.4$ ,  $Re_{\infty,L} = 13.37 \times 10^6$

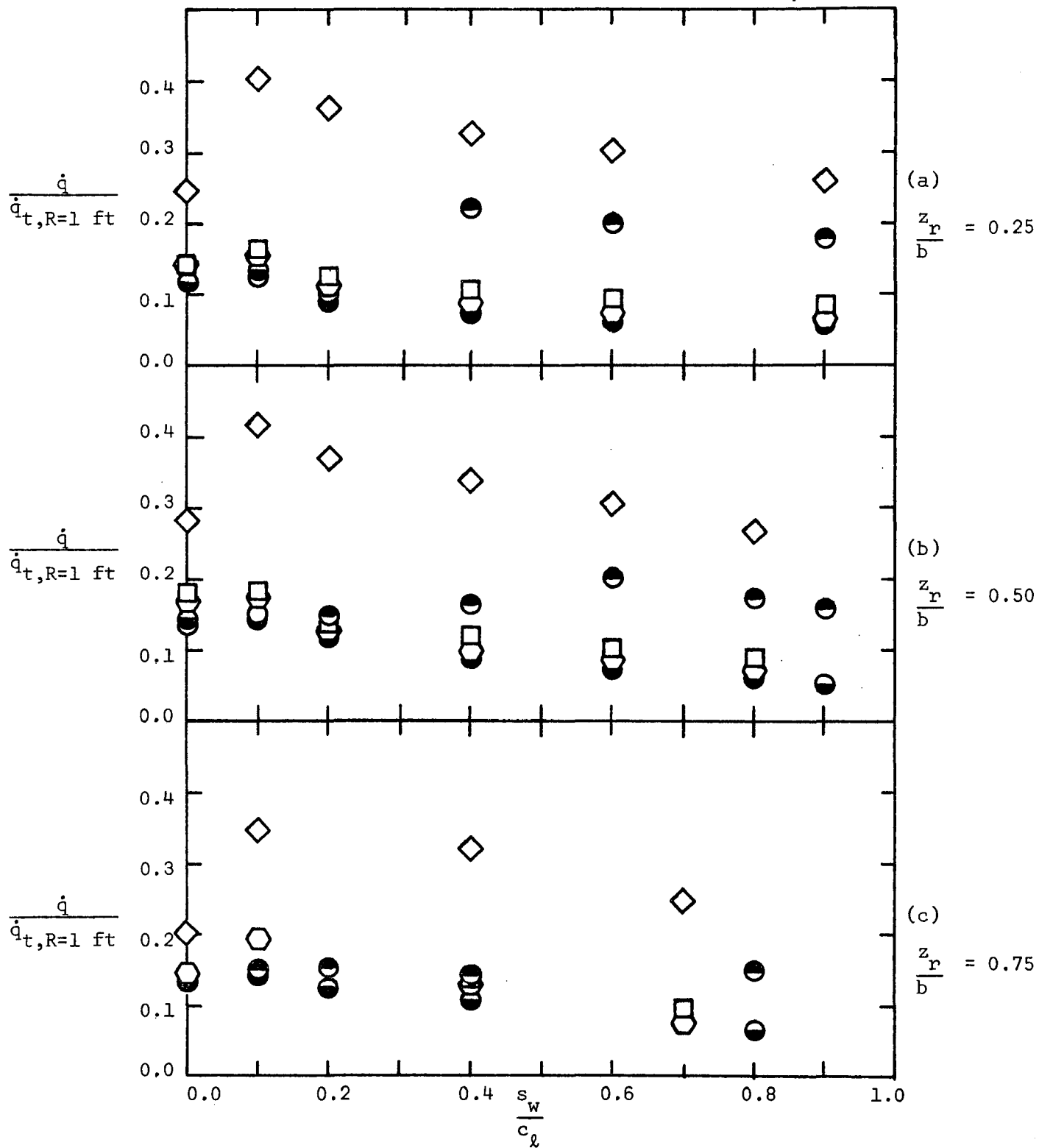
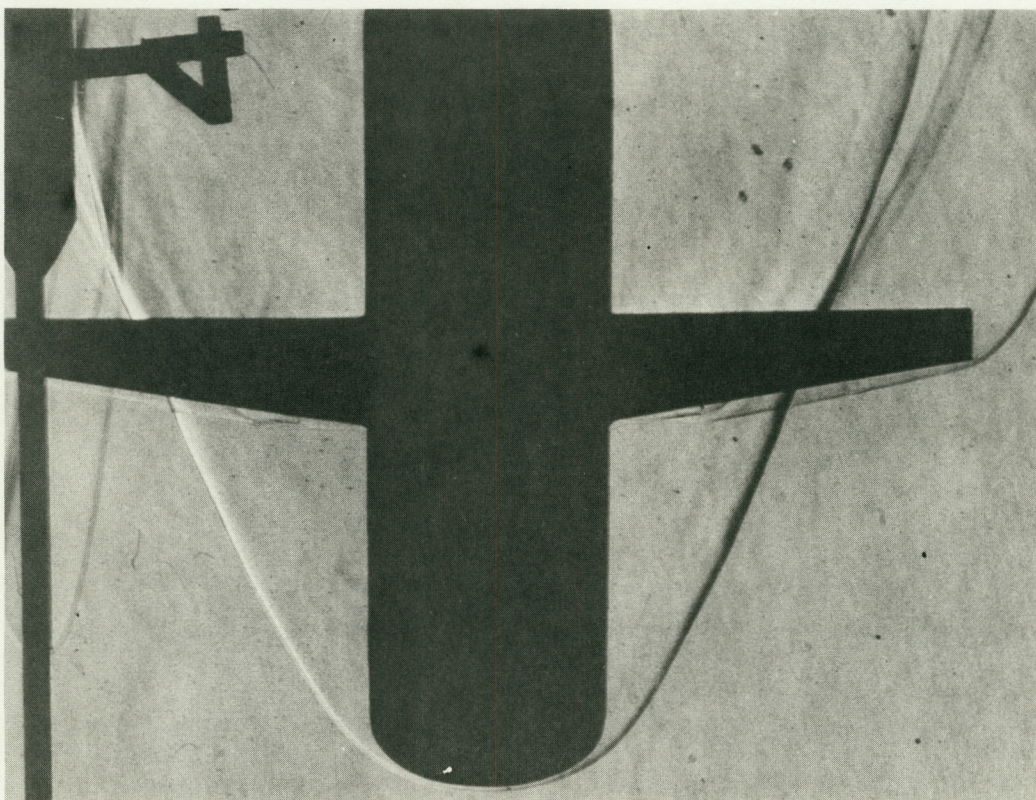
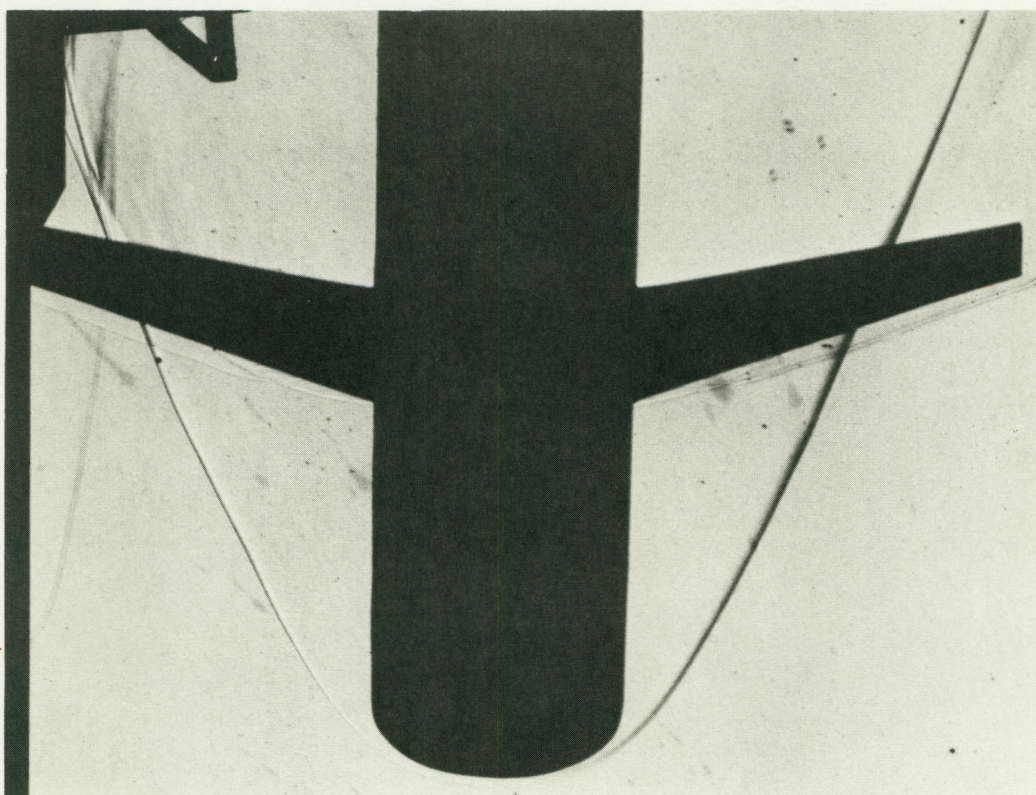


Figure 30. - Chordwise heat-transfer-rate distributions for the NAR 161B at an alpha of 50°.





(a) F3:W2 ( $\Lambda = 15^\circ$ )



(b) F3:W3 ( $\Lambda = 30^\circ$ )

Figure 31. - Flow-field photographs for straight-wing orbiters at an angle of  $50^\circ$ .  $M_\infty = 12$ ,  $Re_\infty/ft = 4 \times 10^6$



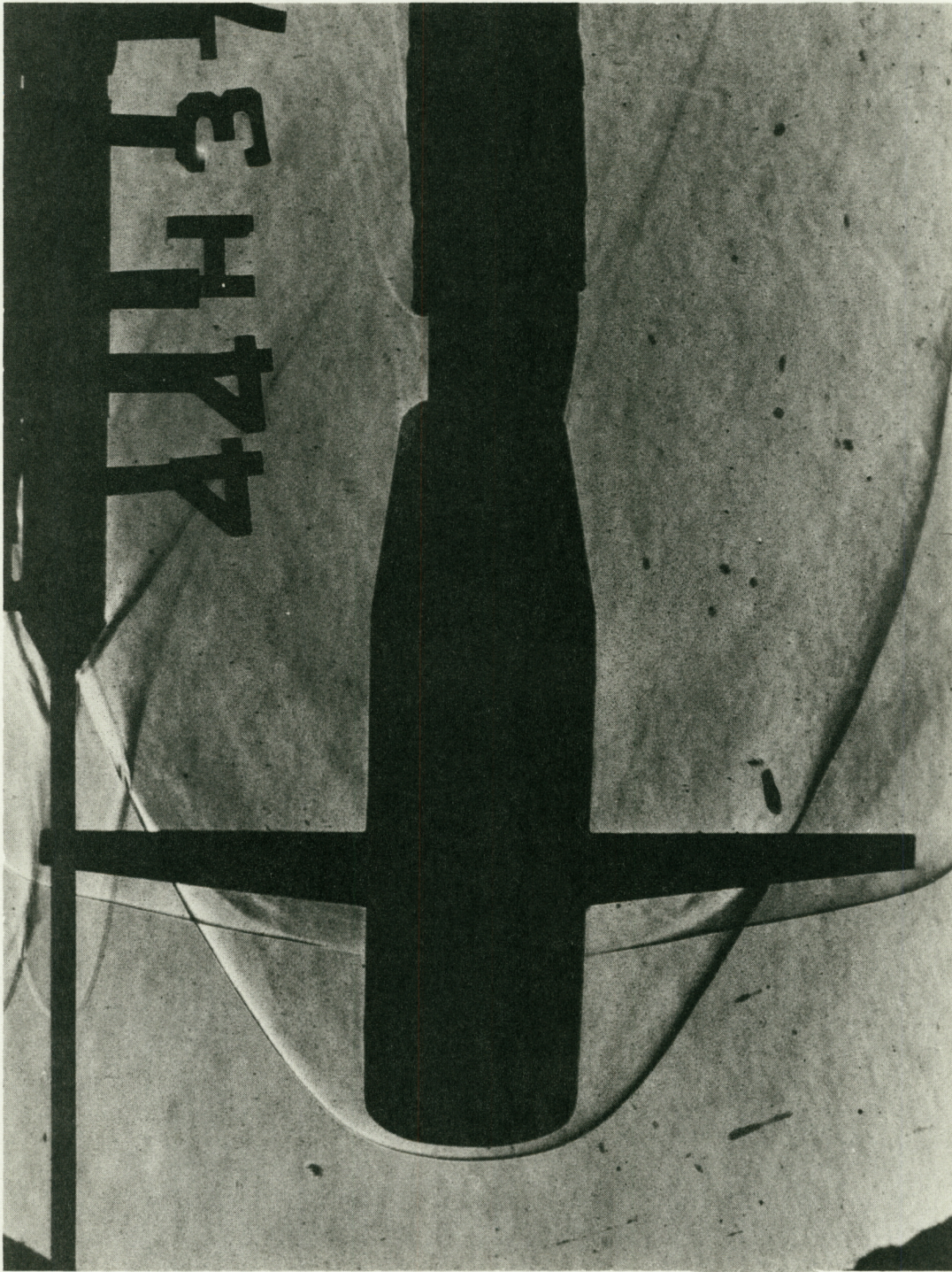


Figure 32. - Flow photographs for the F3:W2 at an  
alpha of 50°.  $M_\infty = 12$ ,  $Re_\infty/ft = 4 \times 10^6$



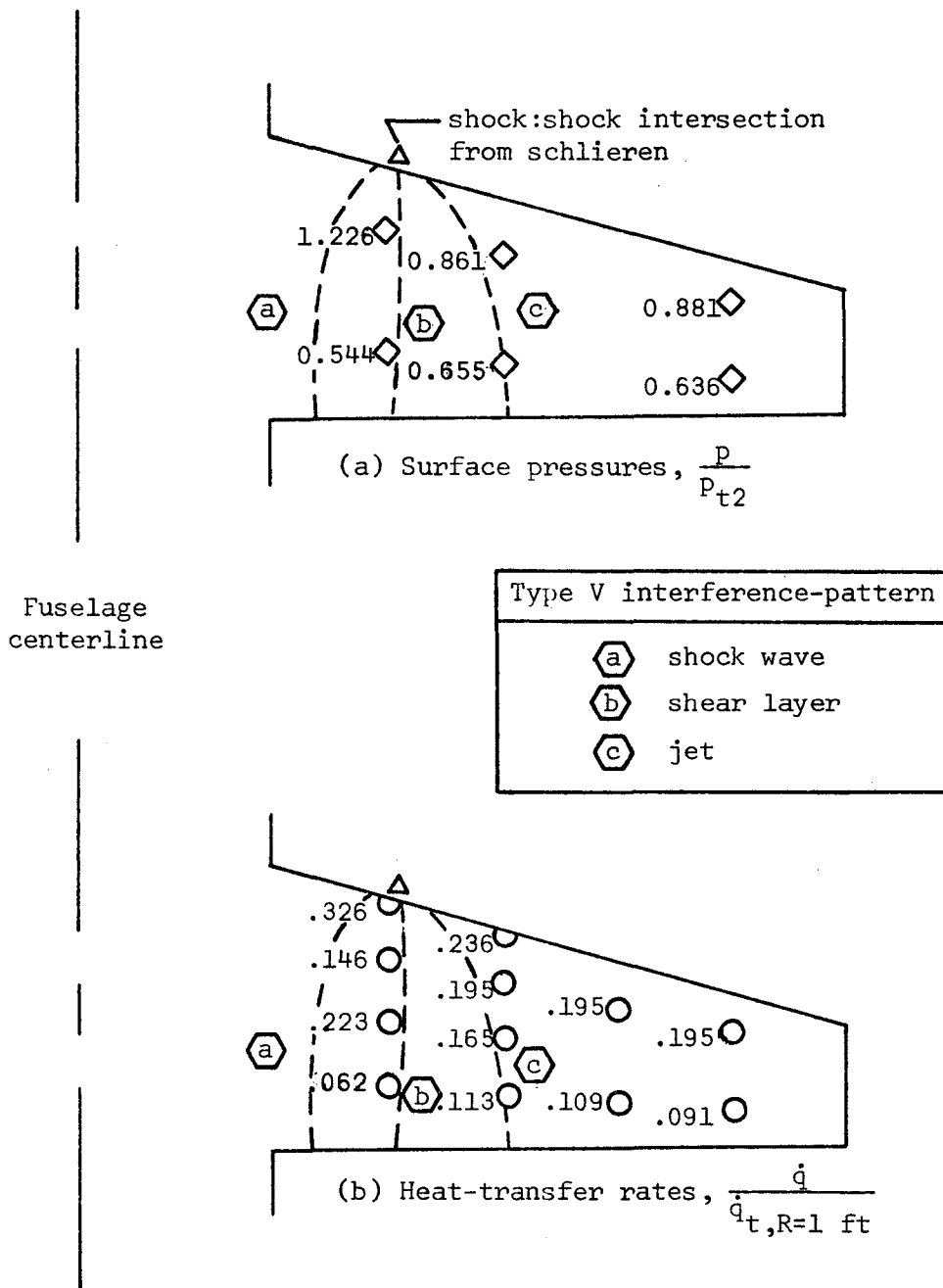


Figure 33. - Surface-pressures and heat-transfer rates on the windward wing surface of the F3:W2 at an alpha of 50°.  $M_\infty = 11.89$ ,  $Re_\infty/\text{ft} = 4.21 \times 10^6$ .

○ F3:W2,  $M_\infty = 11.89$ ,  $Re_\infty/ft = 4.21 \times 10^6$

△ F4:W2,  $M_\infty = 12.07$ ,  $Re_\infty/ft = 4.67 \times 10^6$

□ F4:W2,  $M_\infty = 17.06$ ,  $Re_\infty/ft = 1.85 \times 10^6$

open:  $s_w = 0.25c_\ell$ ; half-filled:  $s_w = 0.50c_\ell$ ;

filled:  $s_w = 0.75c_\ell$

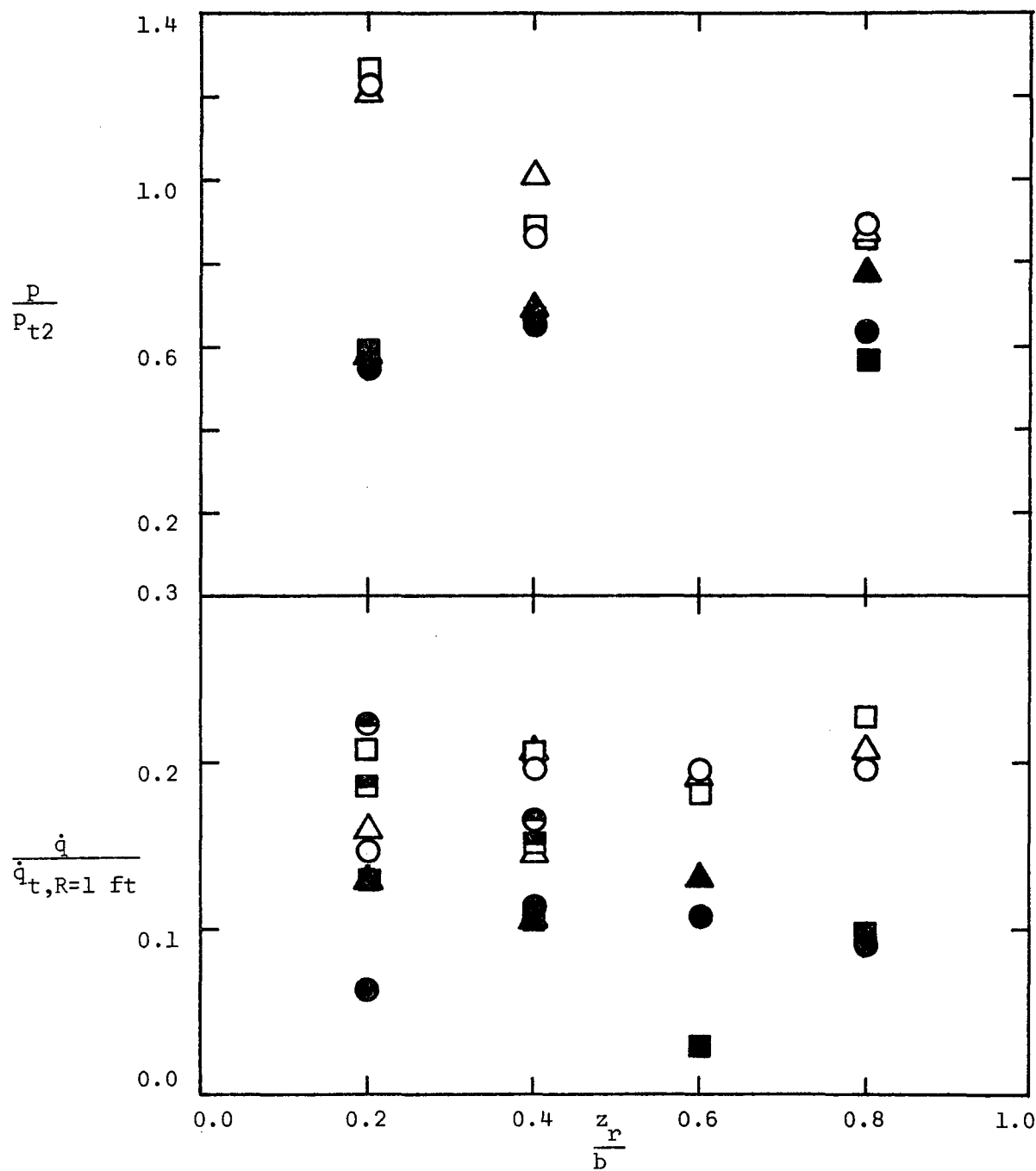


Figure 34. - The surface pressures and the heat-transfer rates measured on the wings of the W2-configurations at an alpha of 50°.



○ F3:W3,  $M_\infty = 11.87$ ,  $Re_\infty/ft = 4.32 \times 10^6$

open:  $s_w = 0.25c_\ell$ ; half-filled:  $s_w = 0.50c_\ell$ ;

filled:  $s_w = 0.75c_\ell$

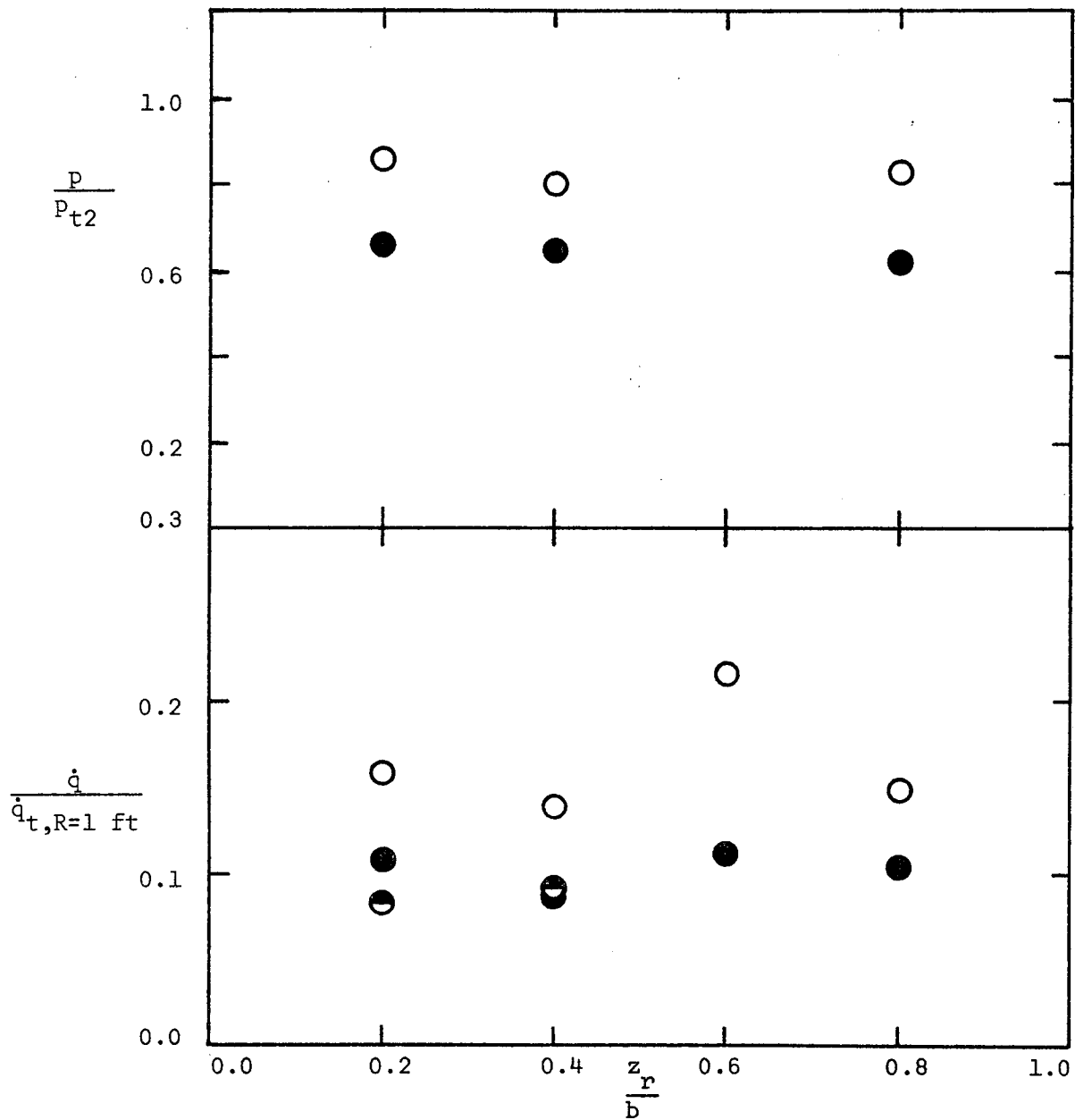


Figure 35. - The surface pressures and the heat-transfer rates measured on the wings of the F3:W3 at an alpha of 50°.

$\triangle$  F3:W2,  $M_\infty = 12.04$ ,  $Re_\infty/ft = 4.23 \times 10^6$

$\circ$  F4:W2,  $M_\infty = 11.96$ ,  $Re_\infty/ft = 3.99 \times 10^6$

$\square$  F4:W2,  $M_\infty = 16.77$ ,  $Re_\infty/ft = 1.90 \times 10^6$

open:  $s_w = 0.25c_\ell$ ; Half-filled:  $s_w = 0.50c_\ell$ ;

filled:  $s_w = 0.75c_\ell$

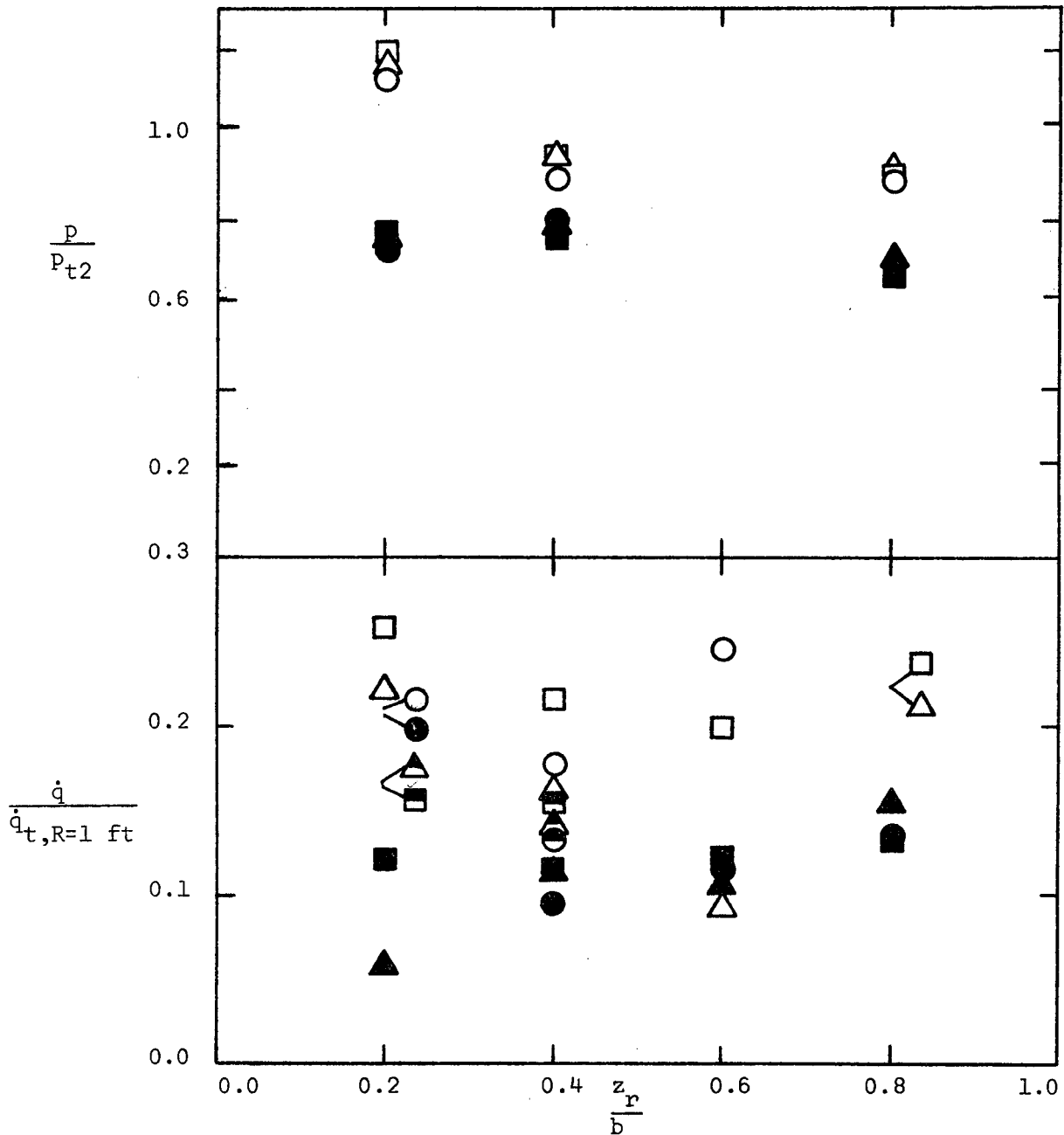


Figure 36. - The surface pressures and the heat-transfer rates measured on the wings of the W2-configurations at an alpha of 60°.

$\frac{s_w}{c_l}$	Conf	$M_\infty$	$Re_{\infty,L}$
$\triangle$ .25	F3:W2	12.04	$1.73 \times 10^6$
$\circ$ .25	F4:W2	11.96	$1.63 \times 10^6$
$\square$ .25	F4:W2	16.77	$0.78 \times 10^6$
$\bullet$ -.17	MSC Orbiter	16.3	$1.58 \times 10^6$ (ref. 15)
$\bullet$ -.17	MSC Orbiter	7.8	$3.72 \times 10^6$ (ref. 15)
$\blacklozenge$ .20	MSC Orbiter	7.4	$1. \times 10^6$ (ref. 14)
$\bullet$ .25	NAR Orbiter	7.4	$1.02 \times 10^6$ (ref. 13)

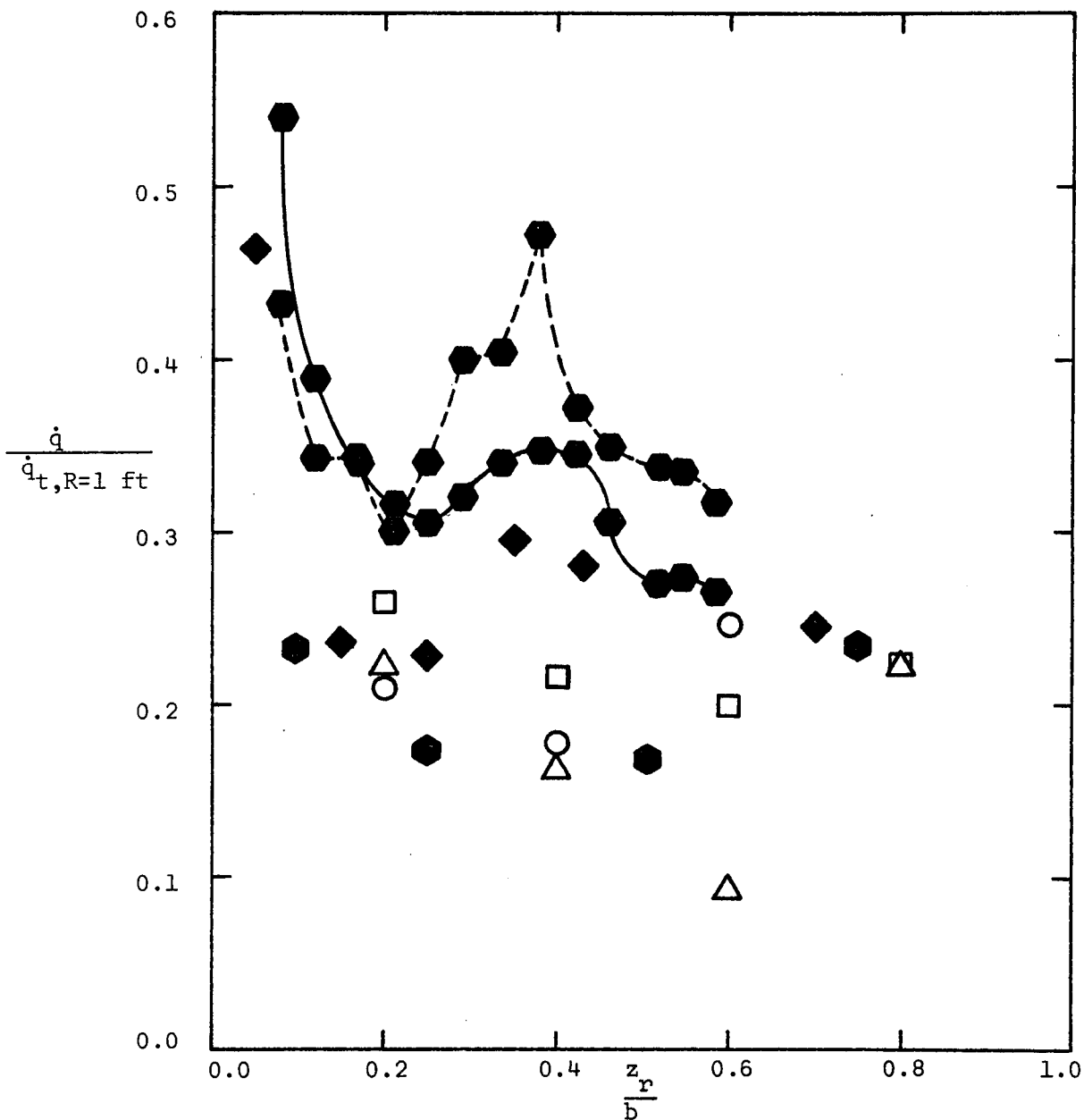


Figure 37. - Spanwise heat-transfer distributions near the quarter-chord for straight-wing orbiters at an alpha of  $60^\circ$ .

NAR 161B DWO  
 $M_\infty = 8.00$ ,  $Re_\infty/ft = 3.74 \times 10^6$

VAC DWO  
 $M_\infty = 10.61$ ,  $Re_\infty/ft = 2.59 \times 10^6$

●  $z_r = 0.10b$

○  $z_r = 0.2b$

■  $z_r = 0.25b$

□  $z_r = 0.4b$

▲  $z_r = 0.50b$

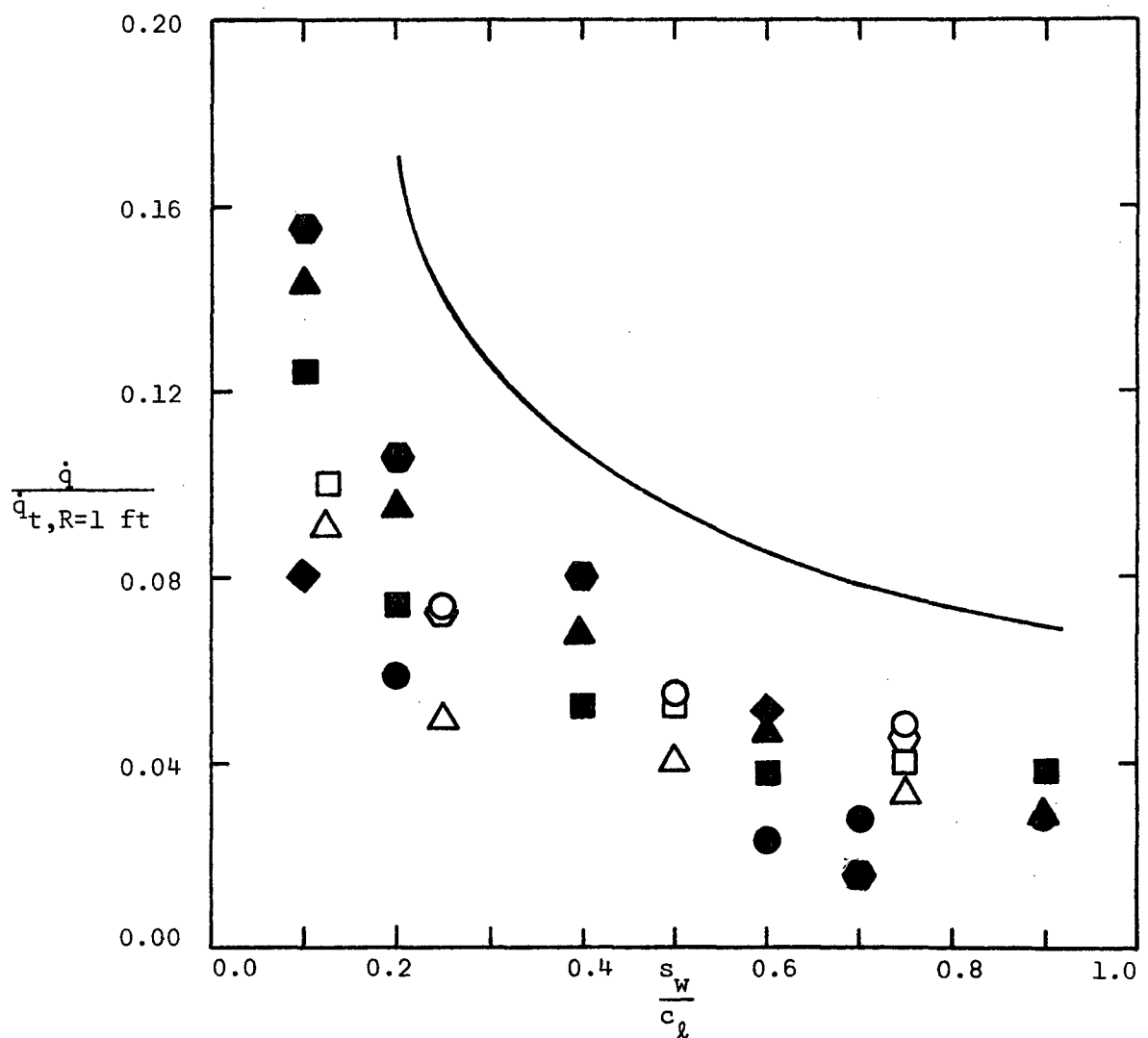
△  $z_r = 0.6b$

⬢  $z_r = 0.75b$

⬡  $z_r = 0.8b$

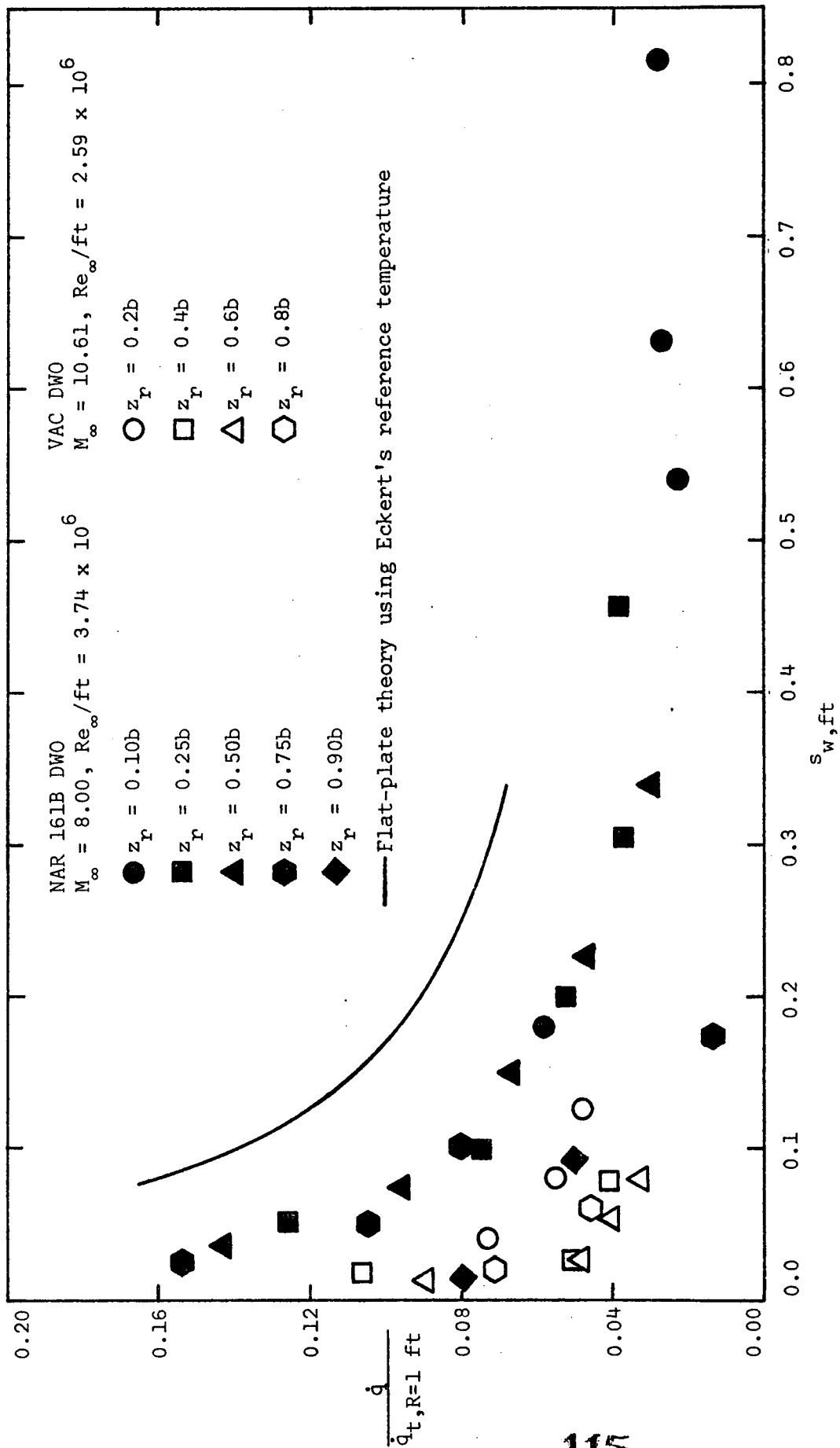
◆  $z_r = 0.90b$

— Flat-plate theory using Eckert's reference temperature



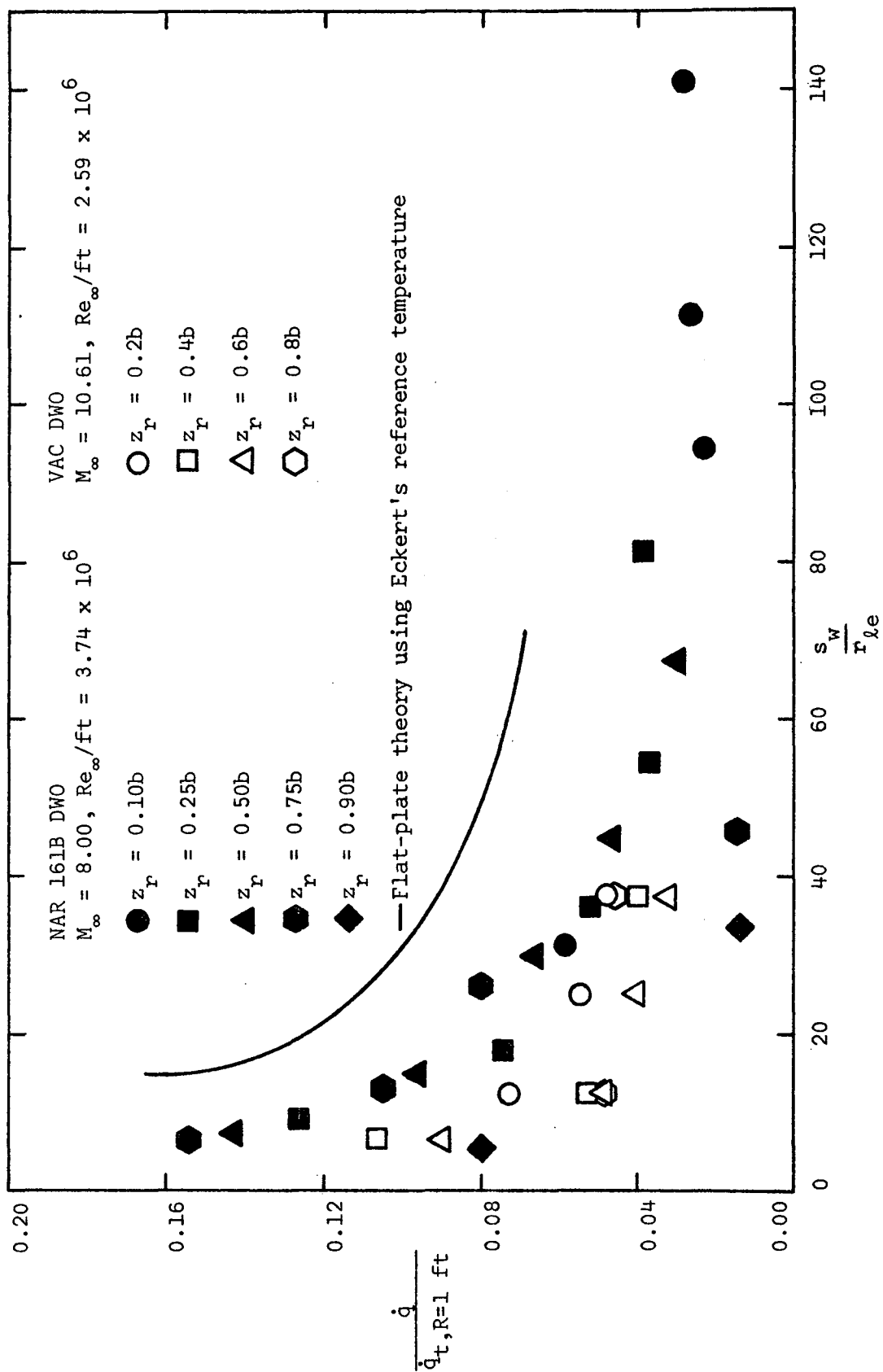
(a) Nondimensionalized with respect to  $c_l$

Figure 38. - The chordwise heat-transfer distributions on the windward surface of the delta-wing at an alpha of 30°.



(b) Dimensional distance

Figure 38. - Continued



(c) Nondimensionalized with respect to  $r_{le}$

Figure 38. - Concluded

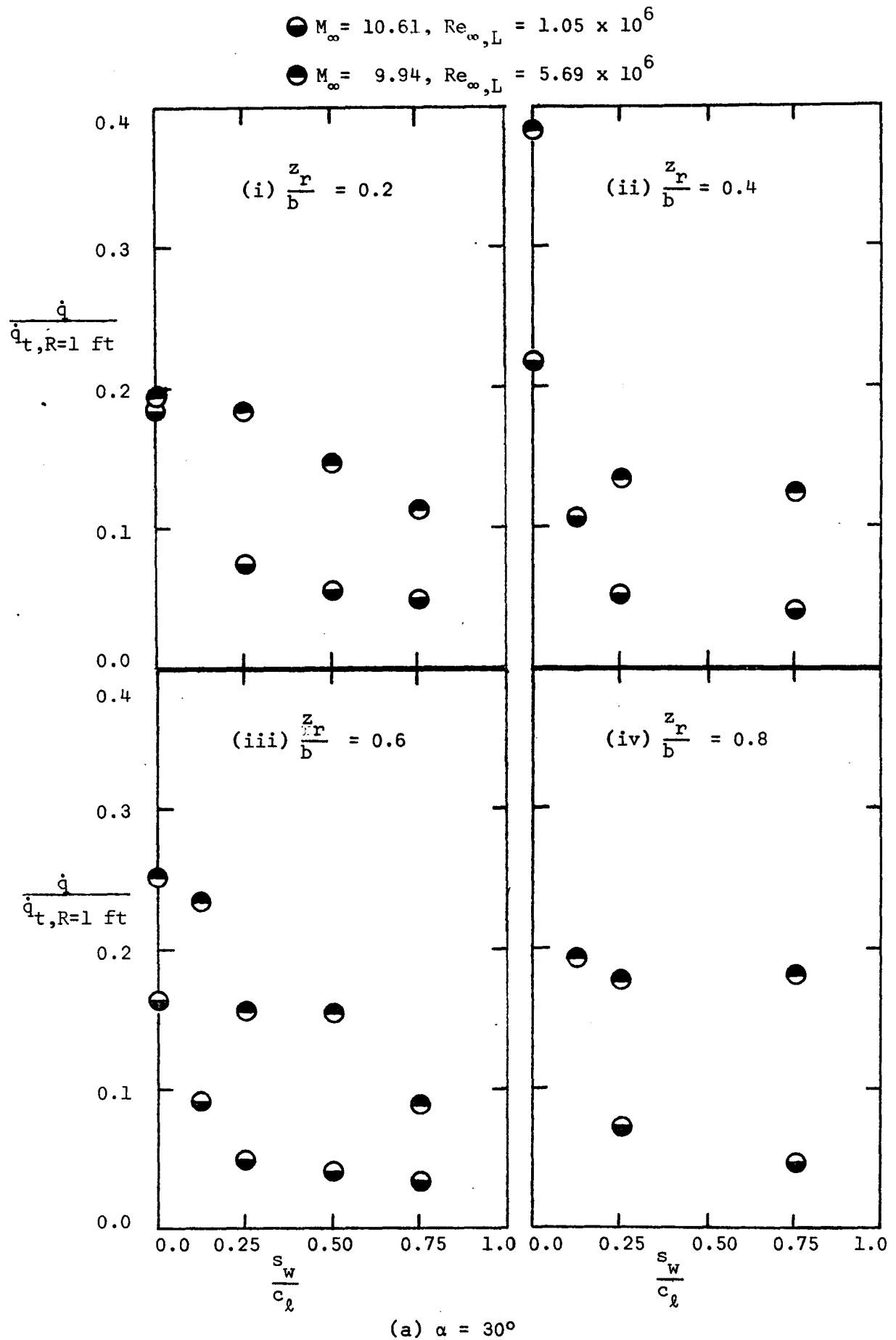
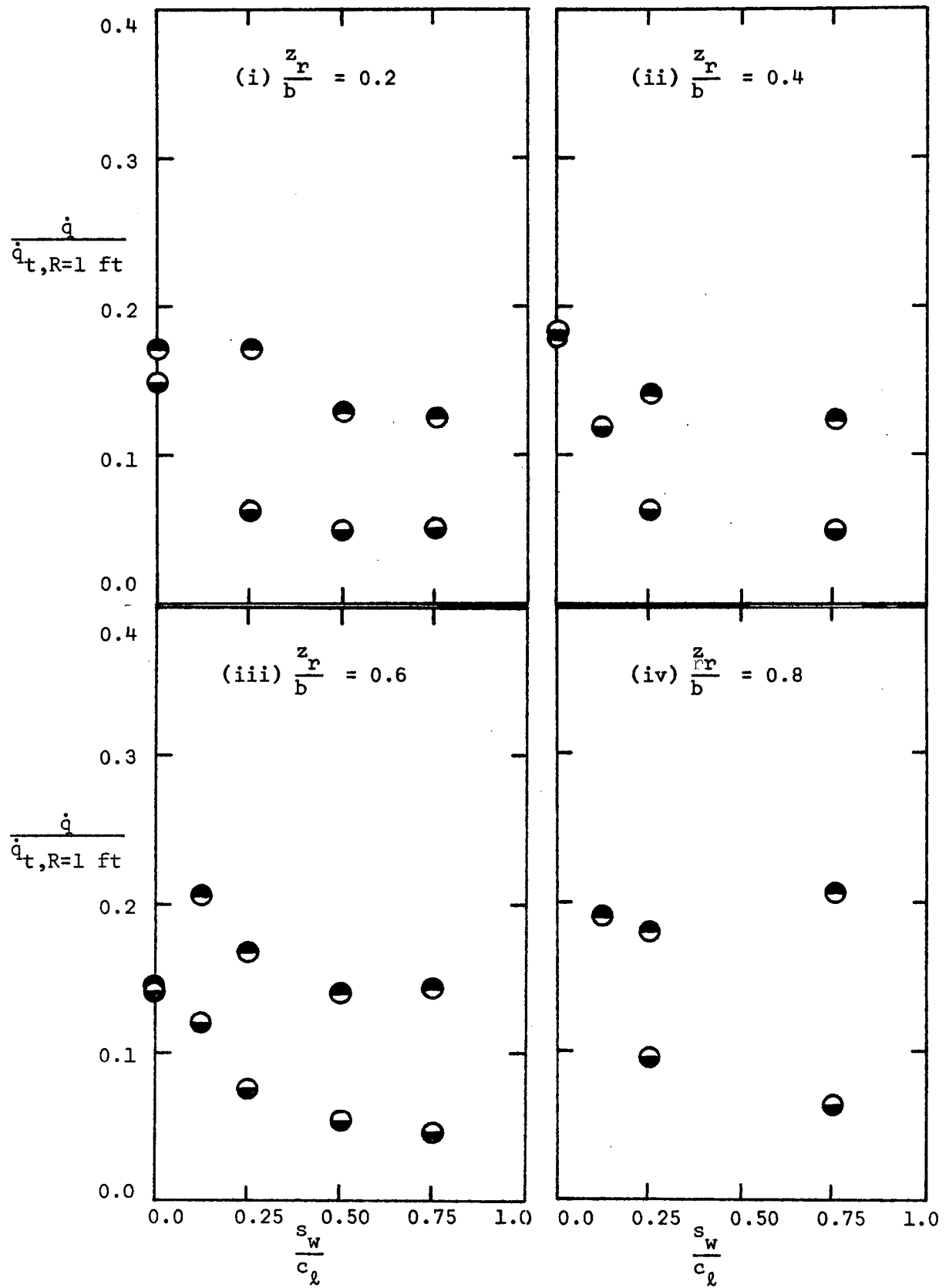


Figure 39. - Chordwise heat-transfer distributions for the VAC DWO.

$$\bullet M_{\infty} = 10.60, Re_{\infty,L} = 1.16 \times 10^6$$

$$\bullet M_{\infty} = 9.93, Re_{\infty,L} = 5.41 \times 10^6$$



(b)  $\alpha = 50^\circ$

Figure 39. - Concluded